

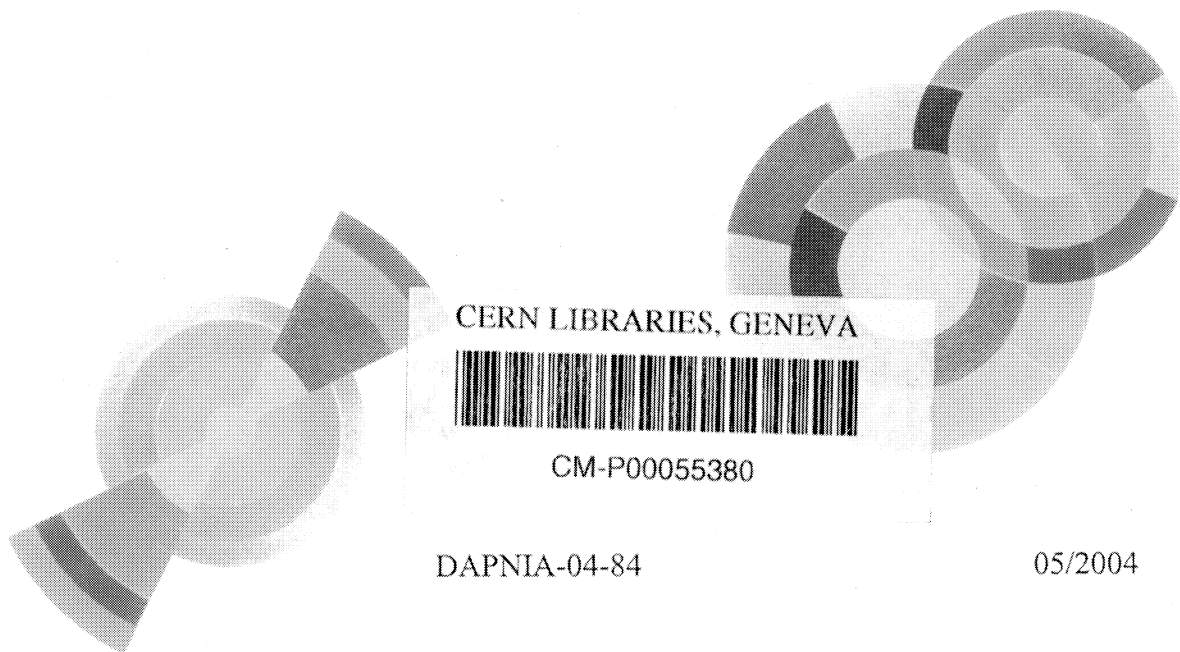
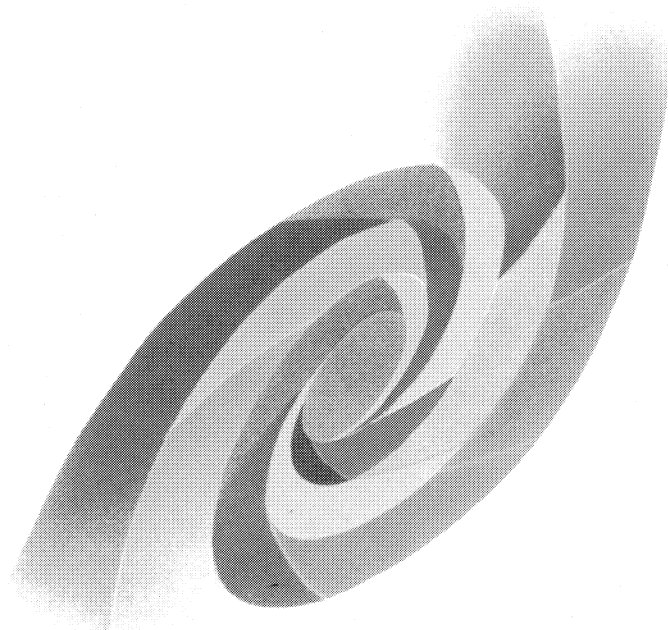


CEA



DAPNIA

22



CERN LIBRARIES, GENEVA



CM-P00055380

DAPNIA-04-84

05/2004

**Letter of intent for Double-CHOOZ :  
a search for the mixing angle  $\theta_{13}$ .**

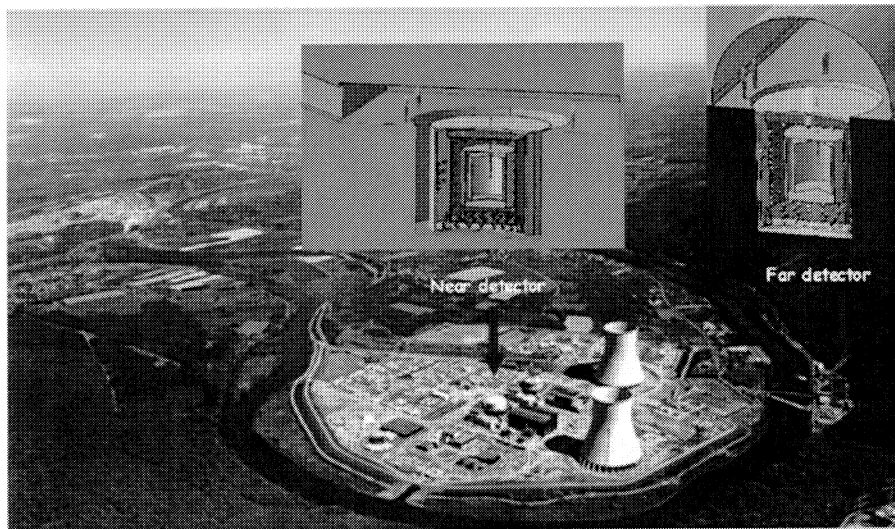
F. Ardellier et al (J.C. Barriere, M. Cribier, T. Lasserre,  
A. Letourneau, F. Marie, A. Milsztajn, J.P. Meyer, L. Scola,)

*Rapport*

Département d'Astrophysique, de Physique des Particules, de Physique Nucléaire et de l'Instrumentation Associée

DSM/DAPNIA, CEA/Saclay F - 91191 Gif-sur-Yvette Cédex  
Tél : (1) 69 08 24 02 Fax : (1) 69 08 99 89  
[http : //www-dapnia.cea.fr](http://www-dapnia.cea.fr)

Letter of Intent for Double-CHOOZ:  
a Search for the Mixing Angle  $\theta_{13}$



APC, Paris - RAS, Moscow - DAPNIA, Saclay  
EKU-Tübingen - INFN, Assergi & Milano  
Institute Kurchatov, Moscow- MPIK, Heidelberg  
Subatech, Nantes - TUM, München  
University of l'Aquila -Universität Hamburg

May 2004

F. Ardellier<sup>3</sup>, I. Barabanov<sup>7</sup>, J.C. Barrière<sup>3</sup>, M. Bauer<sup>4</sup>, L. Bezrukov<sup>7</sup>,  
Ch. Buck<sup>8</sup>, C. Cattadori<sup>5,6</sup>, B. Courty<sup>1,9</sup>, M. Cribier<sup>1,3</sup>, F. Dalnoki-  
Veress<sup>8</sup>, N. Danilov<sup>2</sup>, H. de Kerret<sup>1,9</sup>, A. Di Vacri<sup>5,13</sup>, A. Etenko<sup>10</sup>,  
M. Fallot<sup>11</sup>, Ch. Grieb<sup>12</sup>, M. Goeger<sup>12</sup>, A. Guertin<sup>11</sup>, T. Kirchner<sup>11</sup>,  
Y.S. Krylov<sup>2</sup>, D. Kryn<sup>1,9</sup>, C. Hagner<sup>14</sup>, W. Hampel<sup>8</sup>, F.X. Hartmann<sup>8</sup>,  
P. Huber<sup>12</sup>, J. Jochum<sup>4</sup>, T. Lachenmaier<sup>12</sup>, Th. Lasserre<sup>1,3,†</sup>, Ch. Lend-  
vai<sup>12</sup>, M. Lindner<sup>12</sup>, F. Marie<sup>3</sup>, J. Martino<sup>11</sup>, G. Mention<sup>1,9</sup>, A. Mil-  
sztajn<sup>3</sup>, J.P. Meyer<sup>3</sup>, D. Motta<sup>8</sup>, L. Oberauer<sup>12</sup>, M. Obolensky<sup>1,9</sup>,  
L. Pandola<sup>5,13</sup>, W. Potzel<sup>12</sup>, S. Schönert<sup>8</sup>, U. Schwan<sup>8</sup>, T. Schwetz<sup>12</sup>,  
S. Scholl<sup>4</sup>, L. Scola<sup>3</sup>, M. Skorokhvatov<sup>10</sup>, S. Sukhotin<sup>9,10</sup>, A. Le-  
tourneau<sup>3</sup>, D. Vignaud<sup>1,9</sup>, F. von Feilitzsch<sup>12</sup>, W. Winter<sup>12</sup>, E. Yanovich<sup>7</sup>

<sup>1</sup> APC, 11 place Marcelin Berthelot, 75005 Paris, France

<sup>2</sup> IPC of RAS, 31, Leninsky prospect, Moscow 117312, Russia

<sup>3</sup> DAPNIA (SEDI, SIS, SPhN, SPP), CEA/Saclay, 91191 Gif-sur-Yvette, France

<sup>4</sup> Eberhard Karls Universität, Wilhelmstr. D-72074 Tübingen, Germany

<sup>5</sup> INFN, LGNS, I-67010 Assergi (AQ), Italy

<sup>6</sup> INFN Milano, Via Celoria 16, 20133 Milano, Italy

<sup>7</sup> INR of RAS, 7a, 60th October Anniversary prospect, Moscow 117312, Russia

<sup>8</sup> MPI für Kernphysik, Saupfercheckweg 1, D-69117 Heidelberg, Germany

<sup>9</sup> PCC Collège de France, 11 place Marcelin Berthelot, 75005 Paris, France

<sup>10</sup> RRC Kurchatov Institute, 123182 Moscow, Kurchatov sq. 1, Russia

<sup>11</sup> Subatech (Ecole des Mines), 4, rue Alfred Kastler, 44307 Nantes, France

<sup>12</sup> TU München. James-Franck-Str., D-85748 Garching, Germany

<sup>13</sup> University of L'Aquila, Via Vetoio 1, I-67010 Coppito, L'Aquila, Italy

<sup>14</sup> Universität Hamburg, Luruper Chaussee 149, D-22761 Hamburg, Germany

---

<sup>†</sup>Corresponding author, thierry.lasserre@cea.fr

### Abstract

Tremendous progress has been achieved in neutrino oscillation physics during the last few years. However, the smallness of the  $\theta_{13}$  neutrino mixing angle still remains enigmatic. The current best constraint comes from the CHOOZ reactor neutrino experiment  $\sin^2(2\theta_{13}) < 0.2$  (at 90% C.L., for  $\Delta m_{\text{atm}}^2 = 2.0 \cdot 10^{-3} \text{ eV}^2$ ). We propose a new experiment on the same site, Double-CHOOZ, to explore the range of  $\sin^2(2\theta_{13})$  from 0.2 to 0.03, within three years of data taking. The improvement of the CHOOZ result requires an increase in the statistics, a reduction of the systematic error below one percent, and a careful control of the cosmic ray induced background. Therefore, Double-CHOOZ will use two identical detectors, one at  $\sim 150$  m and another at 1.05 km distance from the nuclear cores. The plan is to start data taking with two detectors in 2008, and to reach a sensitivity for  $\sin^2(2\theta_{13})$  of 0.05 in 2009, and 0.03 in 2011.



# Contents

<b>1</b>	<b>Physics opportunity</b>	<b>11</b>
<b>2</b>	<b>Searching for <math>\sin^2(2\theta_{13})</math> with reactors</b>	<b>15</b>
2.1	Neutrino oscillations	15
2.1.1	Quark mixing	15
2.1.2	Neutrino mixing	15
2.2	Measurement of $\sin^2(2\theta_{13})$ with reactor $\bar{\nu}_e$	16
2.2.1	Reactor $\bar{\nu}_e$ flux	16
2.2.2	$\bar{\nu}_e$ detection principle	17
2.2.3	$\bar{\nu}_e$ oscillations	19
2.3	Complementarity with Superbeam experiments	20
<b>3</b>	<b>Overview of the Double-CHOOZ experiment</b>	<b>23</b>
3.1	The $\bar{\nu}_e$ source	23
3.1.1	The CHOOZ nuclear reactors	23
3.2	Detector site	24
3.3	Detector design	25
3.3.1	Experimental errors and backgrounds	28
3.3.2	Sensitivity	30
<b>4</b>	<b>Detector design and simulation</b>	<b>33</b>
4.1	Detector design	33
4.1.1	The $\bar{\nu}_e$ target acrylic vessel (12.67 m <sup>3</sup> )	33
4.1.2	$\gamma$ -catcher acrylic vessel (28.1 m <sup>3</sup> )	33
4.1.3	Non scintillating buffer (100 m <sup>3</sup> )	36
4.1.4	PMTs and PMT support structure	36
4.1.5	Veto (110 m <sup>3</sup> )	37
4.2	Fiducial volume	37
4.2.1	Definition of the fiducial volume	37
4.2.2	Measurement of the fiducial volume	38
4.3	Light collection	38
4.4	Electronics	42
4.4.1	Data recording	42
4.4.2	Trigger logic	43
<b>5</b>	<b>Liquid scintillators and buffer liquids</b>	<b>45</b>
5.1	Liquid inventory	45
5.2	Status of available scintillators	46
5.3	Scintillator definition phase	47
5.4	Scintillator fluid systems	49

<b>6</b>	<b>Calibration</b>	<b>51</b>
6.1	Optical and electronic calibrations	52
6.2	Energy calibration	52
6.2.1	Gamma ray sources	52
6.2.2	Positron response	53
6.2.3	Neutron response	53
6.2.4	The Calibration source deployment system	54
6.2.5	Map of the Gd-LS target	54
6.2.6	Calibrating the gamma-catcher, buffer, and veto	56
<b>7</b>	<b>Backgrounds</b>	<b>57</b>
7.1	Beta and gamma background	57
7.1.1	Intrinsic beta and gamma background	57
7.1.2	External gamma background	58
7.2	Neutron background	58
7.2.1	Intrinsic background sources	58
7.2.2	External background sources	58
7.2.3	Beta-neutron cascades	59
7.2.4	External neutrons and correlated events	60
7.2.5	Conclusion	62
<b>8</b>	<b>Experimental Errors</b>	<b>65</b>
8.1	From CHOOZ to Double-CHOOZ	65
8.2	Relative normalization of the two detectors	65
8.3	Detector systematic uncertainties	66
8.3.1	Solid angle	66
8.3.2	Number of free protons in the target	66
8.3.2.1	Volume measurement	66
8.3.2.2	Density	66
8.3.2.3	Number of hydrogen atoms per gramme	66
8.3.3	Neutron efficiency	67
8.3.3.1	Gadolinium concentration	67
8.3.3.2	Spatial effects	67
8.3.4	Positron efficiency	67
8.4	Selection cuts uncertainties	67
8.4.1	Identifying the prompt positron signal	68
8.4.2	Identifying the neutron delayed signal	68
8.4.3	Time correlation	68
8.4.4	Space correlation	69
8.4.5	Veto and dead time	69
8.4.6	Electronics and acquisition	70
8.4.7	Summary of the systematic uncertainty cancellations	70
8.4.8	Systematic uncertainties outlook	71
8.5	Background subtraction error	71
8.6	Liquid scintillator stability and calibration	72
<b>9</b>	<b>Sensitivity and discovery potential</b>	<b>73</b>
9.1	The neutrino signal	73
9.1.1	Reactor $\bar{\nu}_e$ spectrum	73
9.1.2	Detector and power station features	73
9.1.3	Expected number of events	74
9.2	Systematic errors handling	75
9.2.1	$\chi^2$ analysis	75
9.2.2	Absolute normalization error: $\sigma_{\text{abs}}$	76

9.2.3	Relative normalization error: $\sigma_{\text{rel}}$ . . . . .	76
9.2.4	Spectral shape error: $\sigma_{\text{shp}}$ . . . . .	76
9.2.5	Energy scale error: $\sigma_{\text{scf}}$ . . . . .	76
9.2.6	Individual core power fluctuation error: $\sigma_{\text{cfl}}$ . . . . .	77
9.2.7	Background subtraction error . . . . .	77
	9.2.7.1 Reactor $\bar{\nu}_e$ shape background: $\sigma_{\text{b2b}}$ . . . . .	77
	9.2.7.2 Flat background: $\sigma_{\text{bkg}}$ . . . . .	77
9.3	Sensitivity in the case of no oscillations . . . . .	77
9.3.1	Comparison of Double-CHOOZ and the T2K sensitivities . . .	78
9.4	Discovery potential . . . . .	80
9.4.1	Impact of the errors on the discovery potential . . . . .	80
9.4.2	Comparison of Double-CHOOZ and the T2K discovery potential	81
<b>A</b>	<b><math>\bar{\nu}_e</math> and safeguards applications</b>	<b>A-85</b>
<b>B</b>	<b>Nuclear reactor <math>\beta</math> spectra</b>	<b>B-89</b>
B.1	New $\beta$ energy spectra measurements at ILL . . . . .	B-89
B.2	Reactivity monitoring . . . . .	B-90
B.3	Double-CHOOZ reactor core simulation and follow-up . . . . .	B-90
<b>C</b>	<b>Some numbers from the CHOOZ experiment</b>	<b>C-91</b>



# Chapter 1

## Physics opportunity

Neutrinos play a crucial role in fundamental particle physics and have a huge impact in astroparticle physics and cosmology. Before 2002, neutrino oscillation physics was still in a discovery phase, even though strong evidence for atmospheric [IMB91, SOU97, SK98, MAC98, Ron01, SK02a] and solar neutrino oscillations have already been established since 1998. Thirty years after the discovery of the solar neutrino anomaly [Cle98, SAG02, GAL99, GNO00], the combined SNO Super-Kamiokande discovery of the flavor conversion [SK02b, SNO02] together with the first reactor  $\bar{\nu}_e$  flux suppression observed by KamLAND [KAM02], is now moving neutrino physics to a new era of precision measurements.

In the Standard Model of electroweak interactions, neutrinos are massless particles, and there is no mixing between the leptons. There exists only a left-handed neutrino, and a right-handed antineutrino. In the quark sector of the Model, the mixing between quark weak and mass eigenstates occurs among the three flavor families, and the amount of mixing is determined by the CKM mixing matrix. In the lepton sector, the analogue of the CKM matrix for quarks is just the identity matrix, and three conservation laws have been empirically included, for the three lepton families.

The strong evidence for non-zero neutrino masses clearly indicates the existence of physics beyond the minimal Standard Model. The smallness of neutrino masses together with the amounts of lepton flavor violation found in neutrino oscillation experiments provide insights into possible modifications of the current Standard Model of electroweak interactions, and open a new window towards the Grand Unification energy scale [Gel79].

In the current paradigm, the neutrino mass and weak eigenstates are related through the Pontecorvo-Maki-Nakagawa-Sakata (PMNS) neutrino mixing matrix [Mak62, Pon58]. A synthesis of atmospheric, solar, and reactor neutrino oscillation data requires the existence of (at least) three-neutrino mixing. The PMNS mixing matrix can be parameterized by three mixing angles  $\theta_{sol}$ ,  $\theta_{atm}$ ,  $\theta_{13}$ , and one or three CP-violating phases, depending on the Dirac or Majorana nature of the massive neutrinos [PDG00]. Although not favored by the current data, a scenario with more than three neutrinos might be required to account for the LSND anomaly [LSN98]. In this case, the mixing of the three active neutrinos with the additional sterile neutrino(s) decouples from the oscillations described by the PMNS matrix. The presently running MiniBoone experiment will settle the controversy in the near future [BOO02].

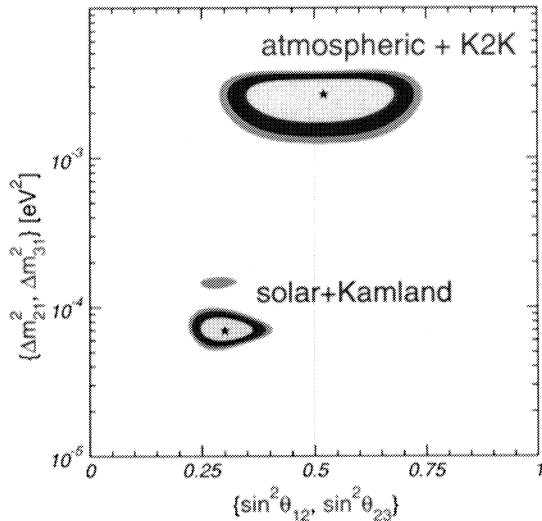


Figure 1.1: Solar and atmospheric allowed regions from the global oscillation data analysis at 90 %, 95 %, 99 %, and  $3\sigma$  C.L. for 2 degrees of freedom [Mal03].

A wide range of experiments using accelerator, atmospheric, reactor, and solar neutrinos will be necessary to achieve a full understanding of the neutrino mixing matrix.

Solar neutrino experiments combined with KamLAND have measured the so-called *solar parameters*<sup>1</sup>  $\Delta m_{\text{sol}}^2 = \Delta m_{21}^2 = 7_{-3}^{+2} \cdot 10^{-5} \text{ eV}^2$  and  $\sin^2(2\theta_{\text{sol}}) = \sin^2(2\theta_{12}) = 0.8_{-0.2}^{+0.2}$  [Mal03, Cle98, SAG02, GAL99, GNO00, SK02b, SNO02, Hub02]. Future solar neutrino data as well as the forthcoming KamLAND results will undoubtedly improve the solar neutrino parameters determination. A new middle baseline (20-70 km) reactor neutrino experiment could further improve  $\Delta m_{\text{sol}}^2$  or/and  $\theta_{\text{sol}}$  if necessary [Pet02, Sch03].

Atmospheric neutrino experiments such as Super-Kamiokande together with the K2K first long baseline accelerator neutrino experiment have measured the so-called *atmospheric parameters*  $\Delta m_{\text{atm}}^2 = |\Delta m_{32}^2| = 2_{-0.7}^{+1.0} \cdot 10^{-3} \text{ eV}^2$  and  $\sin^2(2\theta_{\text{atm}}) = \sin^2(2\theta_{32}) = 1.0_{-0.2}^{+0.0}$  [SK98, MAC98, Ron01, SK02a]. Experimental errors will slowly decrease with additional K2K and Super-Kamiokande data, but a major improvement of the results is expected from the currently starting MINOS long baseline neutrino experiment [MIN01a, MIN01b].

The *third sector* of the neutrino oscillation matrix is driven by the mixing angle  $\theta_{13}$ , currently best constrained by the CHOOZ reactor neutrino experiment [CHO98, CHO99, CHO00, CHO03]. CHOOZ provides the upper bound  $\sin^2(2\theta_{13}) < 0.20$  (90 % C.L.), assuming  $\Delta m_{\text{atm}}^2 = 2.0 \cdot 10^{-3} \text{ eV}^2$  (this upper limit is strongly correlated with the assumed value of  $\Delta m_{\text{atm}}^2$ .) A weaker upper bound,  $\sin^2(2\theta_{13}) < 0.4$ , has been obtained by the Palo-Verde experiment [PV01].

Concerning the determination of the PMNS mixing parameters, the measurement of the angle  $\theta_{13}$  is the next experimental step to accomplish. Knowing the value of  $\theta_{13}$ , or lowering the CHOOZ bound is already fundamental, in itself, in order to better understand the structure of the PMNS matrix. Both atmospheric and

<sup>1</sup>The intervals vary slightly in the different analyzes, we give here the values quoted in [Hub02]. Furthermore, we assume here the normal neutrino mass hierarchy case.

solar mixing angles have been found to be maximal or large, thus the smallness of  $\theta_{13}$  remains a mystery. Moreover, any sub-leading three-neutrino oscillation effects, such as the solar-atmospheric driven oscillation interferences [Pet02, Sch03] or the CP-violation in the lepton sector, could only be observable for non-vanishing  $\theta_{13}$  values.

Which sensitivity is then relevant for the forthcoming projects dedicated to  $\theta_{13}$ ? On the one hand, neutrino mass models predict  $\sin^2(2\theta_{13})$  values ranging from 0 to 0.18 [RWP04]. Any neutrino experiment with a sensitivity of a few percents, like Double-CHOOZ, has thus an important discovery potential. On the other hand, the neutrino mass models connect, in most cases, the CP- $\delta$  phase to the leptogenesis mechanism [Buc04]. The search for CP violation effects in the lepton sector is thus of great interest since the leptogenesis mechanism is one of the best current explanation of the matter-antimatter baryon asymmetry observed in our Universe. The target sensitivity to achieve is thus strongly driven by the potential of future CP- $\delta$  neutrino appearance experiments. In the distant future, CP violation could be observed at neutrino factories if  $\sin^2(2\theta_{13}) > 0.001$ . However, on a shorter time scale, a value of  $\sin^2(2\theta_{13})$  of a few percent might allow superbeam based experiments, possibly combined with a large reactor neutrino detector, to probe part of the  $\delta - \theta_{13}$  parameter space [Hub02].

Although they are not designed to measure  $\theta_{13}$ , a marginal improvement of the CHOOZ constraint can be obtained with conventional neutrino beams. For instance, the MINOS experiment [MIN01a] may achieve a sensitivity  $\sin^2(2\theta_{13}) < 0.1$ , while the CNGS experiments, OPERA and ICARUS [CNG02a, CNG02b, Hub04], may improve the CHOOZ bound down to  $\sin^2(2\theta_{13}) < 0.14$  and  $\sin^2(2\theta_{13}) < 0.09$ , respectively, if no excess of  $\nu_e$  is observed after five years of data taking<sup>2</sup> ( $\Delta m_{\text{atm}}^2 = 2.0 \cdot 10^{-3} \text{ eV}^2$ , 90 % C.L.). The quoted values reduce to 0.05 [MIN01b], 0.08 [OPE03, CNG02b], 0.04 [ICA02], respectively, by neglecting matter effects, CP- $\delta$  phase (set to zero), and mass hierarchy induced correlations and degeneracies [Min02, Hub02].

Concerning the future of neutrino physics, the next generation of accelerator neutrino experiments coupled with powerful neutrino beams (the so-called Superbeam long baseline experiment) are primarily dedicated to the determination of the PMNS mixing matrix elements  $\theta_{13}$  and CP- $\delta$ , as well as the precise measurement of the atmospheric mass splitting and mixing angle, and the identification of the neutrino mass hierarchy (the sign of  $\Delta m_{32}^2$ ). After five years of data taking, the T2K experiment aims to reach the sensitivity  $\sin^2(2\theta_{13}) < 0.02$  (90 % C.L.) [T2K02, T2K03, Hub02]; a similar sensitivity is foreseen by the NuMI Off-Axis project<sup>3</sup> [NUM02].

The observation of a  $\nu_e$  excess in an almost pure  $\nu_\mu$  neutrino beam at any accelerator experiment would be major evidence for a non-vanishing  $\theta_{13}$ . But unfortunately, in addition to the statistical and systematic uncertainties, correlations and degeneracies between  $\theta_{13}$ ,  $\theta_{\text{atm}}$ ,  $\text{sgn}(\Delta m_{31}^2)$ , and the CP- $\delta$  phase degrade the knowledge of  $\theta_{13}$  [Min02, Hub02]. Even though appearance experiments seem to be the easiest way to measure very small mixing angles, as might be the case for  $\theta_{13}$ , it is of great interest nevertheless to get additional information with another experimental method.

A reactor neutrino experiment, like Double-CHOOZ, is able to measure  $\theta_{13}$  with an independent detection principle (inverse neutron beta decay), and thus different

<sup>2</sup>ICARUS and OPERA results could be combined, leading to a value very close to the ICARUS sensitivity (10 % improvement).

<sup>3</sup>This value takes into account, in a very conservative manner, all correlations and degeneracies. At a fixed  $\delta$  phase taken to be 0, the value quoted would be three times lower.

systematic uncertainties. Unlike appearance experiments, it does not suffer from parameter degeneracies induced by the CP- $\delta$  phase. In addition, thanks to the low  $\bar{\nu}_e$  energy (a few MeV) as well as the very short baselines (a few kilometers) the reactor measurement is not affected by matter effects. As a consequence reactors provide a clean information on  $\sin^2(2\theta_{13})$ . Double-CHOOZ will use two identical detectors at  $\sim 150$  m and 1.05 km from the CHOOZ-B nuclear power plant cores. The near detector is used to monitor both the reactor  $\bar{\nu}_e$  flux and energy spectrum, while the second detector is dedicated to the search for a deviation from the expected  $(1/\text{distance})^2$  behavior, tagging an oscillation effect. For  $\Delta m_{\text{atm}}^2 = 2.0 \cdot 10^{-3} \text{ eV}^2$  we expect a sensitivity of  $\sin^2(2\theta_{13}) < 0.03$  (90 % C.L.) after three years of data taking.

In conclusion, due to the fundamental interest of  $\theta_{13}$  as well as the importance of its amplitude for the design of future neutrino experiments dedicated to CP- $\delta$ , independent  $\theta_{13}$ -dedicated experiments are mandatory. To accomplish this goal, both reactor and accelerator programs should provide the required independent and complementary results [RWP04].



## Chapter 2

# Searching for $\sin^2(2\theta_{13})$ with reactors

### 2.1 Neutrino oscillations

Neutrino flavor transitions have been observed in atmospheric, solar, reactor and accelerator neutrino experiments. To explain these transitions, extensions to the minimal Standard Model of particle physics are required. The simplest and most widely accepted extension is to allow neutrinos to have masses and mixing, similar to the quark sector. The flavor transitions can then be explained by neutrino oscillations.

#### 2.1.1 Quark mixing

The Wolfenstein parameterization of the CKM matrix [PDG00] is based on the very small mixing between the quarks. The mixing matrix is almost the identity matrix with only small corrections for the off-diagonal elements. It uses the observed quark mixing angles hierarchy<sup>1</sup> to introduce an expansion parameter  $\lambda$  describing the mixing between  $u$  and  $s$  quarks. This leads to the parameterization

$$V_{\text{CKM}} \simeq \begin{pmatrix} 1 - \frac{1}{2}\lambda^2 & \lambda & A\lambda^3(\rho - i\eta) \\ -\lambda & 1 - \frac{1}{2}\lambda^2 & A\lambda^2 \\ A\lambda^3(1 - \rho + i\eta) & -A\lambda^2 & 1 \end{pmatrix} + \mathcal{O}(\lambda^4), \quad (2.1)$$

where  $\lambda$  corresponds to the Cabibbo angle  $\sin\theta_C \simeq 0.22$ , and the other parameters are roughly  $A \simeq 0.83$ ,  $\rho \simeq 0.23$  and  $\eta \simeq 0.36$  [PDG00]. The latter parameter describes  $CP$  violation in the quark sector; all such effects are proportional to [Jar85]

$$J_{CP} \simeq -A^2 \lambda^6 \eta \sim -3 \cdot 10^{-5}. \quad (2.2)$$

Therefore,  $CP$  violation in the quark sector is a small effect.

#### 2.1.2 Neutrino mixing

The neutrino oscillation data can be described within a three neutrino mixing scheme, in which the flavor states  $\nu_\alpha$  ( $\alpha = e, \mu, \tau$ ) are related to the mass states  $\nu_i$  ( $i = 1, 2, 3$ ) through the PMNS (Pontecorvo-Maki-Nakagawa-Sakata) unitary lepton mixing matrix.

---

<sup>1</sup> $\theta_{12} \sim 0.1 > \theta_{23} \sim 0.01 > \theta_{13} \sim 0.001$

It can be parameterized as  $U_{\text{PMNS}} =$

$$\begin{aligned} & \begin{pmatrix} 1 & & \\ & c_{23} & s_{23} \\ & -s_{23} & c_{23} \end{pmatrix} \begin{pmatrix} c_{13} & & s_{13}e^{-i\delta} \\ & 1 & \\ -s_{13}e^{i\delta} & & c_{13} \end{pmatrix} \begin{pmatrix} c_{12} & s_{12} \\ -s_{12} & c_{12} \\ & & 1 \end{pmatrix} \begin{pmatrix} 1 & & \\ & e^{i\alpha} & \\ & & e^{i\beta} \end{pmatrix} \\ & = \\ & \begin{pmatrix} c_{13}c_{12} & & c_{13}s_{12} & s_{13}e^{-i\delta} \\ -c_{23}s_{12} - s_{13}s_{23}c_{12}e^{i\delta} & c_{23}c_{12} - s_{13}s_{23}s_{12}e^{i\delta} & c_{13}s_{23} & \\ s_{23}s_{12} - s_{13}c_{23}c_{12}e^{i\delta} & -s_{23}c_{12} - s_{13}c_{23}s_{12}e^{i\delta} & c_{13}c_{23} & \end{pmatrix} \begin{pmatrix} 1 & & \\ & e^{i\alpha} & \\ & & e^{i\beta} \end{pmatrix} \end{aligned} \quad (2.3)$$

where  $c_{ij} = \cos\theta_{ij}$  and  $s_{ij} = \sin\theta_{ij}$ ,  $\delta$  is a Dirac  $CP$  violating phase,  $\alpha$  and  $\beta$  are Majorana  $CP$  violating phases, not considered in the following. Up to now, the angles  $\theta_{12}$  and  $\theta_{23}$  are probed via the oscillations of solar/reactor and atmospheric neutrinos, while the angle  $\theta_{13}$  is mainly constrained by the CHOOZ reactor experiment; the Dirac phase  $\delta$  has not been constrained yet.

The factorized form of this PMNS mixing matrix is often used to identify the mixing angles reported by the experiments <sup>2</sup>

$$\theta_{23} \cong \theta_{\text{atm}}, \quad \theta_{12} \cong \theta_{\text{sol}}, \quad \text{and} \quad \theta_{13} \cong \theta_{\text{CHOOZ}}. \quad (2.4)$$

The relevant formula for the oscillation probabilities is

$$P(\nu_\alpha \rightarrow \nu_\beta) = \delta_{\alpha\beta} - 2 \text{Re} \sum_{j>i} U_{\alpha i} U_{\alpha j}^* U_{\beta i}^* U_{\beta j} \left( 1 - \exp \frac{i\Delta m_{ji}^2 L}{2E} \right), \quad (2.5)$$

where  $\Delta m_{ji}^2 = m_j^2 - m_i^2$ .

Since the identification of the MSW-LMA mechanism as the solution of the solar neutrino anomaly [SK02b, SNO02, KAM02], we now know that the mass eigenstate with the larger electron neutrino component has the smaller mass (state 1). Solar neutrino oscillations occur then mainly together with the little heavier state 2:

$$\Delta m_{21}^2 = m_2^2 - m_1^2 \equiv \Delta m_{\text{sol}}^2 > 0. \quad (2.6)$$

The large mass squared difference measured in the atmospheric sector is therefore the splitting between the mass eigenstate 3 and the more closely spaced 1 or 2. In addition, the CHOOZ reactor neutrino experiment shows that the mass eigenstate 3 has only a very small electron neutrino component. In this description, the sign of the splitting between state 3 and states 1 and 2 is unknown; this leads to two possibilities of mass ordering:

$$|\Delta m_{32}^2| = |m_3^2 - m_2^2| \equiv \Delta m_{\text{atm}}^2. \quad (2.7)$$

Thus, one defines the normal hierarchy (NH) scenario  $m_3 > m_2 > m_1$ , and the inverted hierarchy scenario (IH)  $m_2 > m_1 > m_3$ . The determination of the sign of  $\Delta m_{32}^2$  is one of the next goals in neutrino oscillation physics.

## 2.2 Measurement of $\text{sin}^2(2\theta_{13})$ with reactor $\bar{\nu}_e$

### 2.2.1 Reactor $\bar{\nu}_e$ flux

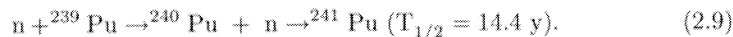
The fissionable material in the CHOOZ pressurized water reactors (PWR) mainly consists of  $^{235}\text{U}$  and  $^{239}\text{Pu}$ , which undergo thermal neutron fission. The fresh fuel is

<sup>2</sup>Thanks to the smallness of  $\frac{\Delta m_{\text{sol}}^2}{\Delta m_{\text{atm}}^2}$  and  $\text{sin}^2\theta_{\text{CHOOZ}}$ .

enriched to about 3.5 % in  $^{235}\text{U}$ . Fast fission neutrons are moderated by light water pressurized to 150 bar. The dominant natural uranium isotope,  $^{238}\text{U}$ , is fissile only for fast neutrons (threshold of 0.8 MeV) but it also generates fissile  $^{239}\text{Pu}$  by thermal neutron capture,



The  $^{241}\text{Pu}$  isotope is produced in a manner similar to  $^{239}\text{Pu}$



As the reactor operates, the concentration of  $^{235}\text{U}$  decreases, while that of  $^{239}\text{Pu}$  and  $^{241}\text{Pu}$  increases. After about one year, the reactor is stopped and one third of the fuel elements are replaced. Typical numbers for an annual cycle are given in Table 2.1. Due to the threshold of the detection reaction at 1.8 MeV only the

	Mean energy per fission (MeV)	Refueling cycle	
		beginning	end
$^{235}\text{U}$	$201.7 \pm 0.6$	60.5 %	45.0 %
$^{238}\text{U}$	$205.0 \pm 0.9$	7.7 %	8.3 %
$^{239}\text{Pu}$	$210.0 \pm 0.9$	27.2 %	38.8 %
$^{241}\text{Pu}$	$212.4 \pm 1.0$	4.6 %	7.9 %

Table 2.1: Typical fuel composition for an annual cycle of a PWR power station, for the four main isotopes, normalized to 100 %. There are also other isotopes, not included here, which contribute for a few percents.

most energetic antineutrinos are detected; they correspond to the decay of fission products with the highest Q-values and hence to the shortest lived. The detected antineutrinos thus closely follow changes in power. In particular spent fuel elements which are kept on site out of the core contain only long lived emitters with a low Q-value; their contribution to the detected  $\bar{\nu}_e$  signal is negligible. Measurements of the neutrino rate per fission have been performed for  $^{235}\text{U}$ ,  $^{239}\text{Pu}$  and  $^{241}\text{Pu}$  by Borovoi et al. [Bor83] and Schreckenbach et al. [Sch85, Hah89]. The latter measurement includes the shape of the energy spectrum, with a 2 % bin-to-bin accuracy and an overall normalization error of 2.8 %. The measurement performed by [Sch85] can be compared with several computations and is found to be in good agreement with that of [Kla82, Vog81]. We will therefore use this computation for the  $^{238}\text{U}$  neutrino rate, which has never been measured. The  $^{238}\text{U}$  contribution to the total number of fissions is  $\sim 10$  %, and is therefore not a major source of error. The antineutrino spectra of the four dominant fissioning isotopes are shown in Figure 2.1. During the cycle, the contributions of the different fissile isotopes to energy production evolve. For fresh fuel,  $^{235}\text{U}$  fissions dominate, whereas  $^{238}\text{U}$  fissions amount for a few times less. Quickly after the beginning of the cycle  $^{239}\text{Pu}$  gives an important contribution (see Figure 2.2).

### 2.2.2 $\bar{\nu}_e$ detection principle

Reactor antineutrinos are detected through their interaction by inverse neutron decay (threshold of 1.806 MeV)

$$\bar{\nu}_e + p \rightarrow e^+ + n. \quad (2.10)$$

The cross section for inverse  $\beta$ -decay has approximately the form

$$\sigma(E_{e^+}) \simeq \frac{2\pi^2 \hbar^3}{m_e^2 f \tau_n} p_{e^+} E_{e^+}, \quad (2.11)$$

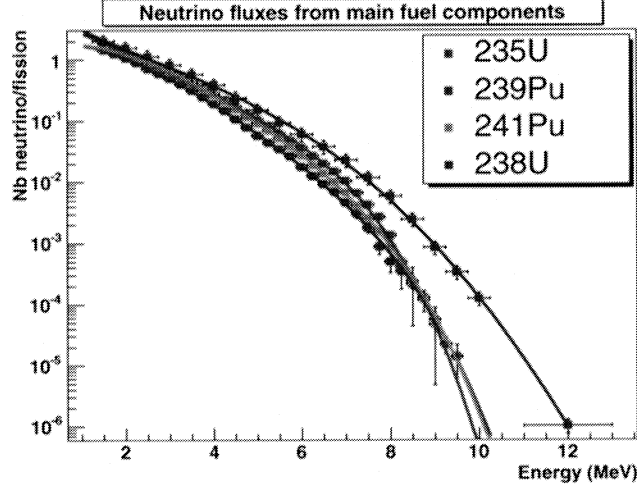


Figure 2.1:  $\bar{\nu}_e$  spectra of the four dominant isotopes with their experimental error bars ( $^{238}\text{U}$  spectrum has not been measured but calculated).

where  $p_{e^+}$  and  $E_{e^+}$  are the momentum and the energy of the positron<sup>3</sup>,  $\tau_n$  is the lifetime of a free neutron and  $f$  is the free neutron decay phase space factor. As an approximation, we use an averaged fuel composition typical during a reactor cycle corresponding to  $^{235}\text{U}$  (55.6 %),  $^{239}\text{Pu}$  (32.6 %),  $^{238}\text{U}$  (7.1 %) and  $^{241}\text{Pu}$  (4.7 %). The mean energy release per fission  $W$  is then 203.87 MeV and the energy weighted cross section amounts to

$$\langle \sigma \rangle_{\text{fission}} = 5.825 \cdot 10^{-43} \text{ cm}^2 \text{ per fission} . \quad (2.12)$$

The reactor power  $P_{th}$  is related to the number of fissions per second  $N_f$  by

$$N_f = 6.241 \cdot 10^{18} \text{ sec}^{-1} \cdot (P_{th}[\text{MW}] / (W[\text{MeV}])) . \quad (2.13)$$

The event rate at a distance  $L$  from the source, assuming no oscillations, is thus

$$R_L = N_f \cdot \langle \sigma \rangle_{\text{fission}} \cdot n_p \cdot 1 / (4\pi L^2) , \quad (2.14)$$

where  $n_p$  is the number of protons in the target. For the purpose of simple scaling, a reactor with a power of 1  $\text{GW}_{th}$  induces a rate of  $\sim 450$  events per year in a detector containing  $10^{29}$  protons, at a distance of 1 km.

Experimentally one takes advantage of the coincidence signal of the prompt positron followed in space and time by the delayed neutron capture. This very clear signature allows to strongly reject the accidental backgrounds. The energy of the incident antineutrino is then related to the energy of the positron by the relation

$$E_{\bar{\nu}_e} = E_{e^+} + (m_n - m_p) + O(E_{\bar{\nu}_e} / m_n) . \quad (2.15)$$

Experimentally, the visible energy seen in the detector is given by  $E_{\text{vis}} = E_{e^+} + 511 \text{ keV}$ , where the additional 511 keV come from the annihilation of the positron with an electron when it stops in the matter.

<sup>3</sup> $E_{e^+}$  is the sum of the rest mass and kinetic energy of the positron.

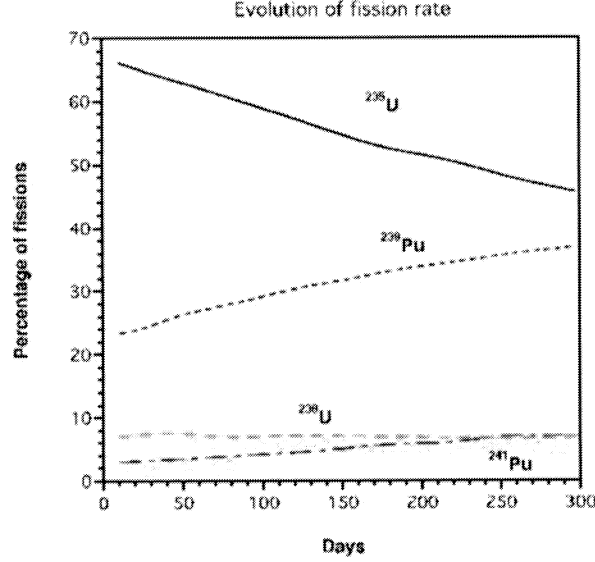


Figure 2.2: Percentage of fissions of the four dominant fissile isotopes during 300 days of a typical fuel cycle.

### 2.2.3 $\bar{\nu}_e$ oscillations

Reactor neutrino experiments measure the survival probability  $P_{\bar{\nu}_e \rightarrow \bar{\nu}_e}$  of the electron antineutrinos emitted from the nuclear power plant<sup>4</sup>. This survival probability does not depend on the  $\delta$ -CP phase. Furthermore, because of the low energy as well as the short baseline considered, matter effects are negligible [Min02]. Assuming a “normal” mass hierarchy scenario,  $m_1 < m_2 < m_3$ , the  $\bar{\nu}_e$  survival probability can be written [Bil01, Pet01]

$$\begin{aligned}
 P_{\bar{\nu}_e \rightarrow \bar{\nu}_e} &= 1 - 2 \sin^2 \theta_{13} \cos^2 \theta_{13} \sin^2 \left( \frac{\Delta m_{31}^2 L}{4E} \right) \\
 &\quad - \frac{1}{2} \cos^4 \theta_{13} \sin^2(2\theta_{12}) \sin^2 \left( \frac{\Delta m_{21}^2 L}{4E} \right) \\
 &\quad + 2 \sin^2 \theta_{13} \cos^2 \theta_{13} \sin^2 \theta_{12} \left( \cos \left( \frac{\Delta m_{31}^2 L}{2E} - \frac{\Delta m_{21}^2 L}{2E} \right) - \cos \left( \frac{\Delta m_{31}^2 L}{2E} \right) \right)
 \end{aligned} \tag{2.16}$$

The first two terms in Eq. 2.2.3 contain respectively the atmospheric driven ( $\Delta m_{31}^2 = \Delta m_{\text{atm}}^2$ ) and solar driven ( $\Delta m_{21}^2 = \Delta m_{\text{sol}}^2$ ,  $\theta_{12} \sim \theta_{\text{sol}}$ ) contributions, while the third term, absent from *any* two-neutrino mixing model, is an interference between solar and atmospheric driven oscillations whose amplitude is a function of  $\theta_{13}$ . Thus, up to second order in  $\sin 2\theta_{13}$  and  $\alpha = \frac{\Delta m_{\text{sol}}^2}{\Delta m_{\text{atm}}^2}$  the survival probability can be expressed as

$$P_{\bar{\nu}_e \rightarrow \bar{\nu}_e} \simeq 1 - \sin^2 2\theta_{13} \sin^2(\Delta m_{31}^2 L/4E) + \alpha^2 (\Delta m_{31}^2 L/4E)^2 \cos^4 \theta_{13} \sin^2 2\theta_{12}, \tag{2.17}$$

<sup>4</sup>The low neutrino energy (a few MeV) does not allow any appearance measurement.

where the third term on the right side can safely be neglected given the current range (90 % error intervals) of mixing parameters found in neutrino oscillation experiments<sup>5</sup> [SK02a, SK04a]:

$$\begin{aligned}
(\Delta m_{\text{atm}}^2)_{\text{SK-I}} &= 2.0_{-0.7}^{+1} \cdot 10^{-3} \text{ eV}^2 \\
(\sin^2 2\theta_{23})_{\text{SK-I}} &= 1_{-0.1}^{+0} \\
(\Delta m_{\text{atm}}^2)_{\text{SK-L/E}} &= 2.4_{-0.5}^{+0.6} \cdot 10^{-3} \text{ eV}^2 \\
(\sin^2 2\theta_{23})_{\text{SK-L/E}} &= 1_{-0.1}^{+0} \\
\Delta m_{\text{sol}}^2 &= 7.0_{-3}^{+2} \cdot 10^{-5} \text{ eV}^2 \\
\sin^2(2\theta_{12}) &= 0.8_{-0.2}^{+0.2} .
\end{aligned}$$

Reactor experiments thus provide a clean measurement of the mixing angle  $\theta_{13}$ , free from any contamination coming from matter effects and other parameter correlations or degeneracies [Min02, Hub02]. Therefore they are exclusively dominated by statistical and systematic errors.

### 2.3 Complementarity with Superbeam experiments

A very detailed comparison of reactor antineutrino experiments with superbeams is described in [Min02, Hub02]. Forthcoming accelerator neutrino experiments, or superbeams, will search for a  $\nu_e$  appearance signal. The appearance probability  $P_{\nu_\mu \rightarrow \nu_e}$  with terms up to second order, *e.g.*, proportional to  $\sin^2 2\theta_{13}$ ,  $\sin 2\theta_{13} \cdot \alpha$ , and  $\alpha^2$ , can be written as:

$$\begin{aligned}
P_{\nu_\mu \rightarrow \nu_e} &\simeq \sin^2 2\theta_{13} \sin^2 \theta_{23} \sin^2 (\Delta m_{31}^2 L/4E) \\
&\mp \alpha \sin 2\theta_{13} \sin \delta \sin 2\theta_{12} \sin 2\theta_{23} \\
&\quad (\Delta m_{31}^2 L/4E) \sin^2 (\Delta m_{31}^2 L/4E) \\
&- \alpha \sin 2\theta_{13} \cos \delta \sin 2\theta_{12} \sin 2\theta_{23} \\
&\quad (\Delta m_{31}^2 L/4E) \cos (\Delta m_{31}^2 L/4E) \sin (\Delta m_{31}^2 L/4E) \\
&+ \alpha^2 \cos^2 \theta_{23} \sin^2 2\theta_{12} (\Delta m_{31}^2 L/4E)^2, \tag{2.18}
\end{aligned}$$

where the sign of the second term refers to neutrinos (minus) or antineutrinos (plus). From Equation 2.18 one sees that superbeams suffer from parameter correlations and degeneracies coming from the different combinations of parameters. Many of the degeneracy problems originate in the summation of the four terms in Equation 2.18, since changes in one parameter value often can be compensated by adjusting another one in a different term. This leads to the  $(\delta, \theta_{13})$  [Bur01],  $\text{sgn}(\Delta m_{31}^2)$  [Min01], and  $(\theta_{23}, \pi/2 - \theta_{23})$  [Fog98] degeneracies, *e.g.* an overall “eight-fold” degeneracy [Bar02, Min01]. Table 2.2 summarizes the sensitivity of accelerator and Double-CHOOZ experiments.

<sup>5</sup>Two different best fit values for the atmospheric mass splitting have been released by the Super-Kamiokande collaboration, based on two different analyzes of the same data.

	Chooz	Beams	Double-CHOOZ	T2K
$\sin^2(2\theta_{13})$ sensitivity limit (90 % CL)				
$\sin^2(2\theta_{13})$	0.2	0.061	0.032	0.023
$\sin^2(2\theta_{13})_{\text{eff}}$	0.2	0.026	0.032	0.006
Measurements for large $\sin^2(2\theta_{13}) = 0.1$ (90 % CL)				
$\sin^2(2\theta_{13})$	–	$0.1^{+0.104}_{-0.052}$	$0.1^{+0.034}_{-0.033}$	$0.1^{+0.067}_{-0.034}$

Table 2.2: Comparison of the sensitivity of reactor and accelerator based future neutrino experiments. The results of the table have been extracted from [Hub04]. "Beams" is the combination of the forthcoming MINOS, ICARUS, and OPERA experiments. Results for accelerator experiments are given for five years of data taking. Results for Double-CHOOZ are given for three years of operation. The line starting by " $\sin^2(2\theta_{13})$ " provides the results of the computation taking into account all correlation and degeneracy effects, while the line starting by  $\sin^2(2\theta_{13})_{\text{eff}}$  give the results of a similar computation performed after "switching off" those effects.





## Chapter 3

# Overview of the Double-CHOOZ experiment

This section is an overview of the Double-CHOOZ experiment. The Double-CHOOZ technology of reactor neutrino detection is based on experience obtained in numerous experiments: Goesgen [GOE86], Bugey [BUG96] (at short distances), CHOOZ [CHO98, CHO99, CHO00, CHO03], Palo Verde [PV01] (at km scale distance) CTF [CTF98], Borexino [Sch99], Kamland [KAM02] (distances of a few hundred km). Therefore, no long term R&D program has to be conducted prior to designing and building the new detector. Nevertheless, in order to be a precision experiment, the Double-CHOOZ design has to be improved with respect to CHOOZ. The liquid scintillator is described in Chapter 5, the calibration in Chapter 6, and the backgrounds in Chapter 7. The systematic error handling is presented in Chapter 8. To conclude, the sensitivity of Double-CHOOZ, taking into account the overall set of systematic errors, is presented in Chapter 9.

### 3.1 The $\bar{\nu}_e$ source

To fulfill the aim of the Double-CHOOZ experiment, precise knowledge of the antineutrino emission in the nuclear core is not crucial thanks to the choice of comparing two similar detectors at different distances, where the near detector measures the flux without  $\bar{\nu}_e$  losses consequent to oscillations. Nevertheless this information is available and will be used for cross checks and other studies of interest (see Appendix A). More details on the  $\bar{\nu}_e$  source will be necessary to do those specific studies with the near detector, such as the  $\bar{\nu}_e$  spectrum and flux expected for a given fuel composition and burn up.

#### 3.1.1 The CHOOZ nuclear reactors

The antineutrinos used in the experiment are those produced by the pair of reactors located at the CHOOZ-B nuclear power station operated by the French company Electricité de France (EDF) in partnership with the Belgian utilities Electrabel S.A./N.V. and Société Publique d'Electricité. They are located in the Ardennes region, northeast of France, very close to the Belgian border, in a loop of the Meuse river (see Figures 3.1 and 3.2). At the CHOOZ site, there are two nuclear reactors, both are of the most recent N4 type (4 steam generators) with a thermal power of 4.27 GW<sub>th</sub>, and recently upgraded from 1.45 GW<sub>e</sub> to 1.5 GW<sub>e</sub>. These reactors are of the Pressurized Water Reactor type (PWR) and are fed with UOx type fuel. They are the most powerful reactor type in operation in the world. One unusual

characteristic of the N4 reactors is their ability to vary their output from 30 % to 95 % of full power in less than 30 minutes, using the so-called gray control rods in the reactor core. These rods are referred to as gray because they absorb fewer free neutrons than conventional black rods. One advantage is a bigger thermal homogeneity. 205 fuel assemblies are contained within each reactor core. The entire reactor vessel is a cylinder of 13.65 meters high and 4.65 meters in diameter. The first reactor started operating at full power in May 1997, and the second one in September of the same year.

### 3.2 Detector site

The Double-CHOOZ experiment will run two almost identical detectors of medium size, containing 12.7 cubic meters of liquid scintillator target doped with 0.1 % of Gadolinium (see Chapter 5). The neutrino laboratory of the first CHOOZ experiment, located 1.05 km from the two cores of the CHOOZ nuclear plant will be used again (see Figure 3.3). This is the main advantage of this site compared with other French locations. We label this site the far detector site or **CHOOZ-far**. A sketch

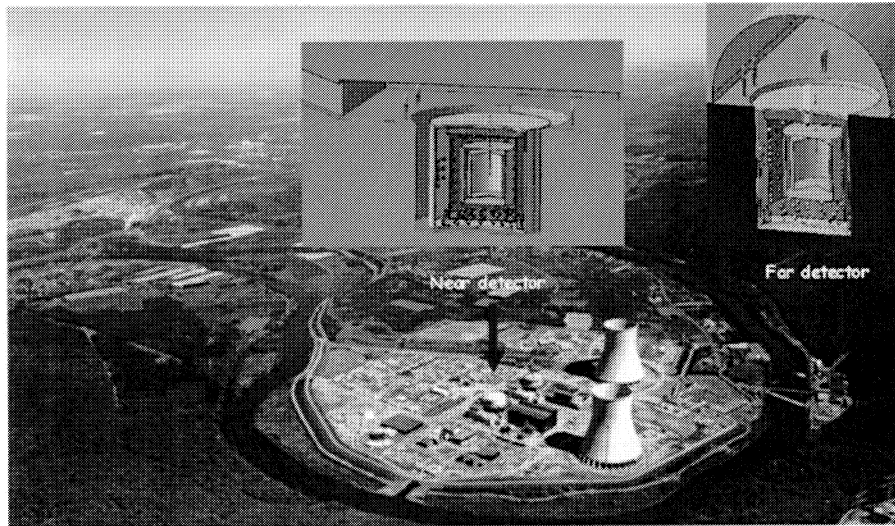


Figure 3.1: Overview of the experiment site.

of the CHOOZ-far detector is shown in Figure 3.4. The CHOOZ-far site is shielded by about 300 m.w.e. of  $2.8 \text{ g/cm}^3$  rocks. Cosmic ray measurements were made with Resistive Plate Chambers and compared with the expected angular distributions. A geological study revealed the existence of several very high density rock layers ( $3.1 \text{ g/cm}^3$  whose positions and orientations were in agreement with the cosmic ray measurements [CHO03]). It is intended to start taking data at CHOOZ-far at the beginning of the year 2007.

In order to cancel the systematic errors originating from the nuclear reactors (lack of knowledge of the  $\bar{\nu}_e$  flux and spectrum), as well as to reduce the set of systematic errors related to the detector and to the event selection procedure, a second detector will be installed close to the nuclear cores. We label this detector site the near site or **CHOOZ-near**. Since no natural hills or underground cavity already exists at this location, an artificial overburden of a few tens of meters height has to

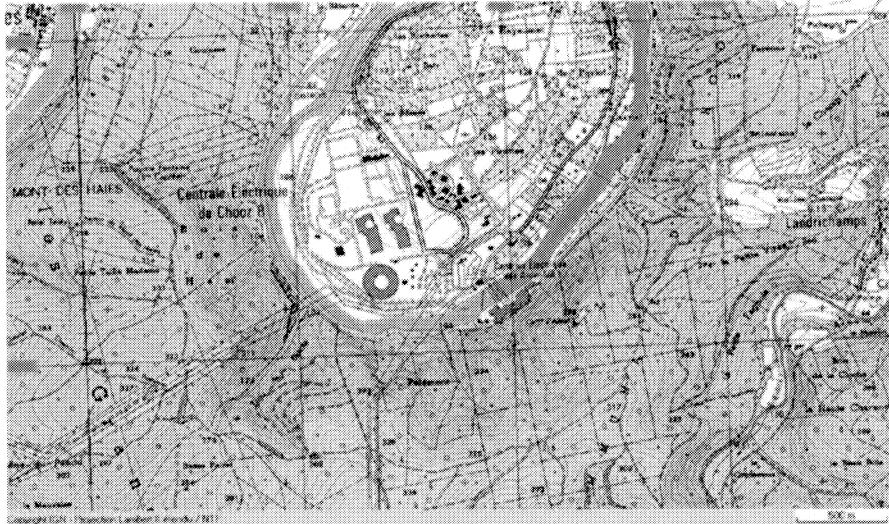


Figure 3.2: Map of the experiment site. The two cores are separated by a distance of 100 meters. The far detector site is located at 1.0 and 1.1 km from the two cores.

be built. The required overburden ranges from 53 to 80 m.w.e. depending on the near detector location, between 100 and 200 meters away from the cores (see Table 3.1). A sketch of this detector is shown in Figure 3.5. After first discussions, this

Distance	Minimal overburden (m.w.e.)	Required overburden (m.w.e.)
100	45	53
150	55	65
200	67.5	80

Table 3.1: Overburden required for the near detector. The second column is the estimation of the minimal overburden required for the experiment. The third column is minimal overburden added to a safety margin.

construction has been considered as technically possible by the power plant company authorities. An initial study has been commissioned by the French electricity power company EDF to determine the best combination of location-overburden and to optimize the cost of the project. Plan is to start to take data at CHOOZ-near at the beginning of the year 2008.

### 3.3 Detector design

The detector design foreseen is an evolution of the detector of the first experiment [CHO03]. To improve the sensitivity of Double-CHOOZ with respect to CHOOZ it is planned to increase statistics and to reduce the systematic errors and backgrounds.

In order to increase the exposure to 60,000  $\bar{\nu}_e$  events at CHOOZ-far (statistical error of 0.4 %) it is planned to use a target cylinder of 120 cm radius and 280 cm



Figure 3.3: Picture of the CHOOZ-far detector site taken in September 2003. The original CHOOZ laboratory hall constructed by EDF, located close to the old CHOOZ-A underground power plant, is still in perfect condition and could be re-used without additional civil engineering construction.

height, providing a volume of  $12.7 \text{ m}^3$ ,  $\sim 2.5$  larger than in CHOOZ. In addition, the data taking period will be extended to at least three years, and the overall data taking efficiency will be improved. The global load factor of the reactor, i.e. the average reactor efficiency, is about 80 %, whereas it was significantly lower for the CHOOZ experiment performed during the power plant commissioning. In addition, the detector efficiency will be slightly improved. The background level at CHOOZ-far will be decreased to have a signal to noise ratio over 100 (about 25 in CHOOZ).

The near and far detectors will be identical inside the PMTs supporting structure. This will allow a relative normalization systematic error of  $\sim 0.6 \%$  (see Chapter 8). However, due to the different overburdens (60-80 to 300 m.w.e.), the outer shielding will not be identical since the cosmic ray background varies between CHOOZ-near and CHOOZ-far. The overburden of the near detector has been chosen in order to keep the signal to background ratio above 100. Under this condition, even a knowledge of the backgrounds within a factor two keeps the associated systematic error well below the percent (assuming that its energy distribution is known).

The detector design has been intensively studied and tested with Monte-Carlo simulations, using two different softwares derived from the simulation of the CHOOZ and Borexino experiments (see Chapter 4). In order to increase the width of the liquid buffers protecting the  $\bar{\nu}_e$  target, the 1 meter low radioactivity sand shielding of CHOOZ will be replaced by a 15 cm metal shielding, steel or iron (this is used to reduce the external gamma rays coming from the rock.) This will increase the size of the liquid active buffer and will thus improve the rejection of muon induced backgrounds (see Chapter 7). Starting from the center of the target the detector elements are as follows (see Figures 3.4 and 3.5)

- $\bar{\nu}_e$  target

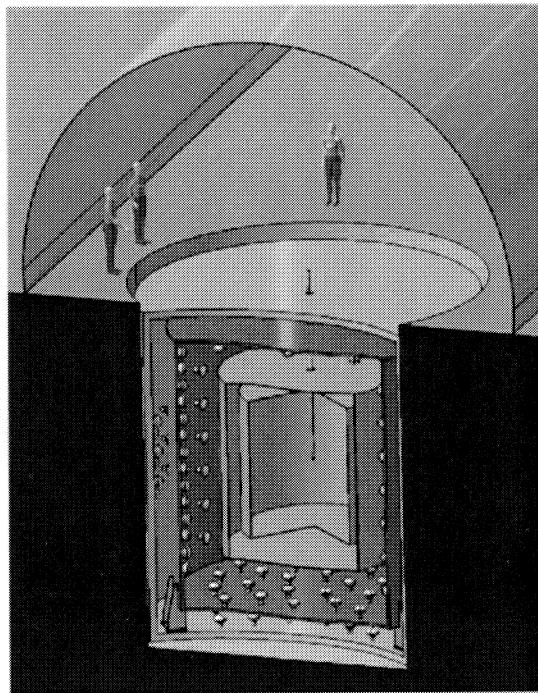


Figure 3.4: The new CHOOZ-far detector, at the former CHOOZ underground site. The detector is located in the tank used for the CHOOZ experiment (7 meters high and 7 meters in diameter) that is still available. About  $12.7 \text{ m}^3$  of a dodecane+PXE based liquid scintillator doped with gadolinium is contained in a transparent acrylic cylinder surrounded by the  $\gamma$ -catcher region and the buffer. The design goal is to achieve a light yield of about 200 pe/MeV (see Chapter 4) which requires an optical coverage of about 15 %, provided by the surrounding PMTs. The PMTs are mounted on a cylindrical structure which separates optically the outer part of the detector, which is used as a muon veto.

A 120 cm radius, 280 cm height, 6-10 mm width acrylic cylinder, filled with 0.1 % Gd loaded liquid scintillator target (see Chapter 5).

- **$\gamma$ -catcher**  
A 60 cm buffer of non-loaded liquid scintillator with the same optical properties as the  $\bar{\nu}_e$  target (light yield, attenuation length), in order to get the full positron energy as well as most of the neutron energy released after neutron capture.
- **Buffer**  
A 95 cm buffer of non scintillating liquid, to decrease the level of accidental background (mainly the contribution from photomultiplier tubes radioactivity).
- **PMT supporting structure**
- **Veto system**  
A 60 cm veto region filled with liquid scintillator for the far detector, and a slightly larger one (about 100 cm) for the near detector.

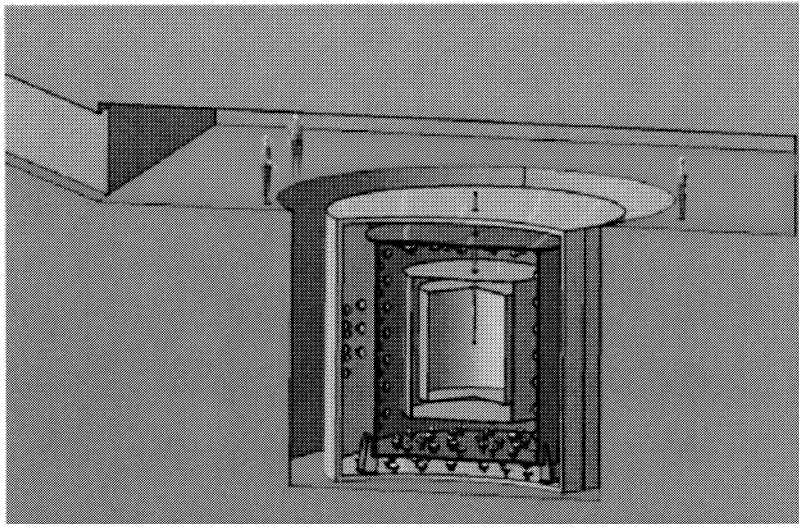


Figure 3.5: The CHOOZ-near detector at the new underground site, close to the reactor cores. This detector is identical to the CHOOZ-far detector up to and including the PMT surface. The veto region will be enlarged to better reject the cosmic muon induced backgrounds (see Chapter 7).

Compared to previous scintillator  $\bar{\nu}_e$  detectors, the Double-CHOOZ experiment will use cylindrical targets; Monte-Carlo simulation shows that the spatial reconstruction in a cylinder is suitable for the experiment. A spherical configuration gives slightly better results, however. Each parameter of the detector is being studied by Monte-Carlo simulation in order to define the tolerance on the differences between the two detectors (see Chapter 4). The inner volume dimensions as well as the shape of the target vessels are still preliminary, within a few tens of percents, and could change prior to the publication of the proposal.

### 3.3.1 Experimental errors and backgrounds

In the first CHOOZ experiment, the total systematic error amounted to 2.7 % [CHO03]. Table 3.2 summarizes the control of the systematic uncertainties that had been achieved in the first CHOOZ experiment as well as the goal of Double-CHOOZ. The main uncertainties at CHOOZ came from the 2 % only knowledge of the antineutrino flux coming from the reactor. This systematic error vanishes by adding a near detector to monitor the power plant antineutrino flux and energy spectrum. A complete description of the systematic uncertainties is given in Chapter 8. The main challenge of the Double-CHOOZ experiment is to decrease the overall systematic error from 2.7 % to 0.6 %. The strategy is to improve the detector design, to rely on the comparison of the two detectors, and to reduce the number of analysis cuts. The non-scintillating buffer will reduce the singles rates in each detector by two orders of magnitude with respect to CHOOZ. This allow to lower the positron threshold down to  $\sim 500$  keV, well below the 1.022 MeV physical threshold of the inverse beta decay reaction. A very low threshold has three advantages:

- The systematic error due to this threshold is suppressed. It was one of the largest source of systematic error, 0.8 % in CHOOZ [CHO03].
- The background below the physical 1 MeV threshold can be measured.

- The onset of the positron spectrum provides an additional calibration point between the near and far detectors.

This reduction of the singles events relaxes or even suppresses the localization cuts, such as the distance of an event to the PMT surface and the distance between the positron and the neutron. These cuts, used in CHOOZ [CHO03], are difficult to calibrate and have to be avoided or relaxed in Double-CHOOZ. The remaining event selection cuts will have to be calibrated between the two detectors with a very high precision. Most important will be the calibration of the energy selection of the delayed neutron after its capture on a Gd nucleus (with a mean energy release of 8 MeV gammas). The requirement is  $\sim 100$  keV on the precision of this cut between both detectors, which is feasible with standard techniques using radioactive sources (energy calibration) and lasers (optical calibrations) at different positions throughout the detector active volume (see Chapter 6). The sensitivity of a reactor experiment of Double-CHOOZ scale ( $\sim 300$  GW<sub>th</sub>.ton.year) is mostly given by the total number of events detected in the far detector. The requirement on the positron energy scale is then less stringent since the weight of the spectrum distortion is low in the analysis. (This is being studied by simulation.) A detailed

	CHOOZ	Double-CHOOZ
Reactor cross section	1.9 %	—
Number of protons	0.8 %	0.2 %
Detector efficiency	1.5 %	0.5 %
Reactor power	0.7 %	—
Energy per fission	0.6 %	—

Table 3.2: Summary of the systematic errors in CHOOZ and Double-CHOOZ (goal). The first line, “Reactor cross section”, accounts for the uncertainties on the neutrino flux as well as the inverse neutron beta decay cross section. A two  $\bar{\nu}_e$  detectors concept makes the experiment largely insensitive to the “Reactor cross section” and the reactor power uncertainties. The number of protons in the first acrylic vessel targets as well as the detection efficiencies have then to be calibrated between the two detectors, but only in a relative sense.

background study is presented in Chapter 7. In CHOOZ the dominant correlated proton recoil background was measured to be about one event per day [CHO03]. At CHOOZ-far the active buffer will be increased, with a solid angle for the background being almost unchanged. This together with a signal increased by about a factor of 3 will fulfill the requirement of a signal to noise ratio greater than 100. At CHOOZ-near, due to the shallow depth between 60 and 80 m.w.e, the cosmic ray background will be more important. If, for instance, the CHOOZ-near detector is located 150 meters from the nuclear cores, the signal will be a few thousand events per day, while the muon rate is expected to be a factor of ten less. A dead time of about 500  $\mu$ sec will be applied to each muon<sup>1</sup>, leading to a global dead time of about 30 %. A few tens of recoil proton events per day, mimicking the  $\bar{\nu}_e$  signal, are expected while the estimate of the muon induced cosmogenic events (<sup>9</sup>Li and <sup>8</sup>He) is less than twenty per day with a large uncertainty (this last point is being carefully studied). This fulfills the requirement of a signal to noise ratio greater than 100 at CHOOZ-near.

<sup>1</sup>This is a conservative number that could be reduced.



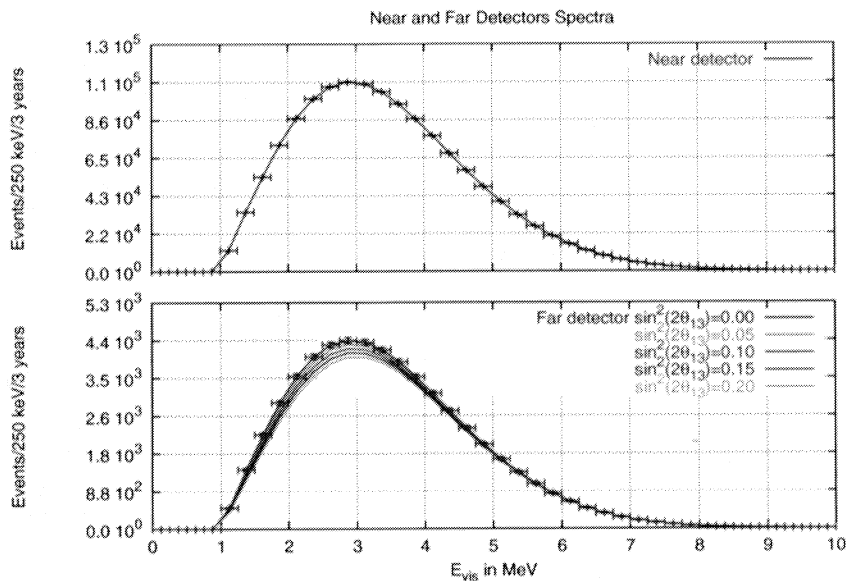


Figure 3.6: Positron spectrum (visible energy, MeV) simulated for the CHOOZ-near and far detectors

### 3.3.2 Sensitivity

A detailed study of the Double-CHOOZ sensitivity is presented in Chapter 9. From the simulations, we expect a sensitivity of  $\sin^2(2\theta_{13}) < 0.03$  at 90 % C.L. for  $\Delta m_{\text{atm}}^2 = 2.0 \cdot 10^{-3} \text{ eV}^2$  (best fit value of Super-Kamiokande [SK02a]), after three years of operation. According to the latest Super-Kamiokande L/E analysis the best mass splitting is  $\Delta m_{\text{atm}}^2 = 2.4 \cdot 10^{-3} \text{ eV}^2$  [SK04a]. The Double-CHOOZ sensitivity would then be  $\sin^2(2\theta_{13}) < 0.025$ . A study of the evolution of the sensitivity with respect to the luminosity is presented in Figure 3.7 [Hub04]. A sensitivity of  $\sim 0.05$  is reachable within the first year of operation with 2 detectors. These estimates are based on the assumptions that the relative normalization error between the near and far detectors could be kept at 0.6 %, and that the backgrounds at both sites amount to 1 % of the  $\bar{\nu}_e$  signal (we assume those backgrounds to be known within a factor of two).

The effect of  $\bar{\nu}_e$  oscillations on the positron spectrum is displayed in Figure 3.8, for different values of  $\Delta m_{\text{atm}}^2$  and  $\sin^2(2\theta_{13})$ . For  $\Delta m_{\text{atm}}^2 \gtrsim 2.0 \cdot 10^{-3} \text{ eV}^2$  a significant shape distortion is expected at the onset of the energy spectrum. Assuming  $\sin^2(2\theta_{13}) = 0.15$ , the ratio of the near and far detector spectrum is presented in Figure 3.9, with the expected statistical error bars ( $1 \sigma$ ) after three years of data taking. It is worth mentioning that the 1.05 km average baseline at CHOOZ is not optimal (the optimal distance should be roughly 1.5 km) compared to the first oscillation maximum if the atmospheric mass splitting is  $\Delta m_{\text{atm}}^2 = 2.0 \cdot 10^{-3} \text{ eV}^2$ . Nevertheless, a new Super-Kamiokande analysis of the data indicates  $1.9 \cdot 10^{-3} \text{ eV}^2 < \Delta m_{\text{atm}}^2 < 3.0 \cdot 10^{-3} \text{ eV}^2$  (90 % C.L.), with a best fit at  $\Delta m_{\text{atm}}^2 = 2.4 \cdot 10^{-3} \text{ eV}^2$  [SK04a]. A shorter baseline is compensated by higher

<sup>2</sup>The sensitivity of the other experiments is as well better for higher  $\Delta m_{\text{atm}}^2$ .



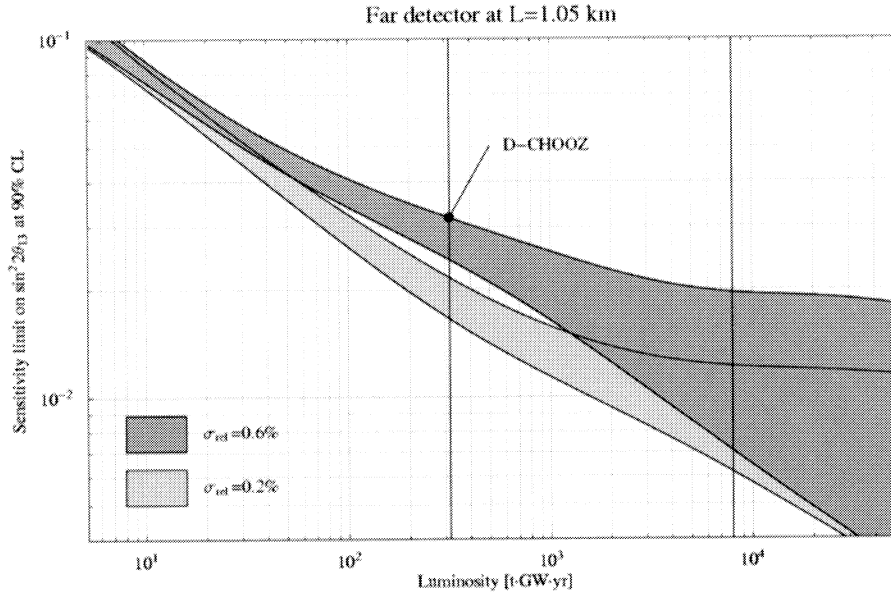


Figure 3.7: Luminosity scaling of the Double-CHOOZ  $\sin^2(2\theta_{13})$  sensitivity at the 90 % C.L.. Here,  $\Delta m_{\text{atm}}^2 = 2.0 \cdot 10^{-3} \text{ eV}^2$  is assumed to be known within 5 %. The relative normalisation error between the two detectors is taken to be (0.2 %)0.6 % for the light (dark) shaded regions. Correlated backgrounds with known shapes account for 1 % and are supposed to be known within 50 %. A 0.5 % “Flat” bin-to-bin uncorrelated background component as been accounted as well (known within 50 %). A luminosity of 300  $\text{GW}_{\text{th}} \cdot \text{ton} \cdot \text{year}$  (left vertical line) correspond approximately to the setup of the Double-CHOOZ experiment as described in this Letter of Intent ( $\sin^2(2\theta_{13}) < 0.03$  within 3 years of data taking). However, a luminosity of 8000  $\text{GW}_{\text{th}} \cdot \text{ton} \cdot \text{year}$  (right vertical line) would describe a  $\sim 300$  tons next detector generation at Chooz [Hub04]

statistics for a fixed size detector. However, a value of  $\Delta m_{\text{atm}}^2 < 1.5 \cdot 10^{-3} \text{ eV}^2$  would restrict the absolute potential of the Double-CHOOZ experiment (see Chapter 9).

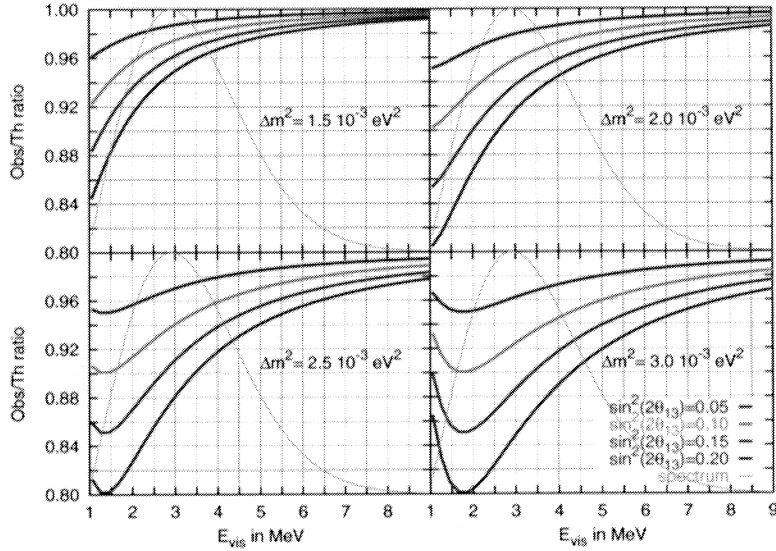


Figure 3.8: Ratio of expected number of  $\bar{\nu}_e$  events in the far detector with respect to the no oscillations scenario, after 3 years data taking, for different values of  $\Delta m_{\text{atm}}^2$  and  $\sin^2(2\theta_{13})$ .

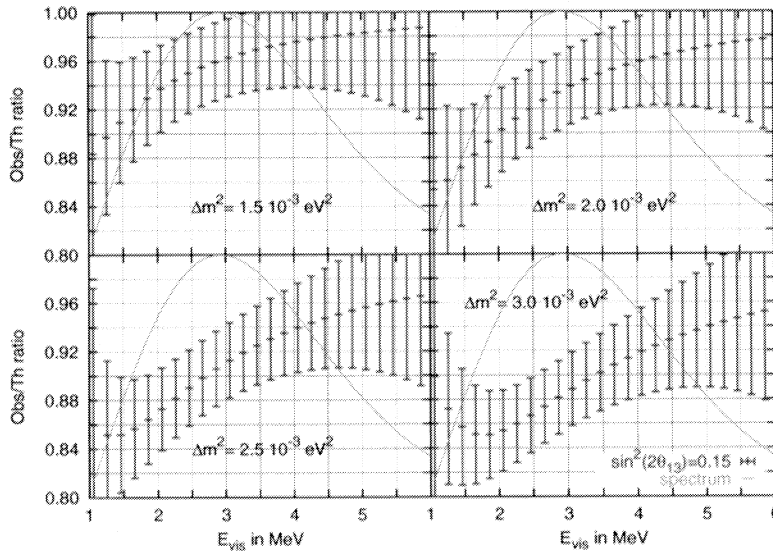


Figure 3.9: Ratio of observed number of events in the far detector with respect to the no oscillations scenario, after 3 years data taking, for  $\sin^2(2\theta_{13}) = 0.15$  and different values of  $\Delta m_{\text{atm}}^2$ . The error bars plotted here are only statistical ( $1\sigma$ ). The positron spectrum shape is also displayed in the background. The potential of the experiment to exclude  $\sin^2(2\theta_{13}) = 0$  may be seen as a deviation from unity in the ratio. Note that in some cases spectral information may be important. The largest spectrum deviation effect is located at the onset of the spectrum, below 4 MeV.

## Chapter 4

# Detector design and simulation

In this section we describe the detector design envisaged for the Double-CHOOZ experiment. Although the generic design is almost complete, some specific technical solutions are still preliminary and could evolve prior to publication of the proposal.

### 4.1 Detector design

Detector dimensions are shown in Figure 4.1.

#### 4.1.1 The $\bar{\nu}_e$ target acrylic vessel (12.67 m<sup>3</sup>)

The neutrino target is a 120 cm radius 280 cm height transparent acrylic cylinder, filled with 0.1 % Gd loaded liquid scintillator (see Chapter 5). Wall thicknesses (under study) range from 6 to 10 mm. The inner acrylic vessel is depicted in Figure 4.2 (left). Since the relative volume between the two inner acrylic vessels has to be controlled at a very accurate level (0.2 %), we plan to build both acrylic vessels at the manufacturer site and to move them as single units into the detector sites. This is possible for the far site, thanks to the size of the underground tunnel. The near detector site will be designed in order to allow this operation. With this strategy, no acrylic welding or gluing has to be done on site, thus reducing the uncontrolled differences between the two envelopes. Furthermore, a very precise calibration of both inner vessels is foreseen at the manufacturer (filling test). Current R&D focuses on the chemical compatibility between acrylic and liquid scintillator (see Chapter 5). Preliminary stress calculations have been done for this purpose (see Figure 4.3).

#### 4.1.2 $\gamma$ -catcher acrylic vessel (28.1 m<sup>3</sup>)

The  $\gamma$ -catcher is a 180 cm radius and 400 cm height acrylic cylinder filled with non-loaded liquid scintillator, which has the same optical properties as the  $\bar{\nu}_e$  target (light yield, attenuation length). Unlike the inner envelope, this second acrylic vessel will have to be partially assembled on site. Nevertheless, the shape and dimensions between far and near  $\gamma$ -catcher are less critical than for the inner vessels. Therefore, small differences between the near and far  $\gamma$ -catcher acrylic vessels could be tolerated (a Monte-Carlo study is being done to provide the construction tolerance).

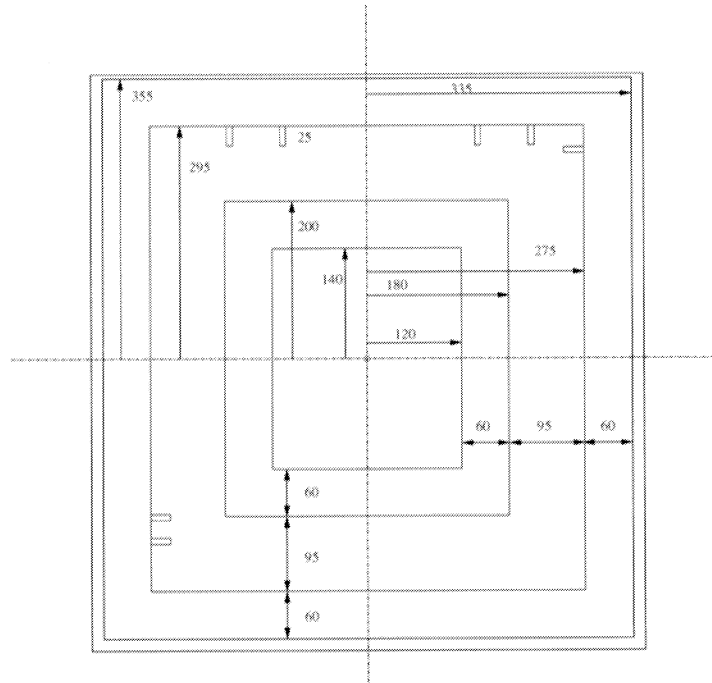


Figure 4.1: Dimensions of the CHOOZ-far detector (in cm). Starting from the center we have: the neutrino target region composed of Gd doped liquid scintillator ( $12.7 \text{ m}^3$ ), the  $\gamma$ -catcher region composed of unloaded liquid scintillator ( $28.1 \text{ m}^3$ ), the non scintillating buffer region ( $100.0 \text{ m}^3$ ), and the veto ( $110.0 \text{ m}^3$ ). The CHOOZ-near detector is identical up to and including the PMT support structure; however, its external muon veto is slightly larger to better reject the cosmic muon induced backgrounds. The exact PMT positioning has not been chosen yet.

This scintillating buffer around the target is necessary to:

**Measure the gammas from the neutron capture on Gd.**

The total released energy is 8 MeV, with a mean gamma multiplicity of 3 to 4. But there are also some 8 MeV single gammas. The buffer must be thick enough to reduce the gamma escape out of the sensitive volume, i.e. the target and the  $\gamma$ -catcher. This escape creates a tail below the 8 MeV peak. Since we must apply an energy cut to define the neutron capture on Gd, the tail of the energy spectrum has to be small enough to keep the systematic error negligible (if there is an energy scale mismatch between both detectors). Monte-Carlo simulations with a 60 cm buffer and a 100(150) keV energy error gives 0.2(0.3) % difference in the neutron counting, which is tolerable.

**Measure the positron annihilation.**

To have a clean threshold at 500 keV, it is mandatory to have very few events with an energy below 1 MeV. From the simulation, a thickness of 35 cm is adequate.

**Reject the background.**

This is the most demanding constraint. One of the most severe background in Double-CHOOZ comes from very fast neutrons, created by muons crossing rocks

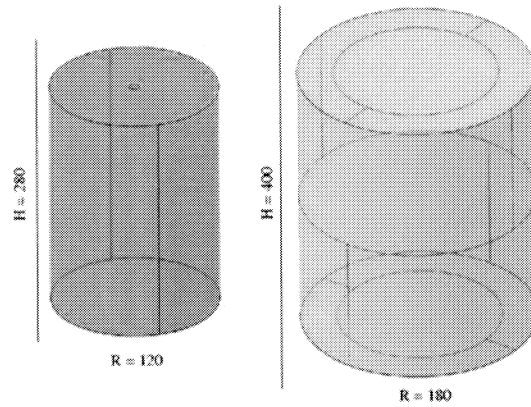


Figure 4.2: The two acrylic vessels containing the Gd doped and unloaded scintillators. The lines drawn on the cylinders show the preliminary positioning of the welding joint between the acrylic pieces. The inner envelopes will be constructed at the manufacturer and transported as single units to the detector sites while the outer envelopes will have to be assembled on sites.

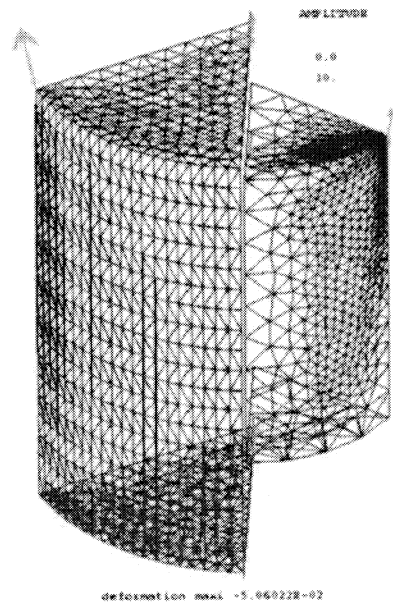


Figure 4.3: Preliminary evaluation of the stress applied on an empty acrylic cylinder suspended with three kevlar ropes (set at 120 degrees from each other). The maximum stress has been estimated at 12 MPa, while acrylic supports a maximum of  $\sim 24$  MPa in the elastic regime.

near the detector (see Chapter 7). To be able to reach the target traveling through the 2 m buffers, these neutrons must have an energy greater than 20 MeV. So when arriving at the scintillating buffer, they often deposit more than 8 MeV in the sensitive volume. This provides a useful rejection, by a factor of  $\sim 2$ . In the simulation, this rejection was seen to be stable for large buffer thickness, and to decrease when this thickness is reduced below 60 cm. Another advantage of this thickness is to allow to scale the result of the first experiment, since the sensitive volume around the target will be the same in both experiments (the veto volume was not sensitive to low energy events in the first experiment).

### 4.1.3 Non scintillating buffer (100 m<sup>3</sup>)

The non-scintillating region aims to decrease the level of the accidental backgrounds, mainly due to the contribution from the photomultiplier tubes (see Chapter 7). To define the size of this region, we have to consider the following constraints:

1. The fast neutron background implies to keep the distance from the rock to the neutrino target at least as it was for the CHOOZ experiment case<sup>1</sup>. Scaling from the CHOOZ experiment, we thus need at least 215 cm of liquid from the rock to the target.
2. The size of the target has been chosen to be 120 cm to decrease the statistical error down to 0.4 %, after three years of operation.

From those constraints, the total thickness of the veto and the non-scintillating buffer has to be smaller than 155 cm. Accounting for the size of the laboratory (mechanical constraints) and the requirement to have an efficient veto, we choose the thickness of the veto to be around 60 cm. From those considerations, the non-scintillating buffer region reduces to 95 cm. The simulation shows that this configuration fulfills our requirement on the accidental background level tolerated (which is mainly driven by PMT radioactivity).

### 4.1.4 PMTs and PMT support structure

The PMT support structure is a 275 cm radius and 590 cm height cylinder (material under study) filled with the same liquid as the  $\gamma$ -catcher, mixed with a quencher (DMP for instance).

From the simulation, 500 PMTs of 8" are necessary to achieve a photoelectron yield of  $\sim 200$  photoelectrons per MeV. Another possibility would be to use a smaller number of larger PMTs, 10", 12" or 13" for instance. The reference PMT is the photomultiplier 9354KB of ETL [ETL]. The glass used has a very low activity (60 ppm in K, 30 ppb in Th and U), and the quantum efficiency peaks at about 28 % at 430 nm. For those PMTs, the peak-to-valley ratio of the single photoelectron signal is typically 2 (1.5 guaranteed by the manufacturer). Since we expect 600 photoelectrons for a medium energy signal of 3 MeV (visible energy), there will always be an important fraction of the PMTs working in the single photoelectron regime. The electronics gain is in the  $10^6 - 10^7$  range, hence some additional amplification is required in the front-end electronics system to obtain a good single photoelectron peak definition (additional dynodes could also be a way to increase the gain). Photonis as well as Hamamatsu PMTs are under study. The final photomultiplier choice will be made in 2004, during the design phase.

<sup>1</sup>The target vessel is seen from outside of the detector under a similar solid angle in both experiments.

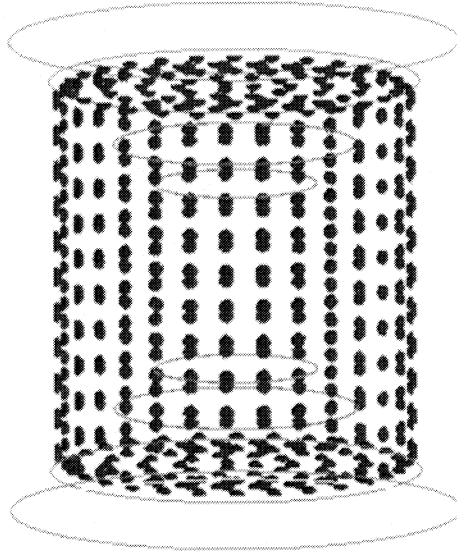


Figure 4.4: Surface of PMTs mounted on the support structure of the detector as described in the GEANT4 simulation. About 500 PMTs are displayed.

#### 4.1.5 Veto (110 m<sup>3</sup>)

The external veto is contained in a steel cylinder of 350 cm radius and 710 cm height. The veto thickness is 60 cm for the far detector. It can be enlarged for the near detector, to better reject the cosmic muon induced backgrounds, since the laboratory has to be build. This tank is shielded by 15 cm of steel in order to reduce the external backgrounds.

## 4.2 Fiducial volume

### 4.2.1 Definition of the fiducial volume

A neutrino interaction in this detector will be tagged by the neutron capture on gadolinium (as was the case in the first CHOOZ experiment [CHO03]). This is the main advantage of using a gadolinium loaded scintillator. However, there is an additional effect to consider, the *spill in/out*, that leads to a compensation between two kinds of  $\bar{\nu}_e$  interactions:

- The  $\bar{\nu}_e$  interacts in the inner acrylic target, near the vessel, but the neutron escapes the target, and is captured on hydrogen in the  $\gamma$ -catcher. In that case, there is no Gd capture to characterize the neutrino interaction, and this is thus not selected as a neutrino event.
- The  $\bar{\nu}_e$  interacts in the  $\gamma$ -catcher, not too far from the target, but the neutron enters the target and is captured on Gd. The neutrino interaction vertex is not in the target, but there is a well measured positron event followed by a Gd capture signal. This interaction is thus selected as a neutrino event.

These two kinds of events do not compensate exactly. However, the simulation shows that the difference is of the order of  $\sim 1\%$  of the total neutrino interaction rate (the software used for this simulation is a low energy neutron Monte-Carlo that was extensively used and checked for the Bugey experiments [BUG96]). This imperfect compensation is due to the presence of gadolinium in the target only. But, since this corresponding cross section is high only at epithermal neutron energies, the neutrons slow down identically in both media. The difference of behavior happens only in the last few centimeters of the neutron path, before its capture. This spill in/out effect would lead to an irreducible  $\sim 1\%$  systematic uncertainty in a new single detector experiment. However, it will cancel in the Double-CHOOZ oscillation analysis since two identical detectors will be used. Nevertheless, a second order spill in/out difference will remain in Double-CHOOZ since the neutrino direction with respect to the neutrino target boundary changes slightly between the two detectors. Indeed, this small effect comes from the correlation of the  $\bar{\nu}_e$  and the neutron directions [CHO03].

In conclusion, the method used to identify a neutrino interaction allows a very good definition of the number of target atoms. The major concern is the design, the construction and the monitoring of the inner acrylic cylinders.

#### 4.2.2 Measurement of the fiducial volume

We have to measure the volume of the inner acrylic vessels with an uncertainty below  $0.2\%$ . With standard commercial materials such as dosing pumps, it is hard to have an absolute volume determination better than  $0.5\%$ . We thus suggest to use a combination of direct and indirect measurements to obtain the required precision.

A possible solution is to use weight measurements. For this, an intermediate vessel close to the acrylic target is necessary (in the experimental hall). We plan to measure first the weight of the empty intermediate vessel, then fill the target vessel and re-measure its weight. The difference of the two measurements indicates very accurately the mass of liquid used to fill the target. Associated with a density measurement, this could provide the volume measurement with uncertainty below  $0.1\%$  (below  $10\text{ kg}$  on the mass determination, and around  $10^{-4}$  on the density measurement).

A second method under study consists to use pH measurement. This measurement has to be done with an acid/water mixture. It seems that this method can reach an  $0.2\%$  accuracy.

Independently of the volume of liquid used to fill the vessels, both detector have to be kept at the same temperature. We will thus have to monitor and control it. A simple regulation loop in the external veto is foreseen.

### 4.3 Light collection

We consider in the following a concentric cylindrical model of the Double-CHOOZ detectors consisting of the target, the  $\gamma$ -catcher and the outer buffer. The target volume of the detector is filled with organic liquid scintillator (LS) loaded with Gadolinium (Gd) consisting of a mixture of

- PXE as solvent with small amount of Gd ( $1\text{ g/l}$ ),
- PPO (2,5-diphenyloxazole) as first fluor with a concentration of  $6.0\text{ g/l}$ ,



- bis-MSB with concentration of 0.02 g/l as second fluor or wavelength shifter.

The volume of the  $\gamma$ -catcher enclosing the target is filled with the same LS but without admixture of the Gd salt. The tank containing the non scintillating buffer is covered by a reflecting material, and about 500 PMTs are installed on this surface (later called the PMT surface). Figure 4.4 displays the PMTs mounted on the support structure.

We consider the reflection coefficient ( $k$ ) as a free parameter; it can be changed within the interval from 0 (absolutely black surface) up to 0.98 (mirror reflection by VM2000 film [Mot04, 3M]). Charged particles deposit energy in the LS medium, mostly due to their interaction with the solvent molecules. PXE excited molecules transfer their energy to the PPO molecules via non-radiative processes. Then, an energy transfer occurs between the PPO and the bis-MSB, mainly by radiative transitions (100 % probability). Therefore the primary (observed) fluorescence of LS is connected with the radiative decay of the bis-MSB excited molecules. The energy spectrum of the photons emitted by the shifter is shown in Figure 4.5. The

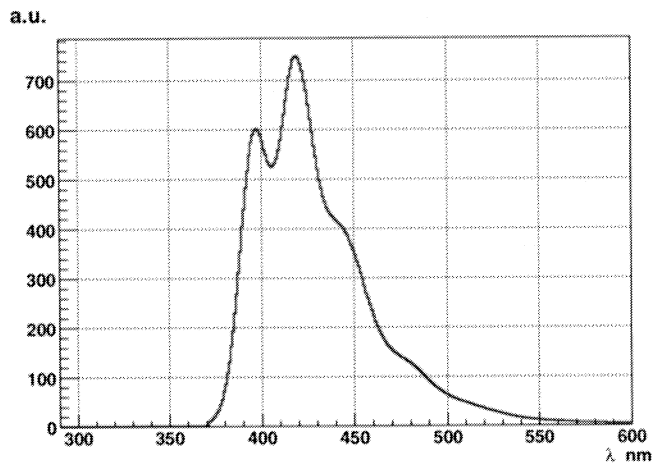


Figure 4.5: Emission spectrum of the bis-MSB wavelength shifter.

radiative transport from the light emission vertex to the PMTs is described by a GEANT4 Monte-Carlo simulation. Borexino-like PMTs cover between 12.5 % to 17.5 % of the surface of the supporting cylinder. The quantum efficiency of the photocathode is shown on Figure 4.6. The Monte-Carlo simulation developed for this work is based on the light propagation model described in [LP00] and [Birks], and has been used for the Borexino experiment. The time decay of the emitted bis-MSB photons is described phenomenologically by the sum of few exponentials having time constants  $\sim 5$  ns. The light yield of the LS is taken to be 8,000 photons per  $\text{MeV}^2$ , both for the target and for the  $\gamma$ -catcher of the detector. The photons emitted by the bis-MSB propagate through the target volume, and interact with PXE, PPO, bis-MSB and Gd salt molecules. Two physical processes have been taken into account:

- (Rayleigh) elastic scattering,
- absorption.

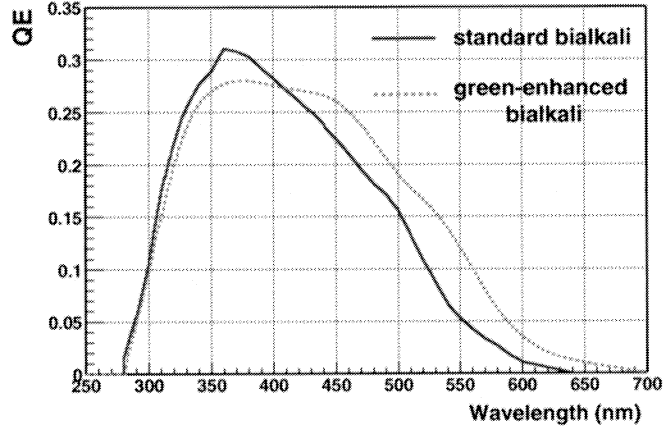


Figure 4.6: Quantum efficiency of the PMT photocathode.

The light attenuation was described by an exponential function with the extinction coefficient  $\mu(\lambda) = \mu_a(\lambda) + \mu_s(\lambda)$ , where  $\mu_a(\lambda)$  is the absorption coefficient,  $\mu_s(\lambda)$  the scattering coefficient and  $\lambda$  the wavelength of the light. The mean free path of the photon is equal to  $\Lambda(\lambda) = 1/(\log(m \times \mu(\lambda)))$ , where  $m$  is the molar concentration of the relevant scintillation component. The cross sections for these interactions have been extracted from the experimental data, obtained by usual spectroscopy methods. An example of  $\Lambda(\lambda)$  variation for bis-MSB is presented in Figure 4.7. Two

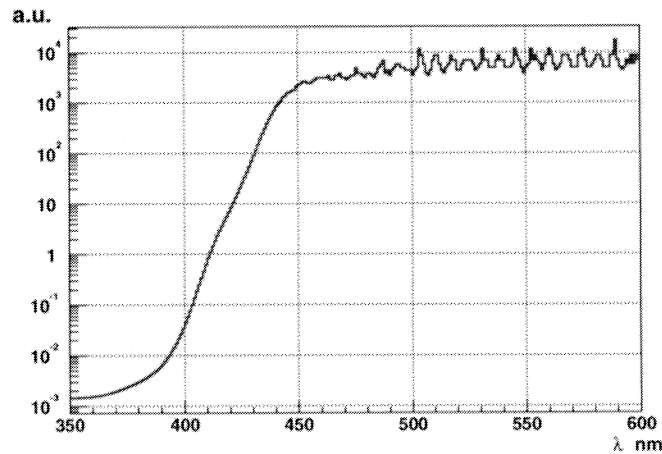


Figure 4.7: Absorption spectrum of the bis-MSB wavelength shifter.

different behaviors can be seen. At wavelengths longer than 450 nm the absorbance drops rapidly and the measured extinction coefficients are practically equal to the coefficient for Rayleigh scattering, while at wavelengths shorter than 450 nm photons absorption is the main interaction process. Elastically scattered photons have

<sup>2</sup>This is 2/3 of the standard unloaded pure PC scintillator.

an angular distribution described as  $1 + \cos^2 \theta$ , independent of the wavelength. The process of light absorption can be accompanied by an isotropic re-emission of the photons. The spectrum of re-emitted photons and time of the re-emission process were taken equal to the fluor primary spectrum and light time decay (1.3 nsec for bis-MSB). The re-emission probability was assumed to be equal to the absorbing molecule quantum efficiency taken around 0.36 for PXE, 0.8 for PPO and 0.96 for bis-MSB. This absorption/re-emission process can occur several times until either the photon is absorbed in the scintillator volume (its energy disappears due to the non-radiative processes) or its wavelength falls in a region where the absorption probability is negligible. Photon reflection (or absorption) near the wall of the buffer is described by the reflection coefficient. As a result of the transport process, a part of the photons reaches photocathode surface of the PMTs. The spectrum of these photons is shown in Figure 4.8. It can be seen that the left part of the spectrum decreases more rapidly with respect to the emitted spectrum of bis-MSB; this is connected with the self-absorption of bis-MSB molecules. The results of the

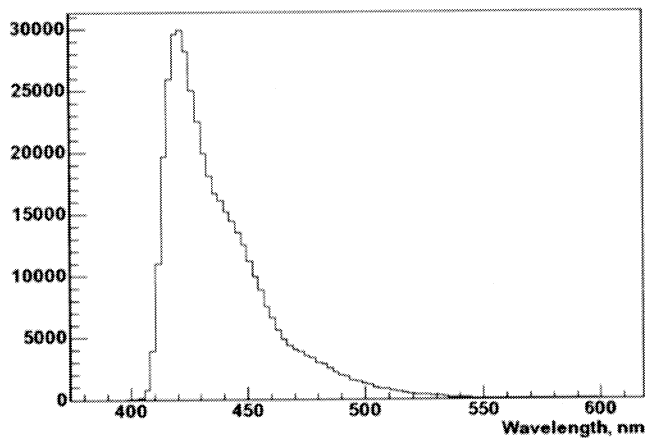


Figure 4.8: Spectrum of the photons as they arrive at the PMT surface.

simulation are presented as a number of photoelectrons per MeV of energy deposit, from point like events generated inside the target and the  $\gamma$ -catcher to PMT-visible photons that propagate to the photocathode of PMTs. If the buffer wall is black (reflection coefficient  $k=0$ ) the number of photoelectrons was found to be around 300 for events in the target center (for a 17.5 % coverage). This number increases up to 40 % if the buffer wall is reflective. The light collection time distribution is shown in Figure 4.9. Obviously, the reflected light increases the tail of the time distribution. During the first 30 ns, all photoelectrons arise from the photons that directly reach the PMT surface. The simulation shows a very good light collection homogeneity. The dependence of light collection from the event position inside the target was found to be within 5 % and increased up to 10 % at the position near the walls of the  $\gamma$ -catcher. The collection of the reflected light improves the homogeneity and for a reflection coefficient of 0.8, the light collection is very homogeneous (+2-3 % at the target border, +5 % at the scintillating buffer border).

Detector design, the number of PMTs and their positioning is now being optimized based on the Monte-Carlo simulation presented here.

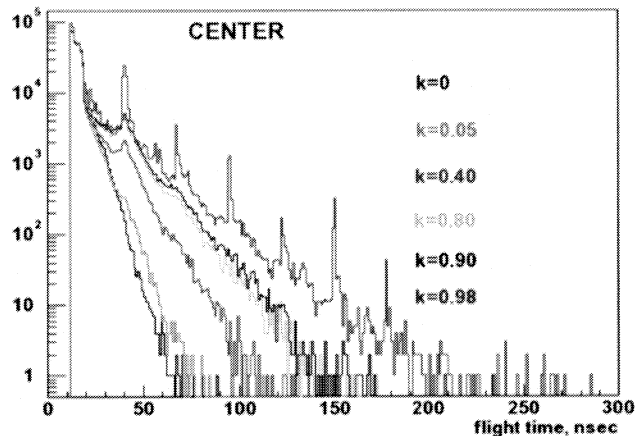


Figure 4.9: Light collection for different reflectivity coefficients of the PMT support structure ranging from  $k=0$  (black paint) to  $k=0.98$  (VM2000 foil [Mot04, 3M]).

## 4.4 Electronics

### 4.4.1 Data recording

The following data have to be recorded:

- Charge and time for each PMT.
- Pulse shape for PMT clusters, to identify recoil protons due to fast neutrons.

Neutrino events are made of two light pulses, separated by a delay of a few  $\mu\text{s}$  to 200  $\mu\text{s}$ . The single trigger rate, although lower than 10 Hz can still be reduced using the delayed coincidence, as explained below. This imply to store the data of the two pulses before the trigger decision. Furthermore, for calibration with Cf sources, several neutrons are detected after the fission signal, with an average multiplicity of 4, extending beyond 8. The dead time of the system must be kept low, stable and simple to control, since it contributes to systematic error.

The front-end electronics will have to:

- Separate the signal from the high voltage, if positive.
- Amplify the signal by a factor  $\sim 50$  to use the single photoelectron range (PMTs stability monitoring).
- Add the analog signals (the total sum over the detector PMTs will be used in the trigger).
- Include a discriminator per PMT (to monitor the trigger stability).

The minimal solution for digitization is to use multihit charge ADCs, shapers and multihit TDCs for all channels, completed by Flash-ADCs for a few tens of PMT groups. The alternative would be to use Flash-ADCs for all channels, build PMT clusters and emulate ADCs and TDCs. A new a model of Waveform recorder with a smart memory management is being developed for Double-CHOOZ. It will provide a multihit capability and digitization with zero dead time. This is an upgrade of an existing model used for Borexino (the prototype will be ready in 2004).

### 4.4.2 Trigger logic

The plan is to keep the trigger logic as simple as possible. It will be based on a rough energy measurement made by the analog sum of all PMT signals. A first level (single pulse) trigger will feature two channels:

1. The “particle” channel: a pulse of 0.5-50 MeV, which will cause the recording of all channels.
2. The “muon” channel: a pulse above 50 MeV *or* a signal in the veto which will cause the recording of time and energy information in a digital LIFO.

The data are read out for all first level triggers and a second level trigger (final) is made online with the coincidence of two “particle” triggers, within 200  $\mu$ s. A final event is composed of two singles, including information about the last muons. The data for each “particle” will be composed of

- the charge and time for all PMTs,
- the pulse shapes for  $\sim 16$  PMT groups (multiplicity tunable by software).

In addition, during data taking, some artificial light pulse patterns will be generated inside the target, using laser or LEDs. These artificial events will mimic the physical  $\bar{\nu}_e$ , in order to monitor the trigger system efficiency. Of course, each event triggered will carry a specific tag and serial number, for its identification in the offline data analysis. Table 4.1 summarizes the expected rates for neutrino like triggers. The

Neutrinos	0.04 Hz
Artificial	0.05 Hz
Multineutron after a muon	0.3 Hz
Cosmogenic	0.001 Hz
Fast neutrons	0.001 Hz
Accidental coincidence	0.001 Hz

Table 4.1: Summary the expected trigger rates for neutrino like events at CHOOZ-near. Trigger rates at CHOOZ-far will be smaller.

resulting data flow at CHOOZ-near will be around 20 kB/event, dominated by pulse shape data. With a trigger rate lower than 1 Hz, the amount of data remains below 2 GB/day.



## Chapter 5

# Liquid scintillators and buffer liquids

### 5.1 Liquid inventory

The Double-CHOOZ detector design requires different liquids in the separate detector volumes as shown in Figures 3.4 and 3.5. The inner most volume of  $12.7 \text{ m}^3$ , the  $\bar{\nu}_e$ -target, contains a proton rich liquid scintillator mixture loaded with gadolinium (Gd-LS) at a concentration of approximately 1 g/liter. The adjacent volume, the  $\gamma$ -catcher, has a volume of  $28 \text{ m}^3$  and is filled with an unloaded liquid scintillator. The photomultipliers are immersed in a non-scintillating buffer in order to shield the active volume from the gamma rays emitted by them. The volume of the buffer liquid is approximately  $100 \text{ m}^3$ . Last, an instrumented volume of approximately  $110 \text{ m}^3$  encloses the whole setup serving as a shield against external radiation and as a muon veto system. Table 5.1 summarizes the liquid inventory of a single detector system. The selection of the organic liquids are guided by physical and technical

Labeling	Volume [ $\text{m}^3$ ]	Type
$\bar{\nu}_e$ -target	12.7	Gd loaded LS (0.1 %)
$\gamma$ -catcher	28.1	unloaded LS
Buffer	100	non-scintillating organic liquid
Veto	110	low-scintillating organic liquid

Table 5.1: Overview of liquid inventory for a single detector. Alternatively we consider as well the use of a water Cherenkov detector for the veto.

requirements, as well as by safety considerations. In particular, the solvent mixtures or their components have a high flash point (e.g. phenyl-xylylethane (PXE): flash point (fp)  $145 \text{ }^\circ\text{C}$ , dodecane: fp  $74 \text{ }^\circ\text{C}$ , mineral oil: fp  $110 \text{ }^\circ\text{C}$ ). The  $\bar{\nu}_e$ -target and  $\gamma$ -catcher have as solvent a mixture of 80 % dodecane and 20 % PXE, or alternatively trimethyl-benzene (PC). Mineral oil is under study as an alternative to dodecane. A similar solvent mixture matching the density of the  $\gamma$ -catcher and  $\bar{\nu}_e$ -target, will be used as the buffer liquid, however with the addition of a scintillation light quencher (e.g. DMP). Alternatively, pure water is under investigation provided the buoyancy forces can be contained, or a density matched water-alcohol mixture. The veto volume contains low-scintillating organic liquid and will be equipped with PMTs. Alternatively, we also consider to fill the veto with water and to operate it as a water Cherenkov detector.

## 5.2 Status of available scintillators

Metal loading of liquid scintillators have been comprehensively studied in the framework of the LENS (Low Energy Solar Neutrino Spectroscopy) R&D phase [LEN99]. The key groups involved in this research, MPIK and LNGS/INR, are contributing their expertise to the Double-CHOOZ project. The challenge of the LENS project was to produce stable liquid scintillators loaded with ytterbium as well as indium at 5-10 % in weight while simultaneously achieving attenuation lengths of several meters and high light yields. Novel scintillator formulations [MPI03b, MPI04a, Cat04a, Cat04b] have been developed successfully. The scintillators have surpassed longterm tests on the scale of up to several years. Several prototype detectors filled with different scintillator samples are continuously measured in the LENS low-background facility at Gran Sasso since October 2003 to study the stability of the scintillator as well as backgrounds. No change in light yield nor in attenuation length has been observed and backgrounds are extremely low.

Research with gadolinium loaded scintillator at MPIK and LNGS/INR indicates that suitable gadolinium loaded scintillators can be produced using the chemistry of beta-diketone complexes as well as using a single carboxylic acid stabilized by careful control of pH. Furthermore, research is being carried out to achieve stability with respect to interaction with detector container materials, through the adjustment of inert solvent components of the scintillator while simultaneously retaining high scintillation yields.

### Beta-diketonate (BDK) Gd-LS:

The studies of the synthesis and properties of beta-diketonates of rare earths and their relevant chemistry, especially stability at high temperatures, is illustrated in [Har92, Har85]. First results of Gd-betadiketonate loaded liquid scintillators have been reported in [MPI03a]. Figure 5.2 displays the scintillation yield of the unloaded PXE [BOR04] based scintillator as a function of dodecane concentration. A scintillation yield of 78 % with respect to pure PXE is observed at a volume fraction of 80 % dodecane. Figure 5.1 shows the light yield of a scintillator system with a solvent mixture of 80 % dodecane and 20 % PXE with varying PPO fluor concentration. The observed light yield corresponds to 80 % of the unloaded scintillator mixture, or to 60 % of a pure PC based scintillator. Attenuation length of the Gd-betadiketonate is being studied and values greater than 10 m at 430 nm have been observed after optimizing the synthesis steps. Figure 5.3 compares the spectral attenuation length of commercial 0.1 % Gd-acetylacetonate (Gd-acac) with that synthesized by us. A secondary fluor(bis-MSB, emission spectrum peaked between 420 to 450 nm) at 20-50 mg/l is used to match the emission to the absorption spectrum (wavelength shifter)

### Carboxylate (CBX) Gd-LS:

The chemical preparation of Gd loaded carboxylic acid based scintillators (single acid, pH controlled) has been established and demonstrated to be sound in our laboratories. These results have been submitted for publication, are in preparation for submission and are presented in publications [Cat04a, Cat04b, Dan03, MPI04b, MPI03c]. Progress has been swift towards the definition of scintillator specifics and quantitative performance. The main aspects are summarized below.

A variety of Gd carboxylate scintillators have been produced, using methylvaleric ( $C_6$ ), ethyl-hexanoic ( $C_8$ ) as well as trimethyl-hexanoic ( $C_9$ ) acids. The possible solvents are trimethyl-benzene (PC) or PXE, mixed with either dodecane or mineral oil. The Gd scintillator can be synthesized by adding a crystalline material or by direct extraction into the liquid. Proper control of pH during the synthesis is important.



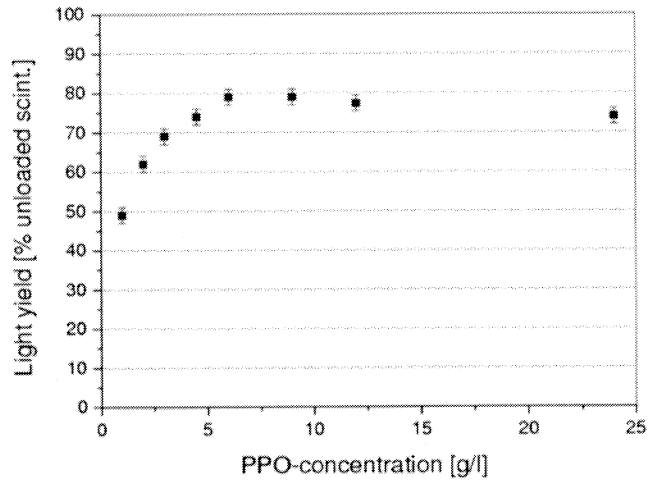


Figure 5.1: Scintillation light yield of 80 % dodecane 20 % PXE 0.1 % Gd beta-diketonate LS with varying PPO concentration relative to the unloaded 80 % dodecane 20 % PXE mixtures with PPO at 6 g/l.

The solubility of two candidate Gd-carboxylate compounds namely Gd-2MeVA and Gd-EtHex, have been measured in a 65 % PC and 35 % Dodecane solvent mixture and found to be respectively 16.0 and 3.2 g/l. Light yields of 60 % with respect to pure PC and attenuation length of 15 m have been achieved with Gd concentrations of 4 g/l and BPO (the primary fluor) concentration of 4 g/l in the same solvent mixture. A C<sub>9</sub> CBX version in 50 % PC and 50 % dodecane and 1 g/l Gd gave 87 % of light with respect to the unloaded mixture. Good optical properties have been achieved.

The first stability tests at elevated temperatures have been carried out successfully with the carboxylate systems. Sample mixtures of PC, mineral oil and Gd salt were heated to 40 °C during 18 days and mixtures with dodecane instead of mineral oil to 50 °C during 7 days. Figure 5.4 shows the absorption spectra of the PC/dodecane based Gd-carboxylate LS before and after the temperature test. Both the light yield and the attenuation length are stable under the test conditions.

### 5.3 Scintillator definition phase

Both the beta-diketonate and the carboxylate based Gd-LS show excellent performances and are viable candidate liquid scintillators for the  $\bar{\nu}_e$ -target. The research on these LS shifts now from the R&D phase to the definition phase and to qualification test of their use in Double-CHOOZ. Both Gd-LS types have to undergo long term tests to verify no changes in the optical performance in contact with detector materials. Backgrounds from radioactive trace contaminations will be studied in the Lens Low Background Facility (LLBF) at Gran Sasso [Mot04]. Work specific to the different scintillator formulation are listed below.

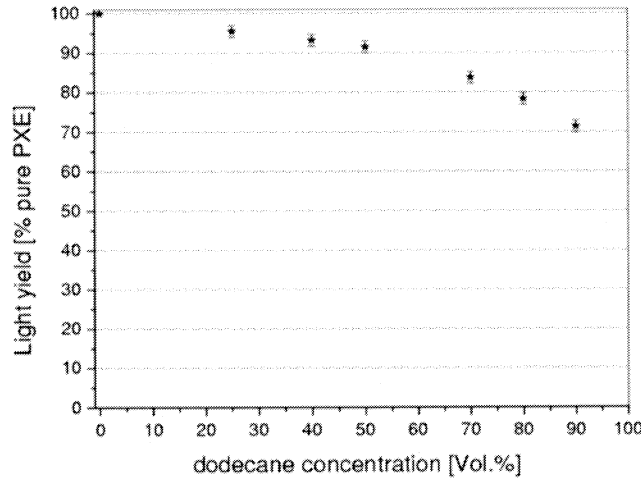


Figure 5.2: Scintillation light yield of PXE/dodecane mixture with varying dodecane concentration. The PPO concentration is kept constant at 6 g/l.

#### **BDK Gd-LS:**

The nominal BDK Gd-LS candidate is based on a mixture of PXE (20 %), dodecane (80 %), PPO (6 g/l) and bis-MSB (50 mg/l) with a Gd loading of 0.1 % by weight. Future laboratory work will concentrate on further optimization of the chemical synthesis with special focus on questions related to the solubility and purity of Gd-acac. The solubility has an impact on the engineering of the Gd-LS production scheme. Moreover, the optimization of energy transfer properties will be studied. A further increase in light yield by fluor optimization appears possible. Mineral oil (MO) will be studied in more detail as an alternative to dodecane since the density range of MO provides the possibility to adjust buoyancy forces applied to the scintillator containment vessel. A PXE (20 %) / MO (80 %) based scintillator can be designed matching a density in the range from 0.8 to 0.9 g/l compared to 0.80 g/l for the PXE (20 %) / dodecane (80 %) mixture.

#### **CBX Gd-LS:**

Work on the CBX Gd-LS formulation will concentrate on the selection of the carboxylic acid to use in the synthesis and on determining the chemical parameters relevant for the chemical stability of the solution. Possible surface induced chemical reactions will be investigated. Optimization of light yield and attenuation length are being further pursued by optimizing the synthesis as well as the solvent and fluor composition. The same delineations concerning solvents and densities described previously also apply here.

From the results of the laboratory research, we now have two working Gd-LS formulations and we expect that both the BDK and CBX systems will comply with the design goals of Double-CHOOZ. The designation of the default and backup LS formulation will be one of the milestones during the definition phase. A further outcome of this phase is the detail engineering of the Gd-LS production scheme. This will be a critical input for the finalization of the scintillator fluid systems

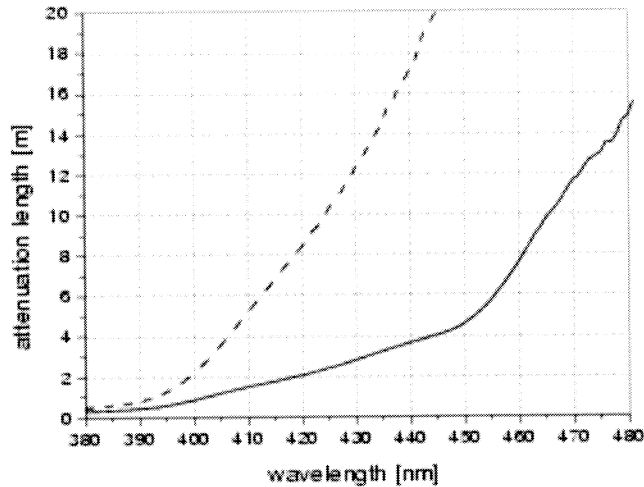


Figure 5.3: Spectral attenuation length of Gd-acac from an optimized synthesis compared with a commercial purchased product. Attenuation length of approximately 12 m is achieved at wavelength of 430 nm, corresponding to the emission peak of the secondary shifter.

discussed in the next section. The final selection of the buffer and veto liquids will be done contingent upon the mechanical design of the containment vessels and the definition of the Gd-LS formulation.

## 5.4 Scintillator fluid systems

The scintillator fluid systems (SFSs) include the **off-site SFS** for production, purification and storage of the Gd-LS, as well as the  $\gamma$ -catcher LS. A possible location for the off-site SFS is MPIK. The **on-site SFS** will be on the reactor area, close to the experimental location.

The SFSs scheme envisions the production and storage of the complete Gd-LS for both the near and far detector, in order to assure identical *proton per volume* concentrations. The off-site SFS will include ISO-containers for storage and subsequent transport to the experimental site. Moreover, it will include a purification column, a nitrogen purging unit, a mixing chamber, nitrogen blankets and auxiliary systems. A similar system, known as Module-0 [Har99], has been constructed by groups in this LOI associated with Borexino. Since the specifications for Module-0 are more demanding than required for Double-CHOOZ, no problems are anticipated.

The on-site SFSs will consist of an area above ground close to the detector sites for the transport tanks which will be connected to the detector by a tubing system. The purpose of the on-site SFS is to transfer the different liquids from their transport container into the detector volumes in a safe and clean way. The different detector volumes will be filled simultaneously and kept at equal hydrostatic pressures to guarantee the integrity of the detector vessels; this will require several parallel lines. Details of the SFSs will be worked out during the definition phase.

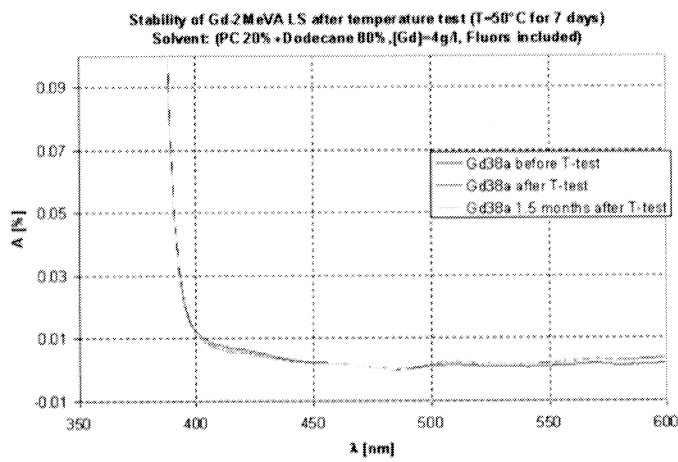


Figure 5.4: Absorption spectra of carboxylate Gd LS prior and after temperature test. The sample was kept at 50 °C for 7 days. The scintillator composition consists of PC (20 %), dodecane (80 %), [Gd]=4 g/l and fluors.

## Chapter 6

# Calibration

The main goal of the calibration effort is to reach maximum sensitivity to neutrino oscillations by comparing the positron energy spectra measured by the CHOOZ-far and CHOOZ-near detectors. This is necessary for reaching the desired sensitivity to neutrino oscillations in Double-CHOOZ. Calculations show that a relative difference both in geometry (construction) and in response of detectors slightly distorts the ratio of the spectra in both detectors. Therefore, appropriate corrections and errors obtained on the basis of absolute and relative calibration measurements should be administered to the data. This should be the result of detailed Monte-Carlo simulations (see Chapter 4) backed up by an extensive program of source calibrations. The calibration sources (See Table 6.1) must be deployed regularly throughout the detector active volume to simulate and monitor the detector response to positrons, neutron captures, gammas and the backgrounds in the Double-CHOOZ experiment. This requires a dedicated mechanical system in order to introduce calibration sources into the different regions of the detector. There are a number

Technique	Calibrations
Optical Fibers, Diffusive Laser ball	Timing and Charge Slopes and Pedestals, attenuation length of detector components
Neutron Sources: Am-Be, $^{252}\text{Cf}$	Neutron response, relative and absolute efficiency, capture time
Positron Sources: $^{22}\text{Na}$ , $^{68}\text{Ge}$	$e^+$ response, energy scale, trigger thresh.
Gamma Sources:	Energy linearity, stability, resolution, spatial and temporal variations.
$^{137}\text{Cs}$	$\beta^-$ , 0.662 MeV
$^{22}\text{Na}$	$\beta^+$ , 1.275 MeV + annih
$^{54}\text{Mn}$	EC, 0.835 MeV
$^{65}\text{Zn}$	1.35 MeV
$^{60}\text{Co}$	EC, 1.173, 1.33 MeV
$^{68}\text{Ge}$	EC, $\beta^+$ 1.899 MeV + annih
$^{88}\text{Y}$	EC, 0.898, 1.836 MeV
H neutron capture	2.223 MeV
$^{241}\text{Am}$ - $^9\text{Be}$	( $\alpha$ ,n) 4.44 MeV ( $^{12}\text{C}$ )
Gd neutron capture	Spectrum in 8 MeV window
$^{228}\text{Th}$	2.615 MeV
$^{40}\text{K}$	EC, $\beta^+$ , $\beta^-$ , 11 % 1.46 MeV

Table 6.1: Table showing the different techniques that are available to calibrate the Double-CHOOZ experiment.

of specific tasks for a successful calibration of the detectors. These include optical calibrations (single photoelectron (PE) response, multiple PE response, detector component optical constants), electronic calibrations (trigger threshold, timing and charge slopes and pedestals, dead time), energy (energy scale and resolution), and neutron and positron detection efficiency and response. In addition, detector calibrations must test the Monte-Carlo and analysis code to verify the accuracy of the simulations, throughout the detector (spatially), and during the lifetime of the experiment.

## 6.1 Optical and electronic calibrations

The optical calibrations are based on the experience with CHOOZ and the CTF-Borexino experiments. In CTF-Borexino the optical calibration consists of a UV pulsed-laser (jitter less than 1 ns) coupled to an optical fiber illuminating separately each PMT. This allows the single PE response to be measured since the amplitude of the pulse is tuned to approximately a single PE. This technique allows the gain, timing slope, charge slope and pedestals to be determined relative to individual PMTs and to the triggers. In addition to the optical fiber calibration, the light attenuation in the liquid scintillator is monitored using a diffusive laser ball source, as has been successfully used by the SNO experiment [SNO02]. This source illuminates all the PMTs isotropically and allows the attenuation length of the detector components and the PMT angular response to be measured as a function of photon wavelength. Finally, to ensure that we are able to veto muons with high efficiency, we must also calibrate the PMTs mounted on the stainless steel tank. This is done by also connecting optical fibers to these PMTs. The attenuation length of the water (or oil) shielding is measured by deploying the laser ball in this region.

## 6.2 Energy calibration

The specific signature for the detection of an electron antineutrino through inverse beta decay is the detection of prompt gammas from the annihilation of the positron and the delayed capture of a neutron several tens of  $\mu\text{s}$  later. While direct calibration with an antineutrino source is impossible, it is possible to simulate each of the components of the antineutrino signal, such as the prompt positron and delayed neutron by deploying positron, neutron, and gamma sources.

The standard calibration system will include a permanent vertical tube, entering the detector until the center of the inner acrylic target. This open tube will allow frequent and safe calibration with radioactive sources.

### 6.2.1 Gamma ray sources

Positron annihilates at rest and produces 2 back-to-back gammas. Thus, for a high detection efficiency we must be able to calibrate the detector energy response to gammas from 1 MeV to  $\sim 10$  MeV corresponding to the endpoint of the fission product beta decays. In addition, a neutron is detected by its capture on the Gd additive to the liquid scintillator and produces a gamma cascade of approximately 8 MeV. For this reason, it is necessary to also know the energy scale in the high energy window of 6-10 MeV to be able to identify the delayed second trigger as a neutron. Specifically, it will be necessary to know the gamma energy corresponding to the neutron detection threshold for both the near and far detector with a 100 keV accuracy. This is accomplished by deploying various higher energy gamma

calibration sources (see Table 6.1) and by detailed Monte-Carlo simulations in the energy region where there are no calibration sources.

The overall energy scale can be determined from the position of the 0.662 MeV peak of the  $^{137}\text{Cs}$  source, and then verified by calibration with several gamma sources (see Table 6.1) in different energy ranges:  $^{54}\text{Mn}$  (0.835 MeV),  $^{22}\text{Na}$  (1.275 MeV),  $^{65}\text{Zn}$  (1.351 MeV),  $^{60}\text{Co}$ , and  $^{228}\text{Th}$  (2.614 MeV). These gammas allow the energy response to the positron annihilation photons to be determined for different positron energies. The capture of neutrons from an Am-Be source scintillator (to be discussed later) can also be used as a high energy gamma source as it produces prompt 4.4 MeV gammas. We will also use the natural sources from radioactive impurities of the detector materials ( $^{40}\text{K}$ ,  $^{208}\text{Tl}$ ) and neutrons produced by cosmic muons for energy calibration. Since these sources are present permanently, they are useful for monitoring the stability of the energy response. Thus, the primary purpose of the gamma sources are to determine and monitor the energy scale for both the far and near detectors as a function of position and time during which the experiment is conducted.

### 6.2.2 Positron response

Positron detection can be simulated experimentally by means of the  $^{22}\text{Na}$  source. A  $^{22}\text{Na}$  source emits a 1.275 MeV primary gamma accompanied by a low energy positron which annihilates inside the source container. The primary and annihilation gammas from the source mimic the positron annihilation resulting from an antineutrino event inside the detector. An alternative positron source is a  $^{68}\text{Ge}$  source which produces positrons with higher energies, and therefore calibrates higher energy positrons.  $^{68}\text{Ge}$  decays by EC to  $^{68}\text{Ga}$  and  $\beta^+$ -decays to stable  $^{68}\text{Zn}$  with an endpoint of 1.9 MeV. This isotope also has the advantage that it produces only low energy gammas in coincidence with the nuclear decay, and the  $\beta^+$  has an endpoint of 1.889 MeV 89 % of the time. A second purpose of this source (if a source is constructed so that the beta is absorbed by the shielding surrounding the source) is to tune the trigger threshold to be sensitive to annihilation gammas and to monitor its stability. A  $^{68}\text{Ge}$  source has been successfully used in the Palo Verde reactor neutrino experiment [PV97].

### 6.2.3 Neutron response

Coincident with the production of a positron in inverse beta decay, a neutron is produced. The neutron then quickly thermalizes and is captured on the Gd ( $^{155}\text{Gd}$  or  $^{157}\text{Gd}$ , with cross sections of 60,900 and 254,000 barns, respectively) loaded in the central target. The neutron capture is accompanied by the emission of a cascade of gamma-rays with the summed energies of 8.536 and 7.937 MeV, respectively. Thus, neutrons are selected by cutting on gammas with energies exceeding 6 MeV. However, a fraction of the gamma-rays can escape detection, especially events that occur near the boundary of the fiducial volume. Therefore, it is expected that the neutron detection efficiency decreases for events near the borders of the acrylic vessel that contains the Gd loaded liquid scintillator. Calibration of this effect must be quantified by deployment of neutron calibration sources throughout the detector and comparing the detector response to Monte-Carlo. In addition to measuring the neutron response, neutron calibration is also a very sensitive method for determining in-situ various liquid scintillator properties, such as the hydrogen and gadolinium concentration in the liquid scintillator.

There are two suitable and accessible neutron sources for neutron calibration: the Am-Be source and  $^{252}\text{Cf}$  spontaneous fission source. These sources emit neutrons with different energy spectra from what is expected from inverse beta decay,

and thus the importance of these differences needs to be quantified. To decrease the background during neutron source deployment, neutrons from Am-Be should be tagged by the 4.4 MeV gamma emitted in coincidence with the neutron. This allows the neutron capture detection efficiency to be determined independent of knowing the precise rate of the neutron source, because every time a 4.44 MeV gamma is detected a neutron is released [Cro89]. The absolute neutron detection efficiency can also be determined with a  $^{252}\text{Cf}$  source by using the known neutron multiplicity (known to 0.3 %). For the source placed into the center, the size of the Gd region is larger than the neutron capture mean free path, so that the neutron capture is studied independent of the presence of the acrylic vessel. In order to tag the neutron events, a small fission chamber is used to detect the fission products. Therefore, neutron source calibrations provide us with the relevant data to calibrate the detector response to neutrons. In particular, neutron sources allow us to measure the absolute neutron efficiency, to determine and monitor the appropriate thresholds of neutron detection, and to measure the neutron capture time for both the far and near detectors.

#### 6.2.4 The Calibration source deployment system

A mechanical system must be developed to introduce calibration sources throughout the detector active volume. The system must be easy to set up so that calibration can be done frequently without loss of neutrino live time. The suggestion is to use a system of ropes and pulleys similar to the SNO experiment (see Figure 6.1 for a conceptual design). However, unlike the SNO experiment we must be able to deploy sources throughout the active volume, rather than in a plane as is done in the SNO experiment. The reason for this is that because during the lifetime of the detector, PMT mortality might result in an anisotropy in the detector response. Moreover, the effect will manifest as an anisotropy relative to Chooz-Near and Chooz-Far which will impact on the energy resolution and scale of the two detectors. The system of ropes and pulleys must be designed so that the calibration sources sample a large fraction of the active volume and can calibrate this effect.

#### 6.2.5 Map of the Gd-LS target

The starting point of the design is to introduce sources through a glove box situated at the center and top of the cylinder housing the Gd-LS target. In the glove box sources can be prepared for deployment without introducing contaminants into the active volume. The glove box can also be evacuated and flushed with  $\text{LN}_2$  before deploying sources to prevent Radon from entering the active volume. The sources are then suspended from a rope and lowered straight down from the glove box to the bottom of the cylinder using a stepper motor. In this way we can calibrate the variation of the detector response along the axis of symmetry of the cylinder (z-axis). To calibrate the detector response off of the z-axis the calibration sources must be physically moved away from the z-axis such that the detector response as a function of radius can be determined. To achieve this, the idea is to fasten two ropes on opposite sides of the cylinder. Then, to feed the rope through two pulleys (one for each side rope) attached to top of the calibration sources, then to a stepper motor located near the glove box. The tension on either of the ropes can then be independently adjusted by carefully controlling stepper motors. When the tension is changed of one of the side ropes the source will move away from the z-axis. This will allow the sources to be deployed throughout most of the area of a plane defined by the central axis of symmetry (z-axis) and the line connecting the places that the ropes are attached. Including a second set of ropes perpendicular to the first will allow the source to be moved not only away from the z-axis but throughout most



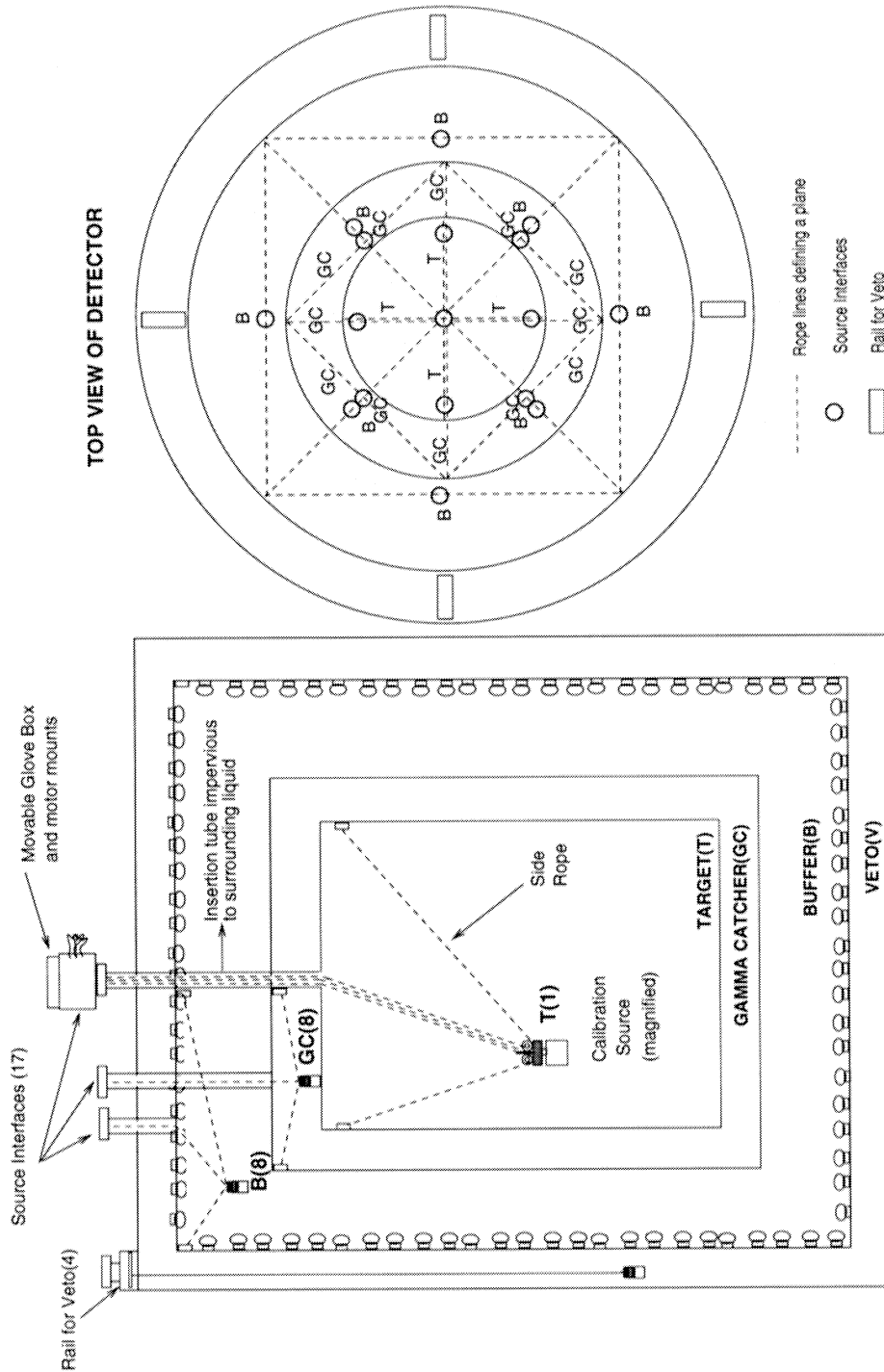


Figure 6.1: A possible scenario for a calibration source deployment system adapted from the SNO experiment calibration system.

of the active volume of the target. The SNO experiment has been able to attain a deployment accuracy of 5 cm using this method when the source is moved in a plane [NIM01].

### 6.2.6 Calibrating the gamma-catcher, buffer, and veto

A deployment mechanism must also be devised to deploy sources outside of the main central target. Sources must be deployed in the gamma catcher region as well as the buffer and the veto. A further requirement of the components inside the active volume is that the system must not block the scintillation light, nor change the detector response, and they must be impervious to liquids. The suggestion is again to use a system of pulleys and side ropes to cover most of the volume. A possible scenario for such a system is shown in Figure 6.1. The system would sample calibration source positions in a plane from the z-axis outward through the cylinders to the veto cylinder. The sources will be accessed through a glove box which will be movable so that it can be mounted on top of all the source interfaces. The calibration of the veto can be done with a rail deployment system (only 1 central rope but movable along the radius of the cylinder), since here the mechanism can be constructed without blocking the scintillation light. The right panel of Figure 6.1 shows a possible configuration of the ropes, specifically the figure shows how the top (ropes outward from the center) and sides (ropes in shape of squares) of the detector will be calibrated. However, calibration of the bottom of both detectors is more difficult since access to this region is limited. Calibration of the bottom portion of the detectors still needs to be investigated.

# Chapter 7

## Backgrounds

The signature for a neutrino event is a prompt signal with a minimal energy of about 1 MeV and a delayed 8 MeV signal after neutron capture in gadolinium. This may be mimicked by background events which can be divided into two classes: accidental and correlated events. The former are realized when a neutron like event by chance falls into the time window (typically few 100  $\mu$ s) after an event in the scintillator with an energy of more than one MeV. The latter is formed by neutrons which slow down by scattering in the scintillator, deposit  $> 1$  MeV visible energy and are captured in the Gd region. In this chapter we first discuss possible sources and fluxes for background events and later estimate their rates. With these numbers we find criteria for the necessary overburden of the near detector and we will extract purity limits for detector components.

### 7.1 Beta and gamma background

#### 7.1.1 Intrinsic beta and gamma background

In this section the intrinsic background due to beta and gamma events above  $\sim 1$  MeV is discussed. It can be produced in the scintillator or in the acrylic vessels which contain the liquid. The contribution from the Uranium and Thorium chains is reduced to a few elements, as all alpha events show quenching with visible energies well below 1 MeV. Furthermore the short delayed Bi-Po coincidences in both chains can be detected event by event, and hence rejected. In the end, only the decays of  $^{234}\text{Pa}$  (beta decay,  $Q = 2.2$  MeV),  $^{228}\text{Ac}$  (beta decay,  $Q = 2.13$  MeV) and  $^{208}\text{Tl}$  (beta decay,  $Q = 4.99$  MeV) have to be considered. Assuming radioactive equilibrium the beta/gamma background rate due to both chains can be estimated by  $b_1 \simeq M_{\text{U}} \cdot 6 \cdot 10^3 \text{ s}^{-1} + M_{\text{Th}} \cdot 4 \cdot 10^3 \text{ s}^{-1}$ , where the total mass of U and Th is given in gram. Taking into account the total scintillator mass of the neutrino target plus the  $\gamma$ -catcher, this rate can be expressed by  $b_1 \simeq 3 \text{ s}^{-1} (c_{\text{U,Th}}/10^{-11})$ , where  $c_{\text{U,Th}}$  is the mass concentration of Uranium and Thorium in the liquid. The contribution from  $^{40}\text{K}$  can be expressed by  $b_2 \simeq 1 \text{ s}^{-1} (c_{\text{K}}/10^{-9})$ , where  $c_{\text{K}}$  is the mass concentration of natural K in the liquid.

The background contribution due to U, Th and K in the acrylic vessels can be written as  $b_3 \simeq 2 \text{ s}^{-1} (a_{\text{K}}/10^{-7}) + 5 \text{ s}^{-1} (a_{\text{U,Th}}/10^{-9})$ , where  $a_{\text{K}}$  and  $a_{\text{U,Th}}$  describe the mass concentrations of K, U and Th in the acrylic. In total, the intrinsic beta/gamma rate is the sum  $b = b_1 + b_2 + b_3$ . In the CTF of the Borexino experiment at Gran Sasso, concentration values of  $c_{\text{U,Th}} < 10^{-15}$  and  $c_{\text{K}} < 10^{-12}$  have been measured for two liquid scintillators (PC and PXE) with volumes of about 4 m<sup>3</sup>. Upper limits on radioactive trace elements in acrylic have been reported

to be  $a_{\text{U,Th}} < 3 \cdot 10^{-12}$  by the SNO collaboration [SNO02]. Gamma spectroscopy measurements show upper limits of  $a_{\text{K}} < 1 \cdot 10^{-9}$ . This shows that in principle the beta/gamma rate in the detector due to intrinsic radioactive elements can be kept at levels well below  $1 \text{ s}^{-1}$ . The aimed concentration values for this goal are given in Table 7.1.

Element	allowed concentration (g/g) for $b < 1 \text{ s}^{-1}$
Uranium, Thorium in scintillator	$\sim 10^{-12}$
Potassium in scintillator	$\sim 10^{-10}$
Uranium, Thorium in acrylic vessels	$\sim 10^{-10}$
Potassium in acrylic vessels	$\sim 10^{-8}$

Table 7.1: Upper limits on U, Th and K concentrations in the liquid scintillator and acrylic vessels to achieve a beta/gamma rate below  $1 \text{ s}^{-1}$

### 7.1.2 External gamma background

According to the experience gained in the CTF of Borexino the dominant contribution to the external gamma background is expected to come from the photomultipliers (PMTs) and structure material. Again contributions from U, Th and K have to be considered. However, because of the shielding of the buffer region only the 2.6 MeV gamma emission from  $^{208}\text{Tl}$  has to be taken into account. The activity of one PMT in the CTF (structure material included) is known to be  $\sim 0.4 \text{ s}^{-1}$ . The shielding factor  $S$  due to the buffer liquid can be calculated to be  $S \sim 10^{-2}$ . Hence, the resulting gamma background in the neutrino target plus the  $\gamma$ -catcher can be written as  $b_{\text{ext}} \simeq 2 \text{ s}^{-1} (N_{\text{PMT}}/500)$ , where  $N_{\text{PMT}}$  is the number of PMTs.

## 7.2 Neutron background

### 7.2.1 Intrinsic background sources

Neutrons inside the target may be produced by spontaneous fission of heavy elements and by  $(\alpha, n)$ -reactions. For the rate of both contributions the concentrations of U and Th in the liquid are the relevant parameters. The neutron rate in the target region can be written as  $n_{\text{int}} \simeq 0.4 \text{ s}^{-1} (c_{\text{U,Th}}/10^{-6})$ . Hence, for the aimed concentration values as described above the intrinsic contribution to the neutron background is negligible.

### 7.2.2 External background sources

Several sources contribute to the external neutron background. We first discuss external cosmic muons which produce neutrons in the target region via spallation and muon capture. Those muons intersect the detector and should be identified by the veto. However, some neutrons may be captured after the veto time window. Therefore we estimate the rate of neutrons, which are generated by spallation processes of through going muons and by stopped negative muons which are captured by nuclei.

The first contribution is estimated by calculating the muon flux for different shielding values and taking into account a  $E^{0.75}$  dependence for the cross section of

neutron production, where  $E$  is the depth dependent mean energy of the total muon flux. The absolute neutron flux is finally obtained by considering measured values in several experiments (LVD [LVD99], MACRO [MAC98], CTF [CTF98]) in the Gran Sasso underground laboratory and extrapolating these results by comparing muon fluxes and mean energies for the different shielding factors. Table 7.2 gives the expected neutron rate depending on the shielding.

Overburden (m.w.e.)	Muon rate ( $s^{-1}$ )	Mean muon energy (GeV)	Neutrons ( $s^{-1}$ )
40	$1.1 \cdot 10^3$	14	2
60	$5.7 \cdot 10^2$	19	1.4
80	$3.5 \cdot 10^2$	23	1
100	$2.4 \cdot 10^2$	26	0.7
300	$2.4 \cdot 10^1$	63	0.15

Table 7.2: Estimated neutron rate in the active detector region due to through going cosmic muons.

Negative muons which are stopped in the target region can be captured by nuclei where a neutron is released afterwards. The rate can be estimated quite accurately by calculating the rate of stopped muons as a function of the depth of shielding and taking into account the ratio between the  $\mu$ -life time and  $\mu$ -capture times. As the capture time in Carbon is known to be around  $25 \mu s$  ( $\approx 1$  ms in H) only about 10 % of captured muons may create a neutron. Since the concentration in Gd is so low, its effect can be neglected here. The estimated results are shown in Table 7.3. The neutron generation due to through going muons dominates.

Overburden (m.w.e.)	Muon stopping rate ( $t^{-1} s^{-1}$ )	Neutrons ( $s^{-1}$ )
40	$5 \cdot 10^{-1}$	0.7
60	$3 \cdot 10^{-1}$	0.4
80	$1.2 \cdot 10^{-1}$	0.2
100	$6 \cdot 10^{-2}$	0.08
300	$2.5 \cdot 10^{-3}$	0.003

Table 7.3: Estimated neutron rate in the target region due to stopped negative muons.

### 7.2.3 Beta-neutron cascades

Muon spallation on  $^{12}C$  nuclei in the organic liquid scintillator may generate  $^8He$ ,  $^9Li$ , and  $^{11}Li$  which may undergo beta decay with a neutron emission. In that case those background events show the same signature as a neutrino event. For shallow shielding depths the muon flux is too high to allow tagging by the muon veto, as the lifetimes of these isotopes are between 0.1 s and 1 s. The cross sections for the production of  $^8He$ ,  $^9Li$  have been measured by a group of TUM at the SPS at CERN with muon energies of 190 GeV (NA54 experiment [Hag00]). In this experiment only the combined production  $^8He + ^9Li$  were obtained without ability to separate each isotope. An estimate for the background rates for shallow depth experiments like CHOOZ can be obtained from results of the KamLAND experiment by calculating the muon flux for energies above  $\sim 500$  GeV [Hor03]. With this assumption an event rate of about 0.4 per day in the target region can be estimated for a 300 m.w.e.

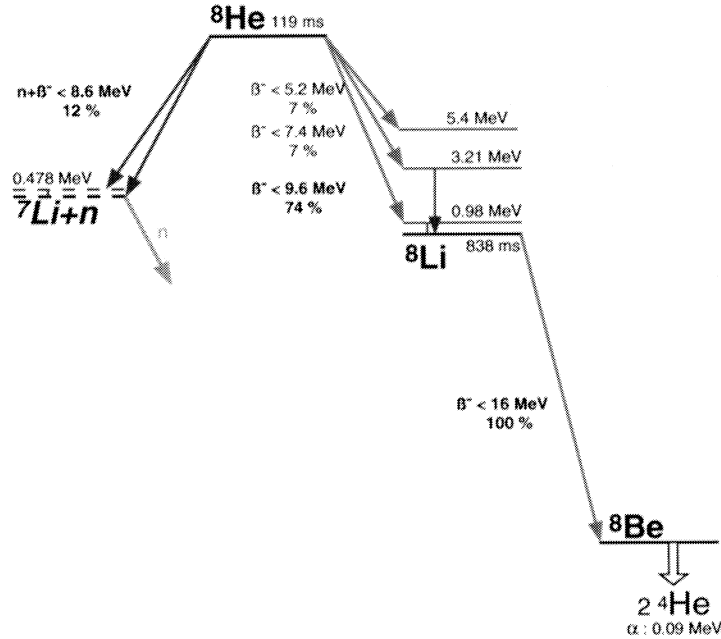


Figure 7.1: Relevant branching ratios for the decay of the  $^8\text{He}$  isotope, normalized to 100 %. Half-lives are quoted, as well as the end-point of the  $\beta$  decays. Neutrons emitted in these decays are typically around 1 MeV. The double cascade decay to the  $^8\text{Be}$  offer a possibility to measure , *in situ*, the production rate.

shielding. A more conservative estimate is obtained assuming a  $E^{0.75}$  scaling as we did in calculating the neutron flux. Then the rate should be around 2 events per day. In Table 7.4 all radioactive  $^{12}\text{C}$ -spallation products including the beta-neutron cascades are shown with the estimated event rates in both detectors.

The Q-values of the beta-neutron cascade decays is 8.6 MeV, 11.9 MeV, 20.1 MeV for  $^8\text{He}$ ,  $^9\text{Li}$ , and  $^{11}\text{Li}$ , respectively. In the experiment the  $^8\text{He}$  production rate might be measured if we set a dedicated trigger after a muon event in the target region looking for the double cascade of energetic betas ( $^8\text{He} \rightarrow ^8\text{Li} \rightarrow ^8\text{Be}$ ) occurring in 50 % of all  $^8\text{He}$  decays (see Figures 7.1 and 7.2). Nothing similar exist in the case of the  $^9\text{Li}$ , but the beta endpoint is here above the endpoint of positron induced by reactor antineutrinos. Nevertheless, from the NA54 experiment [Hag00] results the total cross section of  $^8\text{He} + ^9\text{Li}$  is known, and if the  $^8\text{He}$  is evaluated separately, some redundancy on the total  $\beta$ -neutron cascade will be available. Figure 7.1 shows the relevant branching ratios of the  $^8\text{He}$  isotope, normalized to 100 %. The neutrons emitted in these decays are typically around 1 MeV. Figure 7.2 shows the relevant branching ratios of the  $^9\text{Li}$  isotope, normalized to 100 %.

#### 7.2.4 External neutrons and correlated events

Very fast neutrons, generated by cosmic muons outside the detector, may penetrate into the target region. As the neutrons are slowed down through scattering, recoil protons may give rise to a visible signal in the detector. This is followed by a delayed neutron capture event. Therefore, this type of background signal gives the right time correlation and can mimic a neutrino event. Pulse shape discrimination

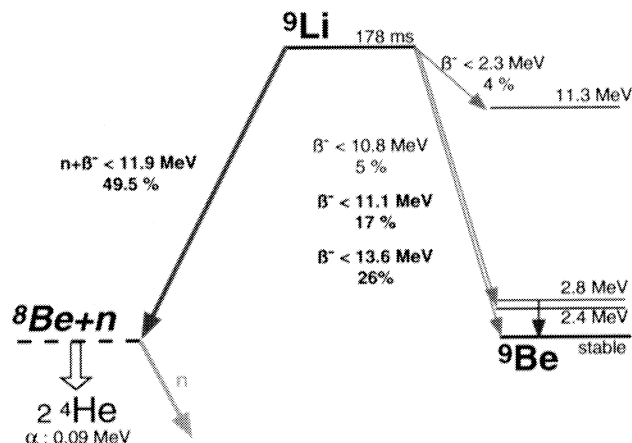


Figure 7.2: Relevant branching ratios for the decay of the  ${}^9\text{Li}$  isotope, normalized to 100 %. Half-lives are quoted, as well as the end-point of the  $\beta$  decays. Neutrons emitted in these decays are typically around 1 MeV. In case of  $\beta$  decay to  ${}^8\text{Be}$ , the latter transform immediately to two low energy  $\alpha$  particles.

in order to distinguish between  $\beta$  events and recoil protons is in principle possible, but should not be applied in the analysis as additional statistical and systematic uncertainties should be avoided in the experiment. As the muon is not seen by the veto, those correlated events may be dangerous for the experiment.

Therefore a Monte-Carlo program has been written to estimate the correlated background rate for a shielding depth of 100 m.w.e. and flat topology. In order to test the code the correlated background for the old Chooz experiment (different detector dimensions, 300 m.w.e. shielding) has been calculated with the same program. The most probable background rate was determined to be 0.8 counts per day. A background rate higher than 1.6 events per day is excluded by 90 % C.L. This has to be compared with the measured rate of 1.1 events per day. We conclude that the Monte-Carlo program reproduces the real correlated background value within roughly a factor 2.

For Double-Chooz we calculated the correlated background rate for 100 m.w.e. shielding and estimated the rates for other shielding values by taking into account the different muon fluxes and assuming a  $E^{0.75}$  scaling law for the probability to produce neutrons. The neutron capture rate in the Gd loaded scintillator for an overburden of 100 m.w.e. is about 300/h. However, only 0.5 % from those neutrons create a signal in the scintillator within the neutrino window (i.e. between 1 MeV and 8 MeV), because most deposit in total much more energy during the multiple scattering processes until they are slowed down to thermal energies. The quenching factors for recoil protons and carbon nuclei has been taken into account. In addition around 75 % from those events generate a signal in the muon veto above 4 MeV (visible  $\beta$  equivalent energy). In total the correlated background rate is estimated to be about 3.0 counts per day for 100 m.w.e. shielding. In Table 7.5 the estimated correlated background rates are shown for different shielding depths.

The correlated background rates can be compared with accidental rates, where by chance a neutron signal falls into the time window opened by a  $\beta^+$ -like event.

Isotopes	Near detector		Far detector	
	$R_\mu$ ( $E^{0.75}$ scaling)	$R_\mu$ ( $E > 500$ GeV)	$R_\mu$ ( $E^{0.75}$ scaling)	$R_\mu$ ( $E > 500$ GeV)
$^{12}\text{B}$		not measured		
$^{11}\text{Be}$	< 18	< 3.8	< 2.0	< 0.45
$^{11}\text{Li}$		not measured		
$^9\text{Li}$	$17 \pm 3$	3.6	$1.7 \pm 0.3$	0.36
$^8\text{Li}$	$31 \pm 12$	6.6	$3.3 \pm 1.2$	0.7
$^8\text{He}$		$^8\text{He}$ & $^9\text{Li}$ measured together		
$^6\text{He}$	$126 \pm 12$	26.8	$13.2 \pm 1.3$	2.8
$^{11}\text{C}$	$7100 \pm 455$	1510	$749 \pm 48$	159.3
$^{10}\text{C}$	$904 \pm 114$	192	$95 \pm 12$	20.2
$^9\text{C}$	$38 \pm 12$	8.1	$4.0 \pm 1.2$	0.85
$^8\text{B}$	$60 \pm 11$	12.7	$5.9 \pm 1.2$	1.25
$^7\text{Be}$	$1800 \pm 180$	382.9	$190 \pm 19$	40.4

Table 7.4: Radioactive isotopes produced by muons and their secondary shower particles in liquid scintillator targets at the CHOOZ near and far detectors. The rates  $R_\mu$  (events/d) are given for a target of  $4.4 \times 10^{29}$   $^{12}\text{C}$  (For a mixture of 80 % Dodecane and 20 % PXE,  $12.7 \text{ m}^3$ ) at a depth of 60 m.w.e. for the near detector and 300 m.w.e. for the far detector. Because of the positron annihilation the visible energy in  $\beta^+$  decays is shifted by 1.022 MeV.  $^9\text{Li}$  and  $^8\text{He}$  could not be evaluated separately. Columns 3 and 5 correspond to an estimate of the number of events assuming that the isotopes are produced only by high energy muon showers  $E > 500$  GeV [Hor03]. A neutrino signal rate of 85 events per day is expected at CHOOZ-far, without oscillation effect (for a power plant running at nominal power, both dead time and detector efficiency are not taken into account here).

The background contribution due to accidental delayed coincidences can be determined *in situ* by measuring the single counting rates of neutron-like and  $\beta^+$ -like events. Therefore the accidentals are not so dangerous as correlated background events. Taking for granted we reach reasonably low concentrations of radioactive elements in the detector materials, especially in the scintillator itself (see discussion above), the beta-gamma rate above 1 MeV can be expected to be about a few counts per second. If the time window for the delayed coincidence is  $\sim 200 \mu\text{s}$  (this should allow a highly efficient neutron detection in Gd loaded scintillators), and the veto efficiency is at 98 % the accidental background rates can be estimated as depicted in Table 7.6. The rate of neutrons which cannot be correlated to muons (“effective neutron rate”) is calculated by  $n_{\text{eff}} = n_{\text{tot}} \cdot (1 - \epsilon)$ , where  $n_{\text{tot}}$  is the total neutron rate (sum of the numbers given in Table 7.2 and 7.3) and  $\epsilon$  is the veto efficiency. If the veto efficiency is 98 % or better, the accidental background for the far detector is far below one event per day (see following Table 7.6).

### 7.2.5 Conclusion

We conclude that correlated events are the most severe background source for the experiment. Two processes mainly contribute:  $\beta$ -neutron cascades and very fast external neutrons. Both types of events are coming from spallation processes of high energy muons. In total the background rates for the near detector will be



Overburden (m.w.e.)	Total neutron rate in $\nu$ -target ( $\text{h}^{-1}$ )	Correlated background rate ( $\text{d}^{-1}$ )
40	829	8.4
60	543	5.4
80	400	4.2
100	286	3.0
300	57	0.5

Table 7.5: Estimated neutron rate in the target region and the correlated background rate due to fast neutrons generated outside the detector by cosmic muons.

Overburden (m.w.e.)	Effective neutron rate ( $\text{h}^{-1}$ )	Accidental background rate ( $\text{d}^{-1}$ )
40	97	2.4
60	65	1.6
80	43	1.0
100	28	0.7
300	6	0.15

Table 7.6: Example of estimated accidental event rates for different shielding depths. The rates scale with the total beta-gamma rate above 1 MeV (here  $b_{tot} = b_{ext} + b \approx 2.5 \text{ s}^{-1}$ ), the time window (here  $\tau = 200 \mu\text{s}$ ) and the effective neutron background rate (here a muon veto efficiency of 98 % was assumed).

between 9/d and 23/d if a shielding of 60 m.w.e. is chosen. For the far detector a total background rate between 1/d and 2/d can be estimated.



## Chapter 8

# Experimental Errors

### 8.1 From CHOOZ to Double-CHOOZ

In the first CHOOZ experiment, the total systematic error amounted to 2.7 %. The goal of Double-CHOOZ is to reduce the overall systematic uncertainty to 0.6 %. A summary of the CHOOZ systematic errors is given in Table 8.1 [CHO03]. The right column presents the new experiment goals. Lines 1,4, and 5 correspond to systematic uncertainties related to the reactor flux and the cross section of neutrinos on the target protons. These errors become negligible if one uses two antineutrino detectors located at different baselines. In order to improve the systematic uncertainties related to the detector and to the  $\bar{\nu}_e$  selection cuts, the Double-CHOOZ experiment will take advantage of the latest technical developments achieved by the recent scintillator detector CHOOZ [CHO03], CTF [CTF98], KamLAND [KAM02], Borexino [Sch99], and the LENS R&D phase [LEN99].

	CHOOZ	Double-CHOOZ
Reactor cross section	1.9 %	—
Number of protons	0.8 %	0.2 %
Detector efficiency	1.5 %	0.5 %
Reactor power	0.7 %	—
Energy per fission	0.6 %	—

Table 8.1: Overview of the systematic errors of the CHOOZ and Double-CHOOZ experiment.

### 8.2 Relative normalization of the two detectors

The goal of Double-CHOOZ is to use two  $\bar{\nu}_e$  detectors in order to cancel or decrease significantly the systematic uncertainties that limit the  $\theta_{13}$  neutrino mixing angle measurement. However, beside those uncertainties, the relative normalization between the two detectors is the most important source of error and must be carefully controlled. This section covers the uncertainties related to the  $\bar{\nu}_e$  interaction and selection in the analysis, as well as the electronics and data acquisition dead times.

## 8.3 Detector systematic uncertainties

### 8.3.1 Solid angle

The distance from the CHOOZ detector to the cores of the nuclear plant have been measured to within  $\pm 10$  cm by the CHOOZ experiment. This translates into a systematic error of 0.15 % in Double-CHOOZ, because the effect becomes relatively more important for the near detector located 100-200 meters away from the reactor. Specific studies are currently ongoing to guarantee this 10 cm error. Furthermore, the “barycenter” of the neutrino emission in the reactor core must be monitored with the same precision. In a previous experiment at Bugey [BUG96], a 5 cm change of this barycenter was measured and monitored, using the instrumentation of the nuclear power plant [Gar92]. Our goal is to confirm that this error could be kept below 0.2 %.

### 8.3.2 Number of free protons in the target

#### 8.3.2.1 Volume measurement

In the first CHOOZ experiment, the volume measurement was done with an absolute precision of 0.3 % [CHO03]. The goal is to reduce this uncertainty by a factor of two, but only on the relative volume measurement between the two inner acrylic vessels (the other volumes do not constitute the  $\bar{\nu}_e$  target). An R&D program has already started in order to find the optimal solution for the relative volume determination (See Section 4.2.2). Among some ideas under study, we plan to use the same mobile tank to fill both targets; a pH-based measurement is being studied as well. A more accurate measurement could be performed by combining a traditional flux measurement with a weight measurement of the quantity of liquid entering the acrylic vessel. Furthermore we plan to build both inner acrylic targets at the manufacturer and to move each of them as a single unit into the detector site. A very precise calibration of both inner vessels is thus foreseen at the manufacturer (filling tests).

#### 8.3.2.2 Density

The uncertainty of the density of the scintillator is  $\sim 0.1$  %. The target liquid will be prepared in a large single batch, so that they can be used for the two detector fillings. The same systematic effect will then occur in both detectors and will not contribute to the overall systematic error (this effect will be included automatically in the absolute normalization error, see Chapter 9). However, the measurement and control of the temperature will be mandatory to guarantee the stability of the density in both targets (otherwise it would contribute to the relative uncertainty, see Chapter 9). To thermalize both  $\bar{\nu}_e$  targets, the temperature control and circulation of the liquid in the external veto is foreseen.

#### 8.3.2.3 Number of hydrogen atoms per gramme

This quantity is very difficult to measure, and the error is of the order of 1 %; however, the target liquid will be prepared in a large single batch (see above). This will guarantee that, even if the absolute value is not known to a high precision, both detectors will have the same number of hydrogen atoms per gramme. This uncertainty, which originates in the presence of unknown chemical compounds in the liquid, does not change with time.

### 8.3.3 Neutron efficiency

The thermal neutron is captured either on hydrogen or on Gadolinium (other reactions such as Carbon captures can be neglected). We outline here the systematical errors related to the neutron signal.

#### 8.3.3.1 Gadolinium concentration

Gd concentration can be extracted from a time capture measurement done with a neutron source calibration (see Chapter 6). A very high precision can be reached on the neutron efficiency (0.3 %) by measuring the detected neutron multiplicity from a Californium source (Cf). This number is based on the precision quoted in [CHO03], but taking away the Monte-Carlo uncertainty, since we work with two-identical detectors. This precision is expected to be better by a factor of two in the Double-CHOOZ experiment because it is easier to compare two experimental measurements in identical detectors than to compare a theoretical spectrum with a measurement. We can increase our sensitivity to very small differences in the response from both detectors by using the same calibration source for the measurements. The Californium source calibration can be made all along the z-axis of the detector, and is thus sensitive to spatial effects due to the variation of Gd concentration (staying far enough from the boundary of the target, and searching for a top/down asymmetry). A difference between the time capture of both detectors could also be detected with a sensitivity slightly less than 0.3 %.

#### 8.3.3.2 Spatial effects

We consider here the spill in/out effect, i.e the edge effect associated with neutron capture close to the acrylic vessel surrounding the inner target [CHO03], and the angle between the neutron direction and the edge of the acrylic target that is slightly different between the two detectors. The  $\sim 1$  % spill in/out effect observed in the first CHOOZ experiment [CHO03] cancels by using a set of two identical detectors (same effect). Nevertheless the second effect (angle) persists, but is considered to be negligible.

### 8.3.4 Positron efficiency

The simulation of the Double-CHOOZ detectors confirms that a 500 keV energy cut induces a positron inefficiency smaller than 0.1 % (see Chapter 4). The relative uncertainties between both detectors lead thus to an even smaller systematic error and is therefore negligible.

## 8.4 Selection cuts uncertainties

The analysis cuts are potentially important sources of systematic errors. In the first CHOOZ experiment, this amounted in total to 1.5 % [CHO03]. The goal of the new experiment is to reduce this error by a factor of three. The CHOOZ experiment used 7 analysis cuts to select the  $\bar{\nu}_e$  (one of them had 3 cases, see Section 8.7 of [CHO03]). In Double-CHOOZ we plan to reduce the number of selection cuts to 3 (one of them will be very loose, and may not even be used). This can be achieved because of reduction of the number of accidentals background events, only possible with the new detector design (see Chapter 3). To select  $\bar{\nu}_e$  events we have to identify the prompt positron followed by the delayed neutron (delayed in time and separated in space). The trigger will require two local energy depositions of more than 500 keV in less than 200  $\mu$ s.

### 8.4.1 Identifying the prompt positron signal

Since any  $\bar{\nu}_e$  interaction deposits at least 1 MeV (slightly less due to the energy resolution effect) the energy cut at 500 keV does not reject any  $\bar{\nu}_e$  events. As a consequence, there will not be any systematic error associated with this cut (see Figure 8.1). The only requirement is the stability of the energy selection cut, which is related to the energy calibration (see Chapter 6).

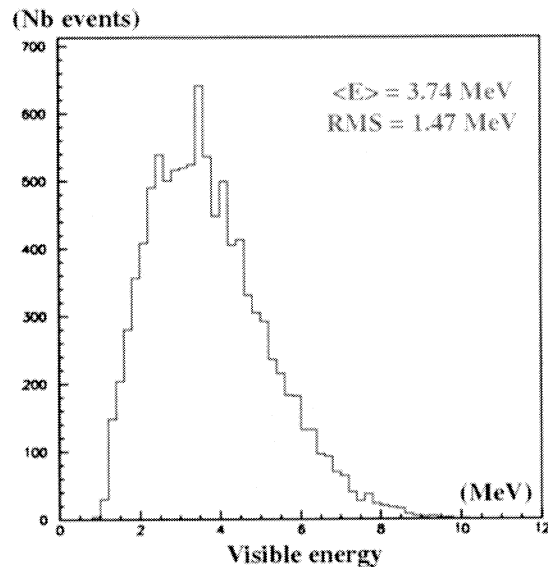


Figure 8.1: Simulation of the positron energy spectrum (in MeV) measured with the Double-CHOOZ detector (10,000 events, without backgrounds). Positron energy is fully contained with a probability of 99.9 %, as a consequence of the 60 cm scintillating buffer.

### 8.4.2 Identifying the neutron delayed signal

The energy spectrum of a neutron capture has two peaks, the first peak at 2.2 MeV tagging the neutron capture on hydrogen, and the second peak at around 8 MeV tagging the neutron capture on Gd (see Figure 8.2). The selection cut that identifies the neutron will be set at about 6 MeV, which is above the energy of neutron capture on hydrogen and all radioactive contamination. At this energy of 6 MeV, an error of  $\sim 100$  keV on the selection cut changes the number of neutrons by  $\sim 0.2$  %. This error on the relative calibration is achievable by using identical Cf calibration source for both detectors (see Chapter 6).

### 8.4.3 Time correlation

The neutron time capture on Gd in the CHOOZ detector is displayed in Figure 8.3. But since the exact analytical behaviour describing the neutron capture time on Gd is not known, the absolute systematic error for a single detector cannot be significantly improved with respect to CHOOZ [CHO03]. However, the uncertainty originating from the liquid properties disappears by comparing the near and far detector neutron time capture. The remaining effect deals with the control of the

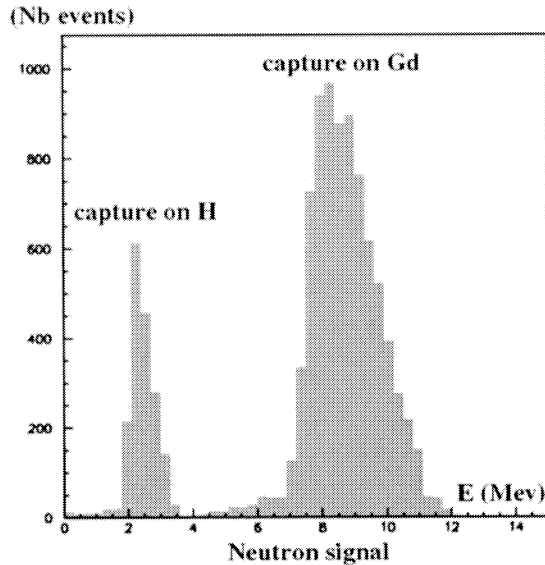


Figure 8.2: Simulation of the neutron energy spectrum (in MeV) measured with the Double-CHOOZ detector (10,000 events, without backgrounds). There are two energy peaks for the neutron capture on hydrogen (releasing 2.2 MeV) and on gadolinium (releasing about 8 MeV). The Double-CHOOZ experiment will select all neutron events with an energy greater than 6 MeV. The resulting systematic uncertainty thus depends on the relative calibration between the near and far detectors.

electronic time cuts. For completeness, a redundant system will be designed in order to control perfectly these selection cuts (for example time tagging in a specialized unit and using Flash-ADC's).

#### 8.4.4 Space correlation

The distance cut systematic error (distance between prompt and delayed events) was published as 0.3 % in the CHOOZ experiment [CHO03]. This cut is very difficult to calibrate, since the rejected events are typically  $\bar{\nu}_e$  candidates badly reconstructed. In Double-CHOOZ, this cut will be either largely relaxed (two meters instead of one meter for instance) or totally suppressed, if the accidentals event rate is low enough, as expected from current simulations (see Chapter 7).

#### 8.4.5 Veto and dead time

The Double-CHOOZ veto will consist of a liquid scintillator and have a thickness of 60 cm liquid scintillator at the far site, and even larger at the near detector site. The veto inefficiency comes from the through going cables and the supporting structure material. This inefficiency was low enough in the first experiment, and should be acceptable for the CHOOZ-far detector. However, it must be lowered for the near detector because the muon flux is a factor 30 higher for a shallower overburden of 60 m.w.e.. A constant dead time will be applied in coincidence with each through going muon. This has to be measured very carefully since the resulting dead time will be very different for the two detectors: a few percent at the far detector, and

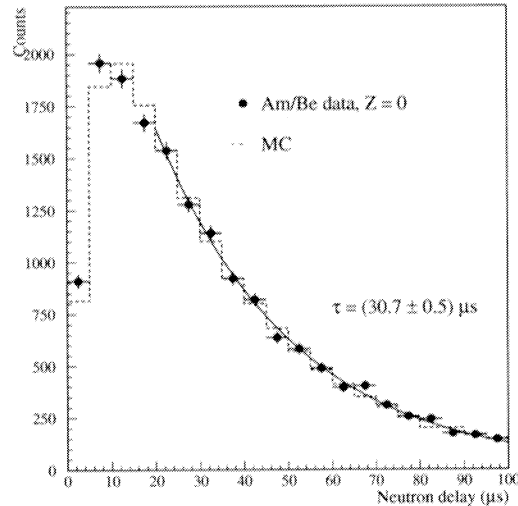


Figure 8.3: Neutron delay distribution measured with the Am/Be source at the detector centre in the CHOOZ detector [CHO03]. The time origin is defined by the 4.4 MeV  $\gamma$ -ray.

at moreless 30 % at the near detector. A 1 % precision on the knowledge of this dead time is mandatory. This will require the use of several independent methods:

- the use of a synchronous clock, to which the veto will be applied,
- a measurement of the veto gate with a dedicated flash ADC,
- the use of an asynchronous clock that randomly generates two particles mimicking the antineutrino tag (with the time between them characteristic of the neutron capture on Gd). With this method, all dead times (originating from the veto as well as from the data acquisition system) will be measured simultaneously. The acquisition of a few thousands such events per day would achieve the required precision,
- the generation of sequences of veto-like test pulses (to compare the one predicted dead time to the actually measured).

#### 8.4.6 Electronics and acquisition

The trigger will be rather simple. It will use only the total analog sum of energy deposit in the detector. Two signals of more than 500 keV in 200  $\mu\text{s}$  will be required.

#### 8.4.7 Summary of the systematic uncertainty cancellations

A summary of the systematic errors associated with  $\bar{\nu}_e$  event selection cuts is given in Table 8.2. We summarize in Table 8.3 the systematic uncertainties that totally cancel, or to a large extent, in the Double-CHOOZ experiment. The error on the absolute knowledge of the chemical composition of the Gd scintillator disappears.

<sup>1</sup>Energy cut on gamma spectrum from a Gd neutron capture.



selection cut	CHOOZ		Double-CHOOZ	
	rel. error (%)	rel. error (%)	rel. error (%)	Comment
positron energy*	0.8	0	0	not used
positron-geode distance	0.1	0	0	not used
neutron capture	1.0	0.2	0.2	Cf calibration
capture energy containment	0.4	0.2	0.2	Energy calibration
neutron-geode distance	0.1	0	0	not used
neutron delay	0.4	0.1	0.1	—
positron-neutron distance	0.3	0 – 0.2	0 – 0.2	0 if not used
neutron multiplicity*	0.5	0	0	not used
combined*	1.5	0.2-0.3	0.2-0.3	—

\*average values

Table 8.2: Summary of the neutrino selection cut uncertainties. CHOOZ values have been taken from [CHO03].

	CHOOZ	Double-CHOOZ
Reactor power	0.7 %	negligible
Energy per fission	0.6 %	negligible
$\bar{\nu}_e$ /fission	0.2 %	negligible
Neutrino cross section	0.1 %	negligible
Number of protons/cm <sup>3</sup>	0.8 %	0.2 %
Neutron time capture	0.4 %	negligible
Neutron efficiency	0.85 %	0.2 %
Neutron energy cut <sup>1</sup>	0.4 %	0.2 %

Table 8.3: Summary of systematic errors that cancel or are significantly decreased in Double-CHOOZ.

There remains only the measurement error on the volume of target (relative between two detectors). The error on the absolute knowledge of the gamma spectrum from a Gd neutron capture disappears. However, there will be a calibration error on the difference between the 6 MeV energy cut in both detectors.

#### 8.4.8 Systematic uncertainties outlook

Table 8.4 summarizes the identified systematic errors that are currently being considered for the Double-CHOOZ experiment.

### 8.5 Background subtraction error

The design of the detector will allow a Signal/Background (S/B) ratio of about 100 to be achieved (compared to 25 at full reactor power in the first experiment [CHO03]). The knowledge of the background at a level around 30-50 % will reduce the background systematic uncertainties to an acceptable level. In the Double-CHOOZ experiment, two background components have been identified, uncorrelated and correlated (see Chapter 7). Among those backgrounds, one has:

- The accidental rate, that can be computed from the single event measurements, for each energy bin.

	After CHOOZ	Double-CHOOZ Goal
Solid angle	0.2 %	to confirm
Volume	0.2 %	to confirm
Density	0.1 %	0.1 %
Ratio H/C	0.1 %	0.1 %
Neutron efficiency	0.2 %	0.1 %
Neutron energy	0.2 %	0.2 %
Spatial effects	neglect?	to confirm
Time cut	0.1 %	0.1 %
Dead time(veto)	0.25 %	to improve
Acquisition	0.1 %	0.1 %
Distance cut	0.3 %	0-0.2 %
Grand total	0.6 %	< 0.6 % (to confirm)

Table 8.4: The column “After CHOOZ” lists the systematic errors that can be achieved without improvement of the CHOOZ published systematic uncertainties [CHO03]. In Double-CHOOZ, we estimate the total systematic error on the normalization between the detectors to be less than 0.5 %. The aim of the work prior the final proposal is to confirm this number, and thus increase the safety margin of the experiment.

- The fast neutrons creating recoil protons, and then a neutron capture. This background was dominant in the first experiment [CHO03]. The associated energy spectrum is relatively flat up to a few tens of MeV.
- The cosmogenic muon induced events, such as  ${}^9\text{Li}$  and  ${}^8\text{He}$ , that have been studied and measured at the NA54 CERN experiment [Hag00] in a muon beam as well as in the KamLAND experiment [KAM02]. Their energy spectrum goes well above 8 MeV, and follows a well defined shape.

The backgrounds that will be measured are:

- Below 1 MeV (this was not possible in the first experiment, due to the different detector design and the higher energy threshold)
- Above 8 MeV (where there remains only 0.1 % of the neutrino signal).
- By extrapolating from the various thermal power of the plant (refueling will result in two months per year at half power).

From the measurement of the accidental events energy shape, and from the extraction of the cosmogenic events shape, the shape of the fast neutron events can be obtained with a precision greater than what is required.

## 8.6 Liquid scintillator stability and calibration

The experiment has some sensitivity to a slight distortion induced by neutrino oscillations. A rate only analysis would only provide a sensitivity that is twice the quoted value of 0.03 on  $\sin^2(2\theta_{13})$ . From the simulation, identical energy scales at the 1 % level is necessary. The specification of no more than 100 keV scale difference at 6 MeV is achieved if this 1 % level is obtained. This relative calibration is easier than an absolute linearity, but still very important to consider in the detector design. We can, for example, move the same calibration radioactive sources from one detector to the other, and directly compare the position of the well defined calibration peaks.

## Chapter 9

# Sensitivity and discovery potential

We describe here the details of the simulation of the Double-CHOOZ experiment. The sensitivity to  $\sin^2(2\theta_{13})$  is presented in Section 9.3, and we present the discovery potential of the experiment in Section 9.4. The statistical analysis (systematic error handling) introduced here is based on the work of [Hub02].

### 9.1 The neutrino signal

In this section we describe the set of parameters used in the simulation.

#### 9.1.1 Reactor $\bar{\nu}_e$ spectrum

The  $\bar{\nu}_e$  spectrum above detection threshold is the result of  $\beta^-$  decays of  $^{235}\text{U}$ ,  $^{238}\text{U}$ ,  $^{239}\text{Pu}$  and  $^{241}\text{Pu}$  fission products. Measurements for  $^{235}\text{U}$ ,  $^{239}\text{Pu}$  and  $^{241}\text{Pu}$  and theoretical calculations for  $^{238}\text{U}$  are used to evaluate the  $\bar{\nu}_e$  spectrum [Sch85, Hah89]. While a nuclear reactor operates, the fission products proportions evolve in time; as an approximation in this evaluation, we use a typical averaged fuel composition during a reactor cycle corresponding to 55.6 % of  $^{235}\text{U}$ , 32.6 % of  $^{239}\text{Pu}$ , 7.1 % of  $^{238}\text{U}$  and 4.7 % of  $^{241}\text{Pu}$ . The mean energy release per fission is then 203.87 MeV and the energy weighted cross section for  $\bar{\nu}_e p \rightarrow n e^+$  amounts to  $\langle\sigma\rangle_{\text{fission}} = 5.825 \cdot 10^{-43} \text{ cm}^2$  per fission.

#### 9.1.2 Detector and power station features

Table 9.1 contains the principal features of the CHOOZ power station nuclear cores, as well as their distances from the near and far detectors. Table 9.2 presents the

	CHOOZ-B-1	CHOOZ-B-2
Electrical Power (raw/net $\text{GW}_e$ )	1.516/1.455	1.516/1.455
Thermal power ( $\text{GW}_{\text{th}}$ )	4.2	4.2
Global load factor	80 %	80 %
Near detector distance	100-200 m	100-200 m
Far detector distance	1,000 m	1,100 m

Table 9.1: Chooz power station main features [CEA01].

characteristics of the detectors used in the simulation. We considered a target

scintillator composition of 20 % of PXE and 80 % of dodecane (see Chapter 5). This translates into  $8.33 \cdot 10^{29}$  free protons in the  $12.7 \text{ m}^3$  inner acrylic vessel. For simplicity we assume that the two cores are equivalent to a single core of  $8.4 \text{ GW}_{\text{th}}$  located 150 m away from the near detector and 1,050 m from the far detector. We checked that a full simulation with two separated cores at CHOOZ does not change the results presented here. The global load factor of the CHOOZ nuclear reactor

	Near Detector	Far Detector
Distance	100 m	1,050 m
Target volume	$12.7 \text{ m}^3$	$12.7 \text{ m}^3$
Target mass	10.16 tons	10.16 tons
Free H	$8.33 \cdot 10^{29}$	$8.33 \cdot 10^{29}$
Detection efficiency	80 %	80 %
Reactor efficiency	80 %	80 %
Dead time	50 %	a few %
Overall efficiency	32 %	64 %
$\bar{\nu}_e$ events after 3 years	3,213,000	58,000

Table 9.2: Detector parameters used in the simulation. As an example we take here the near detector distance at 100 m. Results presented in this chapter don't change if this distance is increased to 200 m.

is taken to be 80 %. We assume that the detection efficiency for both detectors is 80 % (69.8 % in CHOOZ [CHO03]). We neglect the dead time for the far detector (300 m.w.e. overburden). Since the CHOOZ near site will be shallower, between 60 to 80 m.w.e, we apply a dead time of 50 % to be conservative (a  $500 \mu\text{sec}$  cut to each muon crossing the detector leads to a dead time around 30 % at 60 m.w.e). The overall efficiencies used in the simulation for the near and far detectors are thus respectively 32 % and 64 %.

### 9.1.3 Expected number of events

Neglecting the correction terms of order  $\alpha = \left(\frac{\Delta m_{\text{sol}}^2}{\Delta m_{\text{atm}}^2}\right)^2 \approx (2 \cdot 10^{-2})^2$ , we used the following  $\bar{\nu}_e$  survival probability:

$$P_{\bar{\nu}_e \rightarrow \bar{\nu}_e} = 1 - \sin^2(2\theta_{13}) \sin^2\left(1.27 \frac{\Delta m_{23}^2 L[\text{m}]}{E_\nu[\text{MeV}]}\right). \quad (9.1)$$

The expected number of antineutrino events in the near ( $N_i^N$ ) and far detector ( $N_i^F$ ), in the energy bin  $[E_i, E_{i+1}]$ , is

$$N_i^A = \mathcal{F}^A \int_{E_i}^{E_{i+1}} \int_0^{+\infty} S(E_\nu, E'_\nu) \sigma(E_\nu) \phi_i(E_\nu, L^A) P_{\bar{\nu}_e \rightarrow \bar{\nu}_e}(E_\nu, L^A) dE_\nu dE'_\nu, \quad (9.2)$$

where  $A = N, F$ . The cross section  $\sigma$  is given in equation 2.11, and the  $\bar{\nu}_e$  flux is computed according to Figures 2.1 and 2.2. The normalization factor  $\mathcal{F}$  includes the global load factor  $G$  (fraction of running time of the reactors over a year), the reactor thermal power  $P$ , the detector efficiency  $\varepsilon^A$ , the dead time fraction  $D^A$ , the target volume  $V$  and the exposure time  $T$ :

$$\mathcal{F}^A = G \times P \times V \times T \times (1 - D^A) \times \varepsilon^A \quad (9.3)$$

The energy resolution effect is taken into account as follows:

$$S(E, E') = \mathcal{N}\left(E - E', \frac{8\%}{\sqrt{E}}\right), \quad (9.4)$$

where  $\mathcal{N}$  is a Gaussian distribution. In practice, we have used an energy bin size at least four times larger than the energy resolution effect and thus we neglected it in first approximation for this analysis. We checked this approximation by comparing our results with the work of [Hub02, Hub04].

## 9.2 Systematic errors handling

### 9.2.1 $\chi^2$ analysis

In this section we describe the  $\chi^2$ -analysis of the near-far detector set and how we implemented the systematic errors previously discussed. We write  $O_i^A$  the computed number of events observed in  $i^{\text{th}}$  energy bin in near ( $A = N$ ) and far ( $A = F$ ) detectors. The theoretical predictions for the detector  $A$  in the  $i^{\text{th}}$  bin is

$$T_i^A = (1 + a + b^A + c_i) \sum_{j=1}^{N_{\text{cores}}} (1 + f_j) N_{i,j}^A + g^A M_i^A \quad (9.5)$$

where  $a, b^A, c_i, f_j, g^A$  will be the fitted parameters.  $M_i^A$  is the first order correction term to take into account the energy scale uncertainty, obtained by replacing  $E_{\text{vis}}$  by  $(1 + g^A)E_{\text{vis}}$ :

$$M_i^A = \sum_{j=1}^{N_{\text{cores}}} \left. \frac{dN_{i,j}^A(g^A)}{dg^A} \right|_{g^A=0} \quad (9.6)$$

where  $N_{i,j}^A$  is the computed number of events in  $i^{\text{th}}$  bin in detector  $A$  coming from the  $j^{\text{th}}$  reactor core:

$$N_{i,j}^A = \mathcal{F}^A \int_{E_i}^{E_{i+1}} \int_0^{+\infty} S(E_\nu, E'_\nu) \sigma(E_\nu) \phi_i(E_\nu, L_j^A) P_{\bar{\nu}_e \rightarrow \bar{\nu}_e}(E_\nu, L_j^A) dE_\nu dE'_\nu \quad (9.7)$$

which depends on the oscillation parameters through the survival probability. The observed number of events  $O_i^A$  has been chosen to be the computed event number for given ‘‘true values’’ of the oscillation parameters:  $O_i^A = \sum_{j=1}^{N_{\text{cores}}} N_{i,j}^A(\sin^2(2\theta_{13}), \Delta m^2)$ . We used a  $\chi^2$  function including the full spectral information from both detectors:

$$\begin{aligned} \chi^2 = & \sum_{i=1}^{N_{\text{bins}}} \sum_{A=N,F} \frac{(T_i^A - O_i^A - e^A B_i^A)^2}{O_i^A + (\sigma_{\text{b2b}} O_i^A)^2 + B_i^A + (\sigma_{\text{bkg}} B_i^A)^2} \\ & + \left( \frac{a}{\sigma_{\text{abs}}} \right)^2 + \sum_{i=1}^{N_{\text{bins}}} \left( \frac{c_i}{\sigma_{\text{shp}}} \right)^2 + \left( \frac{d - \Delta m_{\text{Best}}^2}{\sigma_{\Delta m^2}} \right)^2 + \sum_{j=1}^{N_{\text{cores}}} \left( \frac{f_j}{\sigma_{\text{cfl}}} \right)^2 \\ & + \sum_{A=N,F} \left[ \left( \frac{b^A}{\sigma_{\text{rel}}} \right)^2 + \left( \frac{g^A}{\sigma_{\text{scl}}} \right)^2 + \left( \frac{e^A}{\sigma_{\text{bkg}}} \right)^2 \right] \end{aligned} \quad (9.8)$$

For each point in the oscillation parameters space, the  $\chi^2$  function has to be minimized with respect to the parameters  $a, b^N, b^F, c_i, g^N, g^F, d, e^N, e^F, f_j$  modeling the systematic errors. The parameter  $a$  refers to the error on the overall normalization of the number of events common to both detectors. Parameters  $b^N$  and  $b^F$  relate to the uncorrelated normalization uncertainties of the two detectors. The energy scale uncertainty is taken into account through parameters  $g^N$  and

$g^F$  in the expression of  $T_i^A$  in equation 9.5. We assumed here a flat background distribution:

$$B_i^A = \alpha \sum_{j=1}^{N_{\text{bins}}} \frac{O_j^A}{N_{\text{bins}}} \quad (9.9)$$

The numerical minimization has been performed with the MINUIT package [Jam]. We now discuss all the relevant terms of Equation 9.9 in turn.

### 9.2.2 Absolute normalization error: $\sigma_{\text{abs}}$

We include a common overall normalization error for the event rate of the near and far detectors. This error accounts for the uncertainty on the  $\bar{\nu}_e$  flux of the reactor, the detection cross section, or any bias that could affect both detectors in the same way<sup>1</sup>. This error is of the order of a few percent; one has for instance 1.4 % in [Dec94], 2 % in [KAM02]. The overall normalization error has almost no impact on the sensitivity to an oscillation effect in the Double-CHOOZ experiment since two detectors will be used (see Figures 9.7 and 9.8). Nevertheless, we included an absolute normalization error  $\sigma_{\text{abs}} = 2 \%$  in the simulation.

### 9.2.3 Relative normalization error: $\sigma_{\text{rel}}$

We take into account an uncorrelated normalization uncertainty between the near and far detectors. This is the dominant experimental error for the Double-CHOOZ experiment. There are contributions from uncertainties on the detector design (fiducial volume, stability of the liquid scintillator, relative dead time measurement) and the uncertainties related to the  $\bar{\nu}_e$  event selection cuts (relative detector efficiency). According to the results presented in Chapter 8, we take the relative normalization error  $\sigma_{\text{rel}} = 0.6 \%$  as our default value.

### 9.2.4 Spectral shape error: $\sigma_{\text{shp}}$

To take into account the  $\bar{\nu}_e$  spectrum shape uncertainty, we introduce an error  $\sigma_{\text{shp}}$  on the theoretical prediction for each energy bin which we take to be fully uncorrelated between different energy bins. Since this error is induced by the physical uncertainty on the fission product beta decay spectra, it is fully correlated between the corresponding bins in the near and far detector. In the simulation we use the shape error value  $\sigma_{\text{shp}} = 2 \%$ , as measured in [BUG96].

### 9.2.5 Energy scale error: $\sigma_{\text{scl}}$

We take into account the energy scale calibration uncertainty by introducing a parameter  $g^A$  for each detector ( $A = N, F$ ), and replacing the observed energy  $E_{\text{obs}}$  by  $(1 + g^A)E_{\text{obs}}$ . We assume that the energy calibration is known with an error of  $\sigma_{\text{scl}} \sim 0.5 \%$ . We found that, as long as no detailed background simulation is performed on the data, this error can be neglected in first approximation for the sensitivity computations. This is understandable since the Double-CHOOZ experiment is mostly sensitive to the number of events integrated over the whole positron spectrum. Nevertheless, a careful study of this error is going on to better understand its influence on the discovery potential of Double-CHOOZ.

<sup>1</sup>For instance, a bias in the volume measurement affecting the two detectors is equivalent to an uncertainty in the reactor  $\bar{\nu}_e$  flux.

### 9.2.6 Individual core power fluctuation error: $\sigma_{\text{eff}}$

Since the Double-CHOOZ power station has two nuclear cores, we introduced an independent error of  $\sigma_{\text{eff}} = 0.5\%$  mimicking a thermal power fluctuation of each nuclear core. Indeed, depending on the exact location of the near detector site, the near and far detectors will not receive the same  $\bar{\nu}_e$  contribution from both cores. In that case, an independent fluctuation in the two cores could lead to a relative systematic error between the detectors. However, we found this error to be negligible and we do not consider it further.

### 9.2.7 Background subtraction error

We considered two different ways to introduce an error on the background subtraction procedure.

#### 9.2.7.1 Reactor $\bar{\nu}_e$ shape background: $\sigma_{\text{b2b}}$

This is modeled as an uncorrelated error  $\sigma_{\text{b2b}}$  in the background subtraction step. This error is bin-to-bin uncorrelated, uncorrelated between the near and far detectors, and proportional to the bin content (i.e. the background has the same shape as the positron spectrum). Typically we used values ranging from  $\sigma_{\text{b2b}} = 0.5\%$  to  $\sigma_{\text{b2b}} = 1.5\%$ .

#### 9.2.7.2 Flat background: $\sigma_{\text{bkg}}$

This background is closer in shape to the background of fast neutrons created in the rocks close to the detector. It was dominating in CHOOZ [CHO03], and is expected to play an important role in Double-CHOOZ as well (see Chapter 7). We assume that it amounts typically for  $R_N = 1\%$  &  $R_F = 1\%$  of the total  $\bar{\nu}_e$  signal. To be conservative we consider an error on those rates of  $\sigma_{\text{bkg}}^N = 100\%$  &  $\sigma_{\text{bkg}}^F = 100\%$ , in the near and far detectors. A careful study of the impact of the background on the sensitivity and on the discovery potential as well is going on.

## 9.3 Sensitivity in the case of no oscillations

We present our results for the current best fit value of the atmospheric mass splitting  $\Delta m_{23}^2 = 2.0_{-0.7}^{+1.0} \cdot 10^{-3} \text{ eV}^2$  [SK02a] as our default value. Nevertheless, we also used the recent analysis of the Super-Kamiokande data leading to  $\Delta m_{23}^2 = 2.4_{-0.5}^{+0.6} \cdot 10^{-3} \text{ eV}^2$  [SK04a], for completeness. We also assume that a forthcoming accelerator experiment will provide a precise measurement of  $\Delta m_{23}^2$ , with an error better than 20%:  $\sigma_{\Delta m^2} = 0.2 \cdot \Delta m^2$  prior to the Double-CHOOZ result [MIN01a, MIN01b]. Figure 9.1 displays the expected sensitivity of Double-CHOOZ in the case of no-oscillations, as a function of time. In this case we have a sensitivity of  $\sin^2(2\theta_{13}) < 0.045$  (90% C.L.) after one year of data taking, and  $\sin^2(2\theta_{13}) < 0.03$  after three years. The sensitivity dependence with respect to the atmospheric mass splitting  $\Delta m_{23}^2$  value is shown in Figure 9.3. Figure 9.4 displays the effect of  $\sigma_{\text{rel}}$  on the sensitivity of Double-CHOOZ in the  $(\sin^2(2\theta_{13}), \Delta m_{\text{atm}}^2)$  plane. The relative normalization influence on the  $\sin^2(2\theta_{13})$  limit as a function of the exposure time is shown in Figure 9.5.

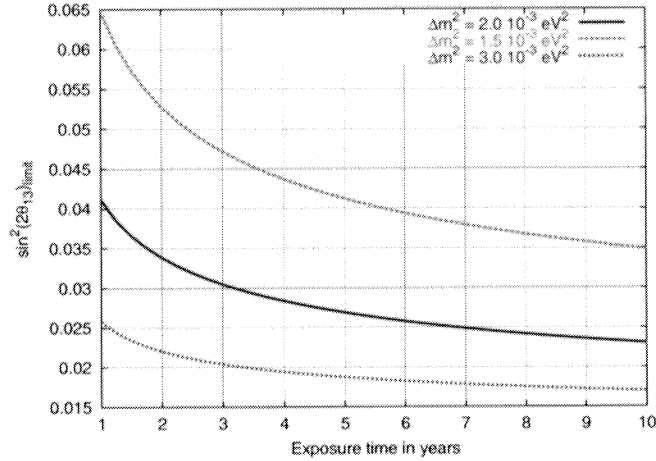


Figure 9.1: Evolution of  $\sin^2(2\theta_{13})$  sensitivity with the exposure time. The three curves shown here are for different values of  $\Delta m^2$  as shown in the legend.

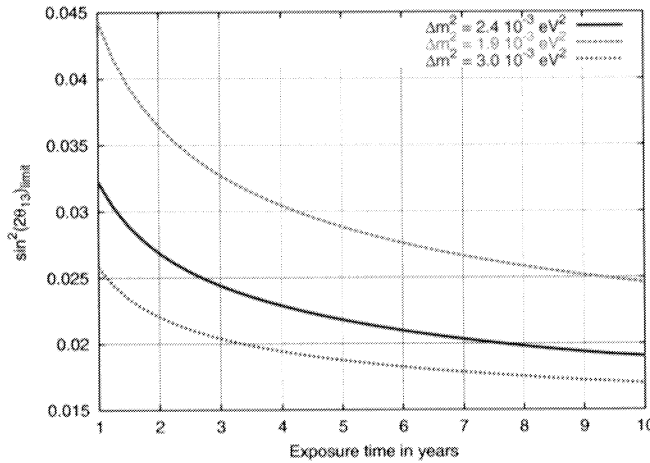


Figure 9.2: Evolution of  $\sin^2(2\theta_{13})$  sensitivity with the exposure time. The three curves shown here are for different values of  $\Delta m^2$  as shown in the legend. These values have been chosen from the second analysis (L/E) of the same Super-Kamiokande data [SK04a].

### 9.3.1 Comparison of Double-CHOOZ and the T2K sensitivities

We compute both the Double-CHOOZ and the T2K sensitivities, in the  $\sin^2(2\theta_{13})$ - $\delta$  plane, for three dates: January 2009, January 2011, and January 2015. We assume that the Double-CHOOZ experiment will start to take data with two detectors on January 2008, while the T2K experiment will start exactly two years later, on January 2010, with the nominal beam intensity (since the T2K neutrino line is expected to be completed within the year 2009, we assume that the accelerator commissioning will be finished by the end of 2009 [SK04b, SK04c]). For the computation of



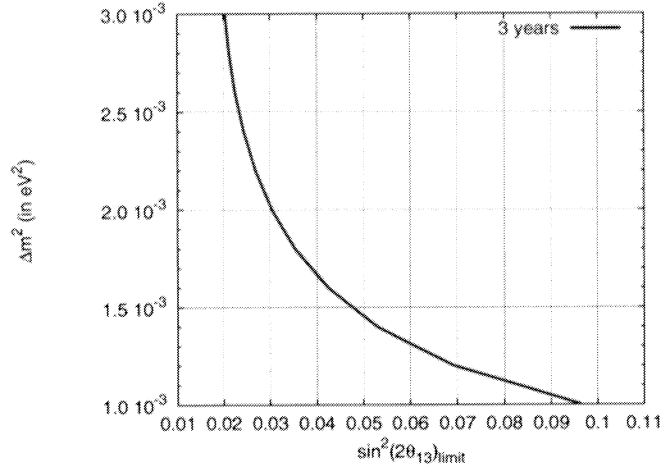


Figure 9.3: Double-CHOOZ sensitivity limit at 90 % C.L. (for 1 d.o.f).

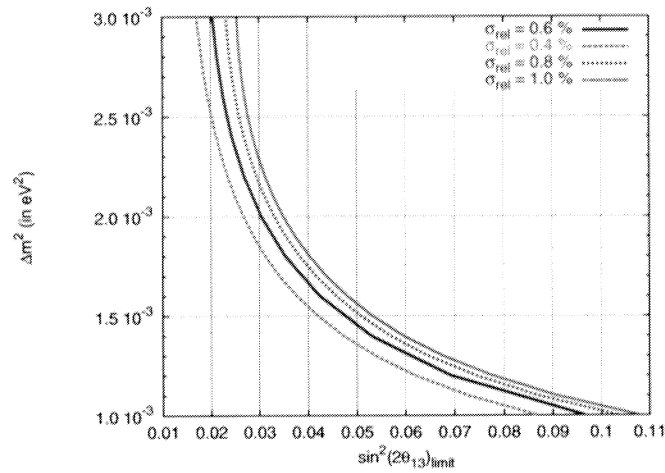


Figure 9.4: Influence of the relative normalization uncertainty on the  $\sin^2(2\theta_{13})$  limit in the  $(\sin^2(2\theta_{13}), \Delta m^2)$  plane in the case of no oscillations (for three years of operation).

the Double-CHOOZ sensitivity we assume here a relative normalization error of 0.6 % for both detectors. The correlated backgrounds considered here amount to 1.5 % of the signal for both the near and far detectors. Several background components of known shape have been included (proton recoil, accidental, spallation, see Chapter 7). An additional uncorrelated background component of 0.5 % is also considered here. All backgrounds are supposed to be known with a 50 % error. Details of the analysis procedure are given in [Hub02, Hub04]. For the simulation of the T2K experiment, the experimental parameters are taken from [T2K02, T2K03]. We used nominal 1 year and 5 year running times for T2K, and 1, 3, and 7 years for the reactor setup (with 20,000 events/year). We compute the two-dimensional allowed fit regions (i.e., the parameters on the axes are the fitted parameters, in the  $\sin^2(2\theta_{13})$ - $\delta$  plane) for three dates: January 2009, January 2011, and January 2015.

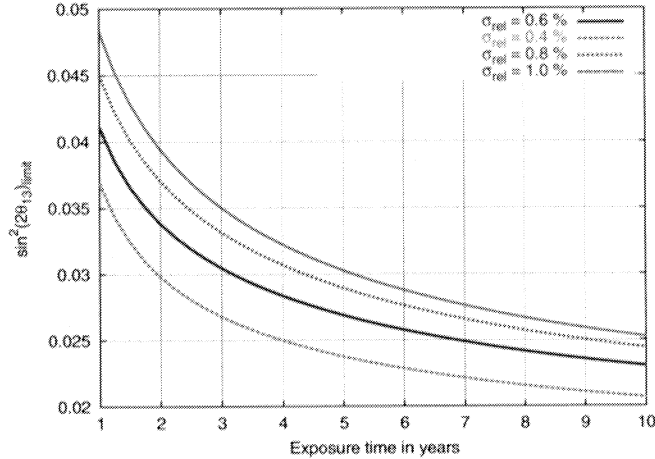


Figure 9.5: Influence of the relative normalization uncertainty on the  $\sin^2(2\theta_{13})$  limit as a function of the exposure time (in years) in the case of no oscillations.

The curves for T2K include all correlations and degeneracies and are obtained as projections of the fit manifolds onto the  $\sin^2(2\theta_{13})$ - $\delta$  plane [Hub02, Hub04].

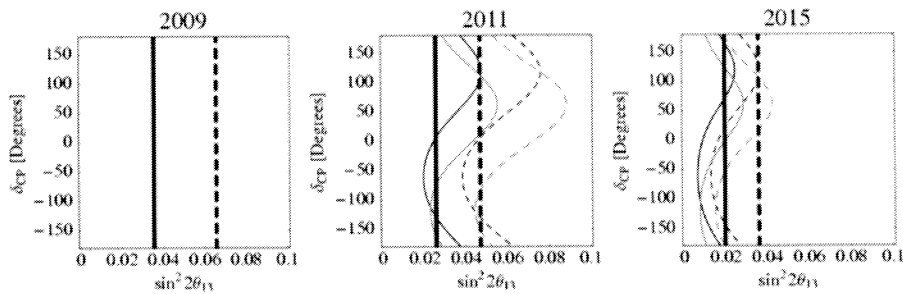


Figure 9.6: Limit at 90 % C.L. in the  $\sin^2(2\theta_{13})$ - $\delta$  plane for Double-CHOOZ and T2K [Hub02, Hub04]. The following oscillation parameters have been used:  $\Delta m_{31}^2 = 2 \cdot 10^{-3} \text{ eV}^2$ ,  $\Delta m_{21}^2 = 7 \cdot 10^{-5} \text{ eV}^2$ ,  $\sin^2(2\theta_{23}) = 1.0$ ,  $\sin^2(2\theta_{12}) = 0.8$ , and  $\sin^2(2\theta_{13}) = 0$ . We have considered 1 d.o.f for the analysis of the Double-CHOOZ experiment, but 2 d.o.f. for the analysis of T2K that is sensitive to both  $\sin^2(2\theta_{13})$  and  $\delta$  simultaneously. 90 % C.L. intervals are shown with solid lines, and  $3\sigma$  intervals are displayed with dashed lines. The thick curves describe the Double-CHOOZ setup, and the thin curves the T2K experiment, with black curves for best-fit solution, and gray curves for the  $\text{sgn}(\Delta m_{31}^2)$ -degeneracy.

## 9.4 Discovery potential

### 9.4.1 Impact of the errors on the discovery potential

The  $3\sigma$  discovery potential of Double-CHOOZ is displayed on Figures 9.7 and 9.8, for respectively  $\Delta m_{31}^2 = 2.0$  and  $2.4 \cdot 10^{-3} \text{ eV}^2$ . In the first case, a non-vanishing

value of  $\sin^2(2\theta_{13}) = 0.05$  could be detected at  $3\sigma$  after three years of data taking. For the second case, this value becomes  $\sin^2(2\theta_{13}) = 0.04$ .

#### 9.4.2 Comparison of Double-CHOOZ and the T2K discovery potential

The computation is done as presented in Section 9.3.1, for both the Double-CHOOZ and the T2K experiments taken at three dates: January 2009, January 2011, and January 2015. To investigate the discovery potential of both experiments, we used three benchmark values  $\sin^2(2\theta_{13}) = 0.14, 0.08, 0.04$ . Results are presented respectively in the  $\sin^2(2\theta_{13})$ - $\delta$  plan in Figures 9.9, 9.10 and 9.11.

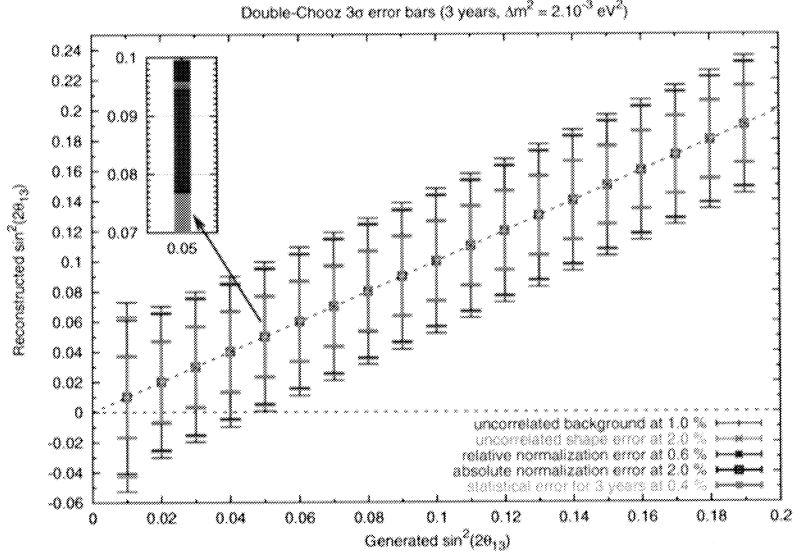


Figure 9.7: Statistical and systematic errors contributions to  $\sin^2(2\theta_{13})$  measurement. We assumed here SK-I analysis best fit value  $\Delta m_{31}^2 = 2.0 \cdot 10^{-3} \text{ eV}^2$ , 3 years of data taking for Double-CHOOZ with 64 % (expecting around 58,000 events in the case of no oscillations) of efficiency in the far detector and 32 % in the near one. We also set the systematic errors to the standard ones: the absolute normalization to 2 %, the relative to 0.6 %, the shape uncertainty to 1 % and the background to 1 %. The different error intervals are plotted at with a  $3\sigma$  confidence level. We see here that the discovery potential limit of Double-CHOOZ to detect a non-vanishing value of  $\sin^2(2\theta_{13})$  is around 0.05. We also see here that struggling harder than the level of 0.6 % on the relative normalization could lower this discovery potential limit.

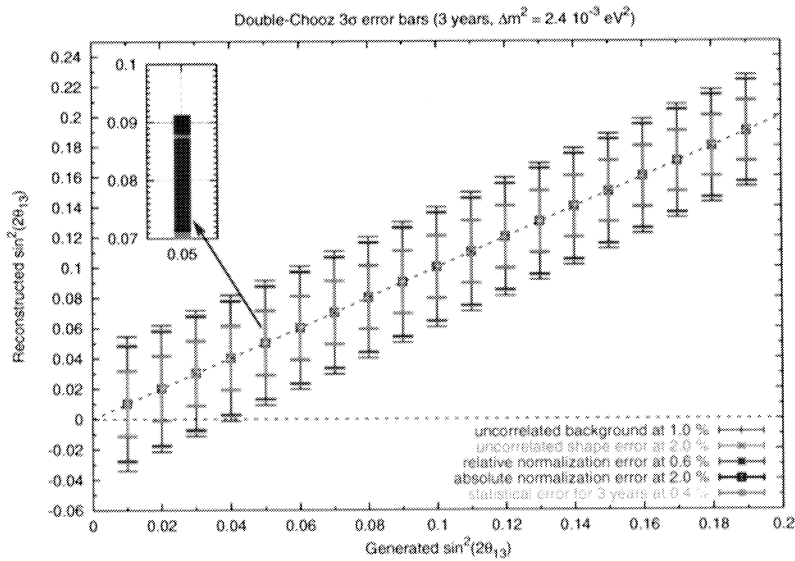


Figure 9.8: Same as Figure 9.7 but for  $\Delta m_{31}^2 = 2.4 \cdot 10^{-3} \text{ eV}^2$ .

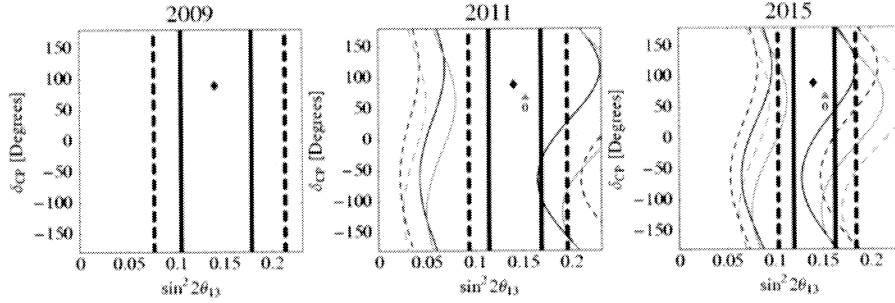


Figure 9.9: Measurement of  $\sin^2(2\theta_{13})$  and  $\delta$  with Double-CHOOZ and T2K [Hub02, Hub04]. The following oscillation parameters have been used:  $\Delta m_{31}^2 = 2 \cdot 10^{-3} \text{ eV}^2$ ,  $\Delta m_{21}^2 = 7 \cdot 10^{-5} \text{ eV}^2$ ,  $\sin^2(2\theta_{23}) = 1.0$ ,  $\sin^2(2\theta_{12}) = 0.8$ . The  $\theta_{13}$  mixing angle was generated as  $\sin^2(2\theta_{13}) = 0.14$  and the CP- $\delta$  phase has been fixed at  $\delta = \pi/2$ . We considered 1 d.o.f. for the analysis of the Double-CHOOZ experiment, but 2 d.o.f. for the analysis of T2K that is sensitive to both  $\sin^2(2\theta_{13})$  &  $\delta$  simultaneously. 90 % C.L. interval are shown with solid lines, and  $3\sigma$  intervals are displayed with dashed lines. The thick curves describe the Double-CHOOZ setup, and the thin curves the T2K experiment, with black curves for best-fit solution, and gray curves for the  $\text{sgn}(\Delta m_{31}^2)$ -degeneracy. The minimum  $\chi^2$  is drawn at marked points.

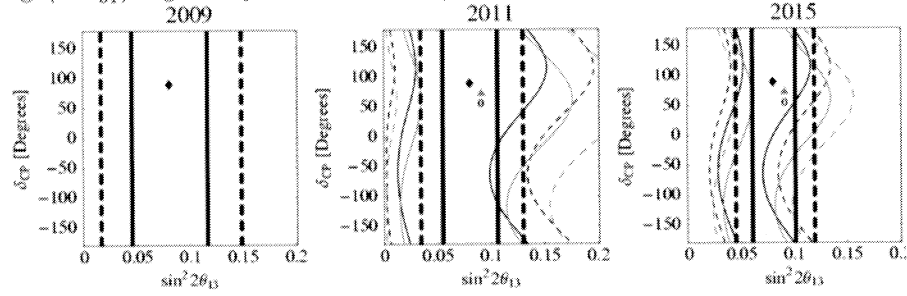


Figure 9.10: Same as Figure 9.9, but for the  $\theta_{13}$  mixing angle was generated at  $\sin^2(2\theta_{13}) = 0.08$ .

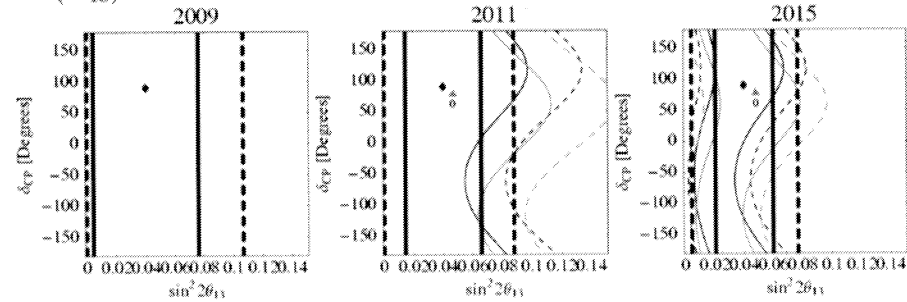


Figure 9.11: Same as Figure 9.9, but for the  $\theta_{13}$  mixing angle was generated at  $\sin^2(2\theta_{13}) = 0.04$ .



## Appendix A

# $\bar{\nu}_e$ and safeguards applications

The International Atomic Energy Agency (IAEA) is the United Nations agency in charge of the development of peaceful use of atomic energy [IAEA]. In particular IAEA is the verification authority of the Treaty on the Non-Proliferation of Nuclear Weapons (NPT). To do that job inspections of civil nuclear installations and related facilities under safeguards agreements are made in more than 140 states. IAEA use many different tools for these verifications, like neutron monitors, gamma spectroscopy, but also bookkeeping of the isotopic composition at the fuel element level before and after their use in the nuclear power station. In particular it verifies that weapon-origin and other fissile materials that Russia and USA have released from their defense programs are used for civil applications.

The existence of a  $\bar{\nu}_e$  signal sensitive to the power and isotopic composition of a reactor core could provide a mean to address certain safeguards applications. Thus the IAEA very recently asked member states to make a feasibility study to determine whether antineutrino detection methods might provide practical safeguards tools for selected applications. If this method proves to be useful, IAEA has the power to decide that any new nuclear power plant to be built has to include an  $\bar{\nu}_e$  monitor.

The high penetration power of antineutrinos and the detection capability might provide a mean to make "remote" and non-intrusive measurements of plutonium content in reactors and in large inventories of spent fuel. The antineutrino flux and energy spectrum depend upon the thermal power and the fissile isotopic composition of the reactor fuel. Because the antineutrino signal from the reactor decreases as the square of the distance from the reactor to the detector the "remote" measurement is really only practical at distances of a few tens of meters if one is constrained to "small" detectors of the order of few cubic meters in size. Based on predicted and observed  $\beta$  spectra, the number of  $\bar{\nu}_e$  per fission from  $^{239}\text{Pu}$  is known to be less than the number from  $^{235}\text{U}$ . This variation has been directly measured in reactor antineutrino experiments. This may offer a mean to monitor changes in the relative amounts of  $^{235}\text{U}$  and  $^{239}\text{Pu}$  in the core and in freshly discharged spent fuel. If made in conjunction with accurate independent measurements of the thermal power (including the ambient reactor temperature and the flow rate of cooling water), antineutrino measurements might provide an estimate of the isotopic composition of the core, in particular plutonium inventories. The shape of the antineutrino spectrum can provide additional information about core fissile isotopic composition.

In order to determine the feasibility of antineutrino detection for safeguards ap-

	$^{235}\text{U}$	$^{239}\text{Pu}$	$^{241}\text{Pu}$
$\bar{\nu}_e/\text{fission}$	6.2	5.6	6.4
End point (MeV)	9.0	7.4	9.3

Table A.1: Number of  $\bar{\nu}_e$  emitted per fission and end points of U and Pu fissile isotopes.

plications, a series of scenarios involving antineutrino detectors should be defined, both for reactors and for spent fuel inventories. The effectiveness, sensitivity, and possible vulnerabilities of antineutrino detection should be examined for these scenarios. For the IAEA, the proposed feasibility study should seek to establish or refute the utility of antineutrino detection methods as a new safeguards tool, and serve as a guide for future efforts. Additional lab tests and theoretical calculations should also be performed to more precisely estimate the underlying  $\beta$  spectra of plutonium and uranium fission products, especially at low energies, corresponding to the most energetic antineutrinos.

The appropriate starting point for this scenario is a representative PWR. For this reactor type, simulations of the evolution of the antineutrino flux and spectrum over time should be provided, and the required precision of the antineutrino detector and independent power measurements should be estimated. In that respect the measurement performed by the Double-CHOOZ experiment with its near detector, as it is explained in the proposal, will constitute the most precise determination of the antineutrinos emitted by a PWR. In particular, the follow-up of the spectrum and rate after refueling with fresh  $^{235}\text{U}$ , would allow a precision study of the correlation between plutonium content and the measured spectrum. If it is possible in addition to have a detailed follow-up of the evolution of the fuel burn-up, by the use of fission chambers, the data gathered by these experiments will constitute an excellent experimental basis for the above feasibility studies of potential monitoring and for bench-marking fuel management codes. This measurement will help to meet another important point of the IAEA concern, linked to the verification of provisions of the US-Russian Plutonium Management and Disposition Agreement (PMDA). This agreement concerns MOX fuel made using weapon origin plutonium.

Verifying core burn up while the reactors are operating would provide a mean to determine whether or not the disposition criteria have been met. From the present knowledge of the antineutrino spectrum emitted by the fission products, we see that the most energetic part offers the best possibility to disentangle fission from  $^{235}\text{U}$  and  $^{239}\text{Pu}$ . Unfortunately the present uncertainty in that region of energy is rather large, due to the difficulties of measuring the corresponding low energy  $\beta^-$ .

Thus, in relation to this feasibility studies, new measurements of the  $\beta$  spectrum for the various fissile elements are mandatory. A group of nuclear physicists has developed tools, in the frame of MiniINCA collaboration [Inca], which can be modified to perform these measurements at ILL. Needless to say that a more precise knowledge of the antineutrinos emitted in the reactor core would also benefit the physics measurements of  $\theta_{13}$ . The overall IAEA feasibility studies are larger than the topics briefly described above. It is also of interest to study other present reactor types, like BWRs, FBRs, and possibly CANDU reactors. Future reactors (e.g., PBMRs, Gen IV reactors, accelerator-driven sub-critical assemblies for transmutation), especially reactors using carbide, nitride, metal or molten salt fuels must also be considered. IAEA seeks also to the possibility of monitoring large spent-



fuel elements. For this application, the likelihood is that antineutrino detectors could only make measurements on large quantities of  $\beta$  emitters, e.g., several cores worth of spent fuel. In the time of the experiment the discharge of parts of the core will happen and the Double-CHOOZ experiment will quantify the sensitivity of such monitoring. More generally the techniques developed for the detection of antineutrinos could be applied for the monitoring of nuclear activities at the level of a country. For example a KamLAND type detector [KAM02] deeply submerged off the coast of the country, would offer the sensitivity to detect a new underground reactor located at several hundreds of kilometers. In that respect, the progress in term of detecting medias (Gd doped liquid scintillators) would be greatly helpful.



## Appendix B

# Nuclear reactor $\beta$ spectra

New measurements of the  $\beta$  spectrum for various fissile elements present in a nuclear reactor will be very important for the Double-CHOOZ experiment to understand the physics at the near detector. Of course, it is less important for the oscillation analysis, since the absolute normalization error on the  $\bar{\nu}_e$  flux is absorbed if two detectors are used simultaneously at different baselines. These new integral measurements deal with a complete characterization of the  $\beta$  spectrum produce in the fuel element by taking into account the evolution of the fuel. This information is important to characterize the antineutrino spectra at the Double-CHOOZ experiment but is also unavoidable for the feasibility studies of using antineutrino detection methods as a new safeguards tool.

In the frame of the Mini-INCA project [Inca], the group has developed a set of experimental tools to perform quasi online  $\alpha$ - and  $\gamma$ -spectroscopy analyzes on irradiated isotopes and to monitor online the neutron flux in the high flux reactor of the ILL reactor. It has also developed competences on the Monte-Carlo simulations of complex systems and in particular nuclear reactors. These competences will be used to provide to the community a set of integral  $\beta$  energy spectra relevant for the Double-CHOOZ experiment and for safeguards studies and to understand and monitor all the fluctuations in the antineutrino spectra originated from the reactor source.

### B.1 New $\beta$ energy spectra measurements at ILL

The  $\alpha$  and  $\gamma$  spectroscopy station, connected to an irradiation channel of the ILL reactor, offer the possibility to perform irradiations in a quasi thermal neutron flux up to 20 times the nominal value in a PWR. This irradiation can be followed by measurements and repeated as many time as needed. It offers then the unique possibility to characterize the evolution of the beta spectrum as a function of the irradiation time and the irradiation cooling. The expected modification of the  $\beta$  spectrum as a function of the irradiation time is connected to the transmutation induced by neutron capture of the fissile and fission fragment elements. It is thus related to the natural evolution of the spent-fuel in the reactor. The modification of the  $\beta$  spectrum as a function of the cooling time is connected to the decay chain of the fission products and is then a mean to select the emitted fragments by their time of live. This information is important because long-lived fission fragments accumulate in the core and after few days mainly contribute to the low energy part of the antineutrino-spectra. We propose to modify the spectroscopy station by adding a large dynamic  $\beta^-$  spectrometer and to measure the  $\beta$  spectra for  $^{235}\text{U}$ ,  $^{239}\text{Pu}$ ,  $^{241}\text{Pu}$  and  $^{243}\text{Cm}$  for different irradiation and cooling times. Due to the

mechanical transfer of the sample from the irradiation spot to the measurement station an irreducible delay time of 30 mn is imposed leading to the loss of short-live fragments. To characterize the  $\beta$  prompt emissions online measurements will be done on a neutron guide where cold neutrons are available.

## **B.2 Reactivity monitoring**

Micro-fission chambers developed for high neutron fluxes are used in core in the ILL reactor. They provide very precise neutron flux measurements and allow to monitor in line the reactivity fluctuations of the core. Due to their small dimensions (4 mm in diameter and 4 cm in length) and the low fissile deposit, they should allow to measure very precisely the gravity center of the core, with a negligible flux perturbation, if placed out core of the Chooz reactor.

## **B.3 Double-CHOOZ reactor core simulation and follow-up**

By the mean of Monte-Carlo and deterministic codes developed for neutron flux calculation and evolution at ILL and for various type of transmutation scenario, we propose to model the complete history of Chooz reactor core to study the sensitivity of the neutrino spectrum to the isotopic composition and fuel burn up.

## Appendix C

# Some numbers from the CHOOZ experiment

The CHOOZ experiment [CHO98, CHO99, CHO00, CHO03] was located close to the CHOOZ nuclear power plant, in the North of France, 10 km from the Belgian border. The power plant consists of two twin pressurized water reactors (PWR), the first of a series of the newly developed N4 PWR generation in France [CEA01]. The thermal power of each reactor is 4.25 GW<sub>e</sub> (1.3 GW<sub>e</sub>). These reactors started respectively in May and August 1997, just after the start of the data taking of the CHOOZ detector (April 1997). This opportunity allowed a measurement of the reactor-off background, and a separation of individual reactors contributions.

The detector was located in an underground laboratory about 1 km from the neutrino source. The 300 m.w.e. rock overburden reduced the external cosmic ray muon flux, by a factor of about 300, to a value of 0.4 m<sup>-2</sup>s<sup>-1</sup>. This was the main criterion to select this site. Indeed, the previous experiment at the Bugey reactor power plant [BUG96] showed the requirement of reducing by two orders of magnitude the flux of fast neutrons produced by muon-induced nuclear spallations in the material surrounding the detector. The neutron flux was measured at energies greater than 8 MeV and found to be about 1/day, in good agreement with the prediction.

The detector envelope consisted of a cylindrical steel vessel, 5.5 m diameter and 5.5 m height. The vessel was placed in a pit (7 m diameter and 7 m deep), and was surrounded by 75 cm of low activity sand. It was composed of three concentric regions, from inside to outside:

- a central 5 tons target in a transparent Plexiglas container filled with a 0.09 % Gd-loaded scintillator
- an intermediate 70 cm thick region, filled with non-loaded scintillator and used to protect the target from PMT radioactivity and to contain the gammas from neutron capture on Gd. These 2 regions were viewed by 192 PMTs
- an outer veto, filled with the same scintillator.

The scintillator showed a degradation of the transparency over time, which resulted in a decrease of the light yield (live time around 250 days). The event position was reconstructed by fitting the charge balance, with a typical precision of 10 cm for the positron and 20 cm for the neutron. Source and laser calibrations found that due to the small size of the detector the time reconstruction was less precise than expected. The reconstruction became more difficult when the event was located

near the PMTs, due to the  $1/r^2$  divergence of the light collected (see Figure 31 of [CHO03]).

The final event selection used the following cuts:

- positron energy smaller than 8 MeV (only 0.05 % of the positrons have a higher energy)
- neutron energy between 6 and 12 MeV
- distance from the PMT support structure larger than 30 cm for both positron and neutron
- distance between positron and neutron smaller than 100 cm
- low particles multiplicity: when a third particle is detected in the time window between the positron and neutron candidates, a complicated cut must be applied (see 8.7 of [CHO03]).

The neutron capture on Gd is identified by a 6 MeV cut on the total energy emitted. This cut induce a systematic error of 0.4 %, due to the poor knowledge of the emission spectrum of the gammas released after the neutron capture.

The scintillating buffer around the target was important enough to reduce the gammas escape. This cut was calibrated with a neutron source. The 3 cuts on the distances were rather difficult to calibrate, due to the the reconstruction problems described above. This created a tail of badly reconstructed events, which was very difficult to simulate (0.4 % systematic error on the positron-neutron distance cut). The positron threshold was carefully calibrated, as shown in Figure 39 of [CHO03]. The value of the threshold depends upon the position of the event, due to the variation of solid angle and to the shadow of some mechanical pieces such as the neck of the detector (0.8 % systematic error). The time cut relied on Monte-Carlo simulation. The corresponding systematic error was estimated to be 0.4 %. The final result was given as the ratio of the number of measured events versus the number of expected events, averaged on the energy spectrum. It was found to be:

$$R = 1.0 \pm 2.8 \% \text{ (stat)} \pm 2.7 \% \text{ (sys)}.$$

Two components were identified in the background:

- Correlated events: which had a flat distribution for energies greater than 8 MeV, and were due to the recoil protons from fast spallation neutrons. It was extrapolated to 1 event/day.
- Accidental events: which were obtained from the measure of the singles rates.

The total noise was measured during the reactor-off, and by extrapolating the signal versus power straight line (see Figure 49 of [CHO03]). It is in good agreement with the sum of the correlated and accidental components. These numbers have to be compared to a signal of 26 events/day at full reactor power. The systematic error was due mainly to the reactor uncertainties (2 %), the detector efficiency (1.5 %), and to the normalisation of the detector dominated by the error on the proton number from the H/C ratio in the liquid (0.8 %). The resulting exclusion plot is shown in Figure 58 of [CHO03]. The corresponding limit on  $\sin^2(2\theta_{13})$  is 0.14 for  $\Delta m^2 = 2.6 \cdot 10^{-3} \text{ eV}^2$ , and 0.2 for  $\Delta m^2 = 2.0 \cdot 10^{-3} \text{ eV}^2$ . This limit disappears for  $\Delta m^2 < 0.8 \cdot 10^{-3} \text{ eV}^2$ , due to the  $\sim 1$  km distance between the cores and the CHOOZ detector.

## Acknowledgments

Électricité de France (E.D.F.) is contributing to this project and studying the possibility of the near detector laboratory construction. The local authorities (Mairie de Chooz and Conseil général des Ardennes) have been supporting this project. Special thanks are due to F. Bobisut and B. Vallage for their very careful reviews of the experiment. Warm thanks are due to B. Svodoba and our american colleagues for fruitful discussions on the experimental issues. We thank C. Bemporad, J. Bouchez, C. Cavata, Y. Déclais, M. Froissart, J. Mallet, and S. Petcov for very useful discussions on the Double-CHOOZ experiment and neutrino physics. Finally, we would like to acknowledge the reactor working group members for the high quality LENE workshops, and M. Goodman for editing the useful Reactor Neutrino White Paper.

# List of Tables

2.1	Typical fuel composition of a PWR reactor . . . . .	17
2.2	Comparison of the sensitivity of reactor and accelerator based future neutrino experiments sensitive to $\theta_{13}$ . . . . .	21
3.1	Overburden required for the near detector . . . . .	25
3.2	Systematic errors in CHOOZ and Double-CHOOZ goals . . . . .	29
4.1	Summary the expected trigger rates for neutrino like events at CHOOZ-near . . . . .	43
5.1	Overview of liquid inventory for a single detector . . . . .	45
6.1	Techniques available to calibrate the Double-CHOOZ experiment . . . . .	51
7.1	Upper limits on U, Th and K concentrations in the liquid scintillator and acrylic vessel . . . . .	58
7.2	Estimated neutron rate in the active detector region due to through going cosmic muons. . . . .	59
7.3	Estimated neutron rate in the target region due to stopped negative muons . . . . .	59
7.4	Radioactive isotopes induced by muons in liquid scintillator targets at the CHOOZ near and far detectors. . . . .	62
7.5	Limits on the estimated neutron rate and the correlated background rate due to fast neutrons . . . . .	63
7.6	Example of estimated accidental event rates for different shielding depths. . . . .	63
8.1	Overview of the systematic errors of the CHOOZ and Double-CHOOZ experiment. . . . .	65
8.2	Summary of the neutrino selection cut uncertainties . . . . .	71
8.3	Summary of systematic errors that cancel or are significantly decreased in Double-CHOOZ . . . . .	71
8.4	Systematic errors that can be achieved without improvement of the CHOOZ published systematic uncertainties . . . . .	72
9.1	Chooz power station main features . . . . .	73
9.2	Detector parameters used in the simulation . . . . .	74
A.1	Number of $\bar{\nu}_e$ emitted per fission and end points of U and Pu fissile isotopes. . . . .	A-86



# List of Figures

1.1	Solar and atmospheric allowed regions from the global oscillation analysis . . . . .	12
2.1	$\bar{\nu}_e$ spectra of the four dominant fissioning isotopes . . . . .	18
2.2	Percentage of fissions of the main fissile elements during a fuel cycle . . . . .	19
3.1	Overview of the experiment site . . . . .	24
3.2	Map of the experiment site . . . . .	25
3.3	Picture of the CHOOZ-far detector site . . . . .	26
3.4	CHOOZ-far detector . . . . .	27
3.5	CHOOZ-near detector . . . . .	28
3.6	Positron spectrum expected in both near and far detectors . . . . .	30
3.7	Luminosity scaling of the Double-CHOOZ $\sin^2(2\theta_{13})$ sensitivity at the 90 % C.L. . . . .	31
3.8	Ratio of the expected number of $\bar{\nu}_e$ events in the far and near detector . . . . .	32
3.9	Ratio of the expected number of $\bar{\nu}_e$ events in the far and near detector: shape information . . . . .	32
4.1	Dimensions of the CHOOZ-far detector . . . . .	34
4.2	Sketch of the two acrylic vessels containing the Gd doped and undoped scintillators . . . . .	35
4.3	Preliminary evaluation of the stress applied on an empty acrylic cylinder suspended with three kevlar ropes . . . . .	35
4.4	Surface of PMTs mounted on the support structure . . . . .	37
4.5	Emission spectrum of the bis-MSB wavelength shifter . . . . .	39
4.6	Quantum efficiency of the PMT photocathode . . . . .	40
4.7	Absorption spectrum of the bis-MSB wavelength shifter . . . . .	40
4.8	Spectrum of the photons as they arrive at the PMT surface . . . . .	41
4.9	Light collection for different reflectivity coefficients of the PMT support structure . . . . .	42
5.1	Scintillation light yield of 80 % dodecane 20 % PXE 0.1 % Gd beta-diketone LS with varying PPO concentration . . . . .	47
5.2	Scintillation light yield of PXE/dodecane mixture with varying dodecane concentration . . . . .	48
5.3	Spectral attenuation length of Gd-acac (1 g/l) from an optimized synthesis compared with a commercial purchased product . . . . .	49
5.4	Absorption spectra of carboxylate Gd LS prior and after temperature test . . . . .	50
6.1	A possible scenario for a calibration source deployment system adapted from the SNO experiment calibration system. . . . .	55
7.1	Relevant branching ratios for the decay of the $^8\text{He}$ isotope. . . . .	60

7.2	Relevant branching ratios for the decay of the ${}^9\text{Li}$ isotope. . . . .	61
8.1	Simulation of the positron energy spectrum measured with the Double-CHOOZ detector . . . . .	68
8.2	Simulation of the neutron energy spectrum measured with the Double-CHOOZ detector . . . . .	69
8.3	Neutron delay distribution measured with the Am/Be source at the detector centre in the CHOOZ detector . . . . .	70
9.1	Evolution of $\sin^2(2\theta_{13})$ sensitivity with the exposure time (with $\Delta m^2$ interval taken from the oscillation analysis of Super-Kamiokande data in July 2003) . . . . .	78
9.2	Evolution of $\sin^2(2\theta_{13})$ sensitivity with the exposure time (with $\Delta m^2$ 90 % C.L. interval taken from the second analysis (L/E) of the same Super-Kamiokande data . . . . .	78
9.3	Double-CHOOZ sensitivity limit at 90 % C.L. (for 1 d.o.f). . . . .	79
9.4	Influence of the relative normalization uncertainty on the $\sin^2(2\theta_{13})$ limit in the $(\sin^2(2\theta_{13}), \Delta m^2)$ plane in the case of no oscillations . . . . .	79
9.5	Influence of the relative normalization uncertainty on the $\sin^2(2\theta_{13})$ limit as a function of the exposure time in the case of no oscillations. . . . .	80
9.6	Limit at 90 % C.L. in the $\sin^2(2\theta_{13})$ - $\delta$ plane for Double-CHOOZ and T2K . . . . .	80
9.7	Statistical and systematic errors contributions to $\sin^2(2\theta_{13})$ measurement ( $\Delta m_{31}^2 = 2.0 \cdot 10^{-3} \text{ eV}^2$ ) . . . . .	82
9.8	Statistical and systematic errors contributions to $\sin^2(2\theta_{13})$ measurement ( $\Delta m_{31}^2 = 2.4 \cdot 10^{-3} \text{ eV}^2$ ) . . . . .	82
9.9	Measurement of $\sin^2(2\theta_{13})$ and $\delta$ with Double-CHOOZ and T2K experiments ( $\sin^2(2\theta_{13}) = 0.14$ ) . . . . .	83
9.10	Measurement of $\sin^2(2\theta_{13})$ and $\delta$ with Double-CHOOZ and T2K experiments ( $\sin^2(2\theta_{13}) = 0.08$ ) . . . . .	83
9.11	Measurement of $\sin^2(2\theta_{13})$ and $\delta$ with Double-CHOOZ and T2K experiments ( $\sin^2(2\theta_{13}) = 0.04$ ) . . . . .	83

- [Jar85] C. Jarlskog, Phys. Rev. Lett. 55, 10 (1985)
- [KAM02] K. Eguchi *et al.*, (KamLAND Collaboration), Phys. Rev. Lett. 90, 021802 (2003).
- [Kla82] H. V. Klapdor and J. Metzinger, Phys. Rev. Lett. 48, 127 (1982).
- [LEN99] LENS Collaboration, Letter of Intent to the LNGS (1999).
- [LP00] "Light propagation in a large volume liquid detector.", NIM A 440, 360-371 (2000).
- [LVD99] A. Dementyev *et al.*, Nucl. Phys. **B** (Proc. Suppl.), 70 486 (1999).
- [LSN98] C. Athanassopoulos *et al.*, Phys. Rev. Lett. 81, 1774 (1998).
- [MAC98] M. Ambrosio *et al.* (MACRO Collaboration), Phys. Lett. B434, 451 (1998).
- [Mak62] Z. Maki, M. Nagakawa and S. Sakata, Prog. Part. Nucl. Phys. 28, 870 (1962).
- [Mal03] M. Maltoni, T. Schwetz, M.A. Tortola and J.W.F. Valle, Phys. Rev. D68, 113010 (2003).
- [MIN01a] V. Paolone (MINOS Collaboration), Nucl. Phys. Proc. Suppl. 100, 197 (2001).
- [MIN01b] M. Diwan *et al.* (MINOS Collaboration), Tech. Rep. NuMi-L-714 (2001).
- [Min01] H. Minakata and H. Nunokawa, JHEP 10, 001 (2001).
- [Min02] H. Minakata, H. Sugiyama, O. Yasuda, K. Inoue and F. Suekane, hep-ph/0211111 (2002)
- [Mot04] D. Motta, "Feasibility Analysis and Prototype Measurements of a Novel Approach for the Real-Time Spectroscopy of Low Energy Solar Neutrinos". Faculties for the Natural Sciences and for Mathematics of the Ruperto-Carola University of Heidelberg, Germany (2004).
- [MPI03a] C. Buck, F.X. Hartmann, D. Motta, S. Schönert, U. Schwan, "Metal beta-diketone scintillators." Presentation at the Workshop on Future Low Energy Neutrino Experiments, Technical University Munich, Munich, 9-11 October (2003).
- [MPI03b] C. Buck, F.X. Hartmann, S. Schönert, U. Schwan, "Development of an optically pure In beta-diketoneate for the scintillator of an  $^{115}\text{In}$ -loaded solar neutrino detector." Journal of Radioanalytical and Nuclear Chemistry 258(2) 255-264 (2003).
- [MPI03c] F.X. Hartmann, "Low Level Scintillators and Gadolinium.", Presentation at the Workshop on Future Low Energy Neutrino Experiments, Technical University Munich, Munich, 9-11 October (2003).
- [MPI04a] C. Buck, F.X. Hartmann, T. Lasserre, D. Motta, S. Schönert U. Schwan, "Luminescent properties of a new In-based liquid scintillator system." Journal of Luminescence, 106(1) 57-67 (2004).
- [MPI04b] F.X. Hartmann *et al.* "Single carboxylate Yb, Gd and In scintillators and pH control stability model". Prepared for submission to NIM (2004).

- [NIM01] Nuclear Instruments and Methods in Physics Research, A449, 172-207 (2000).
- [NUM02] D. Ayres *et al.*, hep-ex/0210005 (2002).
- [OPE03] (OPERA Collaboration), International Workshop on "Neutrino Oscillations in Venice", Venice, December 3-5 (2003).
- [PDG00] Particle Data Group, D.E. Groom *et al.*, Eur. Phys. J. C15 (2000).
- [Pet01] S.T. Petcov and M. Piai, hep-ph/0112074 (2001).
- [Pet02] S. T. Petcov and M. Piai, Phys. Lett. B533, 94 (2002).
- [Pon58] B. Pontecorvo, Zh. Eksp. Teor. Fiz. 33, 549 (1957), and Zh. Eksp. Teor. Fiz. 34, 247 (1958).
- [PV01] F. Boehm *et al.* (Palo Verde Collaboration), Phys. Rev. D64, 112001 (2001).
- [PV97] (Palo Verde Collaboration) NIM A 385, 85-90 (1997).
- [SOU97] W.W.M. Allison *et al.* Phys. Lett. B391, 491 (1997).
- [SK98] Y. Fukuda *et al.* (Super-Kamiokande Collaboration), Phys. Rev. Lett. 81, 1562 (1998).
- [Ron01] F. Ronga, Nucl. Phys. Proc. Suppl. 100, 113 (2001).
- [RWP04] K. Anderson *et al.*, "White Paper For a new Reactor Neutrino Experiment", hep-ex/0402041 (2004).
- [SAG02] J. N. Abdurashitov *et al.* (SAGE Collaboration), J. Exp. Theor. Phys. 95, 181 (2002).
- [Sch85] K Schreckenbach *et al.*, Phys. Lett. B160, 325 (1985).
- [Sch99] S. Schönert, Nucl. Phys. B (Proc. Suppl.) 70, 195 (1999).
- [Sch03] S. Schönert, T. Lasserre and L. Oberauer, Astropart. Phys. 18, 565 (2003).
- [SK02a] M. Shiozawa (Super-Kamiokande Collaboration), Talk given at Neutrino 2002 conference, Munich, Germany. <http://neutrino2002.ph.tum.de>.
- [SK02b] S. Fukuda *et al.* (Super-Kamiokande Collaboration), Phys. Lett. B539, 179 (2002).
- [SK04a] M. Ishitsuka, Ph.D. Thesis, University of Tokyo (2004).
- [SK04b] T. Kobayashi (KEK), Talk given at the international workshop NOON04, Tokyo, Japan (2004).
- [SK04c] Y. Itow (ICRR), Talk given at the international workshop NOON04, Tokyo, Japan (2004).
- [SNO02] Q. R. Ahmad *et al.* (SNO Collaboration), Phys. Rev. Lett. 89, 011301 (2002).
- [T2K02] Nucl. Phys. B645, 3-48, (2002).
- [T2K03] Nucl. Phys. B654, 3-29 (2003).
- [Vog81] P. Vogel *et al.*, Phys. Rev. C24, 1543 (1981).
- [3M] <http://www.3m.com/>.

# Bibliography

- [Bar02] V. Barger, D. Marfatia and D. Whisnant, Phys. Rev. D65, 073023 (2002).
- [Bil01] S.M. Bilenky, D. Nicolo and S.T. Petcov, hep-ph/0112216 (2001).
- [Birks] *"The Theory and Practice of Scintillation Counting."*, J.B. Birks.
- [Bor83] A.A. Borovoi *et al.*, Sov. J. Nucl. Phys. 37, 801 (1983).
- [BOO02] A. Bazarko (BooNE Collaboration), hep-ex/0210020 (2002).  
<http://www-boone.fnal.gov/publicpages/index.html>.
- [BOR04] Borexino Collaboration, *"A high-density and high-flashpoint organic liquid scintillator for applications in low-energy particle-astrophysics experiments."* Prepared for submission to NIM (2004).
- [Buc04] W. Buchmuller, P. Di Bari, M. Plumacher, hep-ph/0401240 (2004).
- [BUG96] B. Achkar *et al.*, Phys. Lett. B374, 243 (1996).
- [Bur01] J. Burguet-Castell, M. B. Gavela, J. J. Gomez-Cadenas, P. Hernandez and O. Mena, Nucl. Phys. B608, 301 (2001).
- [Cat04a] C. Cattadori, N. Danilov *et al.*, *"Formulation of an indium loaded scintillator based on indium extraction in trimethyl-benzene by means of C<sub>3</sub>-C<sub>5</sub> carboxylic acids, in presence of neutral organophosphorous compounds."* Submitted to Radiation Physics and Chemistry (2004).
- [Cat04b] C. Cattadori, N. Danilov *et al.*, *"A novel formulation for high light yield high transparency indium loaded liquid scintillator."* Submitted to Radiation Physics and Chemistry (2004).
- [CEA01] Nuclear power plants in the world, CEA/DSE/SEE (2001).
- [CHO98] M. Apollonio *et al.* (CHOOZ Collaboration), Phys. Lett. B420 397 (1998).
- [CHO00] M. Apollonio *et al.* (CHOOZ Collaboration), Phys. Rev. D61 012001 (2000).
- [CHO99] M. Apollonio *et al.* (CHOOZ Collaboration), Phys. Lett. B466, 415 (1999).
- [CHO03] M. Apollonio *et al.* (CHOOZ Collaboration), Eur. Phys. J. C27, 331 (2003).
- [Cle98] B. T. Cleveland *et al.*, Astrophys. J. 496, 505 (1998).
- [CNG02a] D. Duchesneau (OPERA Collaboration), hep-ex/0209082 (2002).
- [CNG02b] M. Komatsu, P. Migliozi and F. Terranova, hep-ph/0210043 (2002).

- [Cro89] S. Croft, NIM A 281, 103-106 (1989).
- [CTF98] G. Alimonti *et al.* (BOREXINO Collaboration), Astropart. Phys. 8, 141 (1998).
- [Dan03] N.A. Danilov, Yu. S. Krylov, C. Cattadori, "Development of scintillators to detect solar neutrino based on ytterbium chloride compounds and neutral organophosphorus compounds." Radiochemistry, 45 (2), 128-133 (2003).
- [Dec94] Y. Declais *et al.*, Phys. Lett. B338, 383 (1994).
- [ETL] <http://www.electrontubes.com/>.
- [Fog98] G. L. Fogli and E. Lisi, Phys. Rev. D54, 3667 (1998).
- [GAL99] W. Hampel *et al.* (GALLEX Collaboration), Phys. Lett. B447, 127 (1999).
- [Gar92] Garciaz, Ph.D. thesis, University of Provence (1992).
- [Gel79] M. Gell-Mann, P. Ramond and R. Slansky, in Supergravity, ed. by F van Nieuwenhuizen and D. Freedman, North-Holland, Amsterdam, 315 (1979).
- [GNO00] M. Altmann *et al.* (GNO Collaboration), Phys. Lett. B490, 16 (2000).
- [GOE86] G. Zecek *et al.*, Phys. Rev. D34, 2621 (1986).
- [Hag00] T. Hagner, R. von Hentig, B. Heisinger, L. Oberauer, S. Schönert, F. von Feilitzsch and E. Nolte, Astropart. Phys. 14, 33 (2000).
- [Hah89] A.A Hahn *et al.*, Phys. Lett. B218, 365 (1989).
- [Har85] F. X. Hartmann and R. A. Naumann, "Observation of *N* and *M* orbital electron capture in the decay of  $^{163}\text{Ho}$ ". Phys. Rev. C. (Rapid Comm.) 31, 1594-1596 (1985).
- [Har92] F.X. Hartmann and R. A. Naumann, "High temperature gas proportional detector techniques and application to the neutrino mass limit using  $^{163}\text{Ho}$ ." Nucl. Inst. and methods in Physics Research, Ser. A 313, 237 (1992).
- [Har99] F.X. Hartmann, Proc. of the 4th Int. Solar Neutrino Conference, Heidelberg, Germany, (1999).
- [Hor03] G. Horton-Smith, J. Atwell, R.D. McKeown, P Vogel, Presentation at the Workshop on Future Low Energy Neutrino Experiments, Technical University Munich, Munich, 9-11 October (2003).
- [Hub02] P. Huber, M. Lindner, T. Schwetz and W. Winter, Nucl. Phys. B665, 487 (2003).
- [Hub04] P. Huber, M. Lindner, T. Schwetz and W. Winter, hep-ph/0403068 (2004).
- [IAEA] <http://www.iaea.org/>.
- [ICA02] P. Aprili *et al.* (Icarus Collaboration), CERN-SPSC-2002-027 (2002).
- [IMB91] D. Casper *et al.* (IMB Collaboration) Phys. Rev. Lett. 66, 2561 (1991).
- [Inca] G. Fioni, M. Cribier, F. Marie *et al.*, Nucl. Phys. A693, 546 (2001). G. Fioni *et al.*, Journal of nuclear Science and technology sup. 876-879, 2(2002).
- [Jam] F. James, <http://wwwcn.cern.ch/asdoc/WWW/minuit/minmain/minmain.html>.